



HAL
open science

Anderson limit and topological edge states

Tianzhen Zhang

► **To cite this version:**

Tianzhen Zhang. Anderson limit and topological edge states. Superconductivity [cond-mat.supr-con]. Université Paris Saclay (COMUE), 2018. English. NNT : 2018SACLS240 . tel-01968063

HAL Id: tel-01968063

<https://theses.hal.science/tel-01968063v1>

Submitted on 2 Jan 2019

HAL is a multi-disciplinary open access archive for the deposit and dissemination of scientific research documents, whether they are published or not. The documents may come from teaching and research institutions in France or abroad, or from public or private research centers.

L'archive ouverte pluridisciplinaire **HAL**, est destinée au dépôt et à la diffusion de documents scientifiques de niveau recherche, publiés ou non, émanant des établissements d'enseignement et de recherche français ou étrangers, des laboratoires publics ou privés.

Limite d'Anderson et états de bords topologiques

Thèse de doctorat de l'Université Paris-Saclay
préparée à l'Université Paris-Sud

Ecole doctorale n°564 Ecole doctorale Physique en Ile de France (EDPIF)
Spécialité de doctorat : Physique

Thèse présentée et soutenue à Paris, le 13 Septembre 2018, par

TIANZHEN ZHANG

Composition du Jury :

Claude Pasquier Professeur, Laboratoire de Physique des Solides, Université Paris-Sud	Président
Laurent Saminadayar Professeur, Institut Néel CNRS/UGA UPR2940	Rapporteur
Claude Chapelier Directeur de Recherche, Laboratoire de Transport Electronique Quantique et Supraconductivité	Rapporteur
Pascale Diener Maître de Conférences, Institut d'électronique de microélectronique et de nanotechnologie	Examinatrice
Hervé Aubin Directeur de Recherche, Ecole supérieure de physique et de chimie industrielles de la ville de Paris	Directeur de thèse
Sergio Vlaic Maître de Conférences, Ecole supérieure de physique et de chimie industrielles de la ville de Paris	Invité

Acknowledgement

First of all, I would like to thank my supervisor Hervé Aubin, for all the knowledge he taught me on physics and others, for all the help he gave me for my thesis, for the attitude he has shown me about the research work, for all the patience and care to me in all these three years.

I would like to thank my colleagues, Alexandre Assouline, Hongyue Wang, Sergio Vlaic, Stéphane Pons, Dimitri Roditchev, Alexandre Zimmers, Zhuoying Chen, Christophe Brun, Cheryl Feuillet-Palma, Sophie Demonchaux, Marie-Claude Theme , Francis Casagne, Ricardo Lobo and all the others for their help in LPEM.

I would like to thank Jose Palomo in ENS and Alireza Mottaghizadeh, Christophe Manquest, Pascal Filloux, Stephan Suffit in Paris 7 for their help with micro-fabrications. I would like to thank J.C. Girard, G. Rodary and C. David for their help with the preparation of the InAs substrates for STM experiments. I would like to thank A. Lemaître for providing the InAs/GaSb heterostructures.

I would like to thank G. Allan and C. Delerue for the tight-binding calculations.

I would like to thank Gérard Dujardin, Andrew Mayne and Eric Le Moal in Paris sud for all their help.

I would like to thank all the friends in France, Hungju Lin, Hengyang Xiang, Zhelu Hu, Yanan Liu, Ye Jiang, Xiangzhen Xu, Shuiyan Cao, Yaqiong Wang and all the other friends for their help.

I would like to thank my family for their support all the time, especially to my husband for his accompany.

I would like to thank all for the time I spent in France.

Table des matières

Acknowledgement	i
Introduction	v
I STM spectroscopy of InAs	1
I.1 Theory of quantum tunneling	1
I.2 Scanning Tunneling Spectroscopy	5
I.3 Electronic properties of InAs	7
I.3.1 Metal-semiconductor interfaces	8
I.3.2 STM spectroscopy of InAs	13
II STM spectroscopy of Pb nanocrystals on InAs (110)	17
II.1 State of the art	18
II.1.1 Coulomb blockade	19
II.1.2 Quantum confinement	20
II.1.3 Superconductivity	22
II.1.4 Past works on quantum size effects on superconductivity	24
II.2 Growth of Lead(Pb) nanocrystals	27
II.3 Tip Induced QDot on InAs(110)	33
II.4 Coulomb blockade and nature of the tunnel barrier	35
II.5 From the Superconducting Parity Effect to the Anderson limit	42
II.6 Quantum confinement in Pb nanocrystals	52
II.7 Superconducting proximity effect from the nanocrytals into InAs	57
II.8 Conclusion	62
III STM spectroscopy of hinge states in Bismuth nanocrystals	65
III.1 Introduction to topological materials	66
III.2 Electronic properties of Bismuth	71

III.3 Growth of Bismuth nanocrystals	75
III.4 Scanning Tunneling Spectroscopy of Bismuth nanocrystals	76
III.5 Conclusion	83
IV Hybrid semiconductor-superconductor Josephson junctions	85
IV.1 Introduction to hybrid Josephson junctions on InAs-based semiconductors	86
IV.2 Josephson effect	88
IV.3 Microfabrication of Josephson junctions with III-V semiconductors . . .	92
IV.4 Measurements	97
IV.5 Conclusion	103
V Conclusion and Perspectives	105
VI Publications	107
Bibliographie	109

Introduction

These last ten years have seen the emergence of the era of topological band theory. The search for topologically non-trivial band-structures leads to the theoretical prediction of a plethora of new materials : topological insulators, topological semi-metals and topological superconductors.

For many of these new materials, the topological properties result from parity-inversions in the band structure ; for example, the topological properties of HgTe based topological materials result from the band inversion between the Γ_6 and Γ_8 bands existing in the bulk HgTe. However, topological properties can also arise from the combination of trivial materials. In this context, the III-V family of materials are particularly interesting. It has been shown theoretically[1] and experimentally[2, 3, 4, 5] that the heterostructures InAs/GaSb constitute a two-dimensional Quantum Hall Insulator, even that neither InAs or GaSb has inverted band structure. In addition, it has also been shown, theoretically[6] and experimentally[7], that the deposition of a superconducting electrode on the top of an InAs nanowire[7] leads to a topological superconductor, when submitted to an in-axial magnetic-field. Similarly, the deposition of a superconducting electrode on the two-dimensional quantum Hall insulator InAs/GaSb is expected to give rise to a topological superconductor[8].

This context leads to a renewal of interest for the interface between metals and III-V semiconductors. In some situations, STM spectroscopy can be a powerful tool for investigating interfaces at the atomic scale. For example, about 1989, STM spectroscopy near Fe clusters deposited on GaAs[9] was employed to demonstrate the presence of cluster-induced interface states. More recently, it has been demonstrated that STM tunneling spectroscopy on the side of cleaved III-V heterostructures is possible, which enabled the visualization of the discrete quantum dots levels in self-assembled InAs QDots grown on GaAs[10, 11, 12, 13].

For this thesis, I worked on the growth of superconducting (Pb) and semi-metallic (Bi) nanocrystals on the (110) surface of InAs and the STM spectroscopy of these

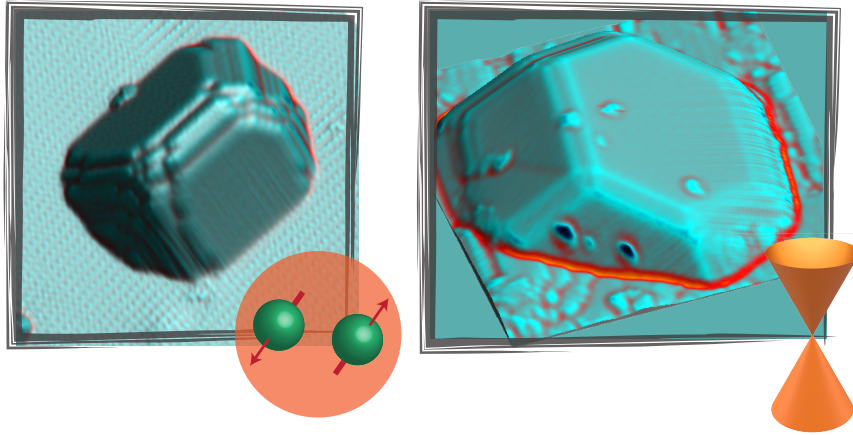


Fig. .1 *STM topographic images of (left) Pb and (right) Bi nanocrystals on InAs(110).*

systems. In addition, I also worked on the microfabrication of InAs/GaSb heterostructures, which, in the future, could be employed in cross-sectional STM spectroscopy.

In this manuscript, I will provide, in the first chapter, the theoretical background on quantum tunneling and review our current understanding of the interface between III-V semiconductors and metal overlayers.

In the second chapter, I will describe the first experiment where I show that high quality superconducting Lead (Pb) nanocrystals can be grown on the (110) surface of InAs. We found that when the lateral size of the Pb nanocrystals is smaller than the Fermi wavelength of the two-dimensional electron gas accumulated at the surface of InAs, the nanocrystals are only weakly coupled to this electron gas and, consequently, are found in the regime of Coulomb blockade. This phenomenon enabled the first study of the superconducting parity effect through STM spectroscopy, which we employed to check the validity of the Anderson limit for the existence of superconductivity in Pb nanocrystals. Furthermore, we identified, in these Pb nanocrystals, the signature of discrete electronic levels and attempted a mapping of the corresponding electronic wavefunctions.

In the third chapter, I will describe the second STM experiment where I show that high quality Bismuth (Bi) nanocrystals can also be grown on the (110) surface of InAs. In contrast to Pb nanocrystals, a wetting layer of Bi separates the nanocrystals from the InAs surface, leading to a strong coupling between the Bi nanocrystals and the substrate. From STM spectroscopy, we have identified edge-states on the (111) plane

of the bismuth nanocrystals. These edge-states have C3 symmetry, which is lower than the C6 symmetry of the (111) face. Assuming that Bismuth is a 2nd order topological insulator as suggested theoretically, the observed edge-states can be interpreted naturally as the hinge-states predicted in this last topological band-theory.

Finally, in the last chapter, I will present the methods that I developed for the fabrication of hybrid Josephson junctions on bulk InAs and InAs/GaSb heterostructures, together with preliminary measurements of Josephson characteristics.

I – STM spectroscopy of InAs

As an essential part of this thesis is about the tunneling spectroscopy of metallic/superconducting nanocrystals grown on InAs, I will introduce in this first chapter the basic theoretical and technical elements required to understand our experiments. I will start, first, with a basic introduction on quantum tunneling and provide a description of the STM microscope installed in the laboratory. Second, I will provide an elementary description of the electronic properties of the semiconductor InAs, as well as provide a review of our current understanding on the surface physics of this material.

I.1 Theory of quantum tunneling

In classical physics, a particle cannot go through a potential barrier which is larger than its kinetic energy. However, in quantum physics, a particle can tunnel through such a potential barrier with some probability, this is called quantum tunneling. Considering the one dimensional square barrier shown in Fig. I.1 : a particle with energy ε on the left side of the barrier is described by the wavefunction ψ_L , and, after tunneling across the barrier of height U , is described by the wavefunction ψ_R .

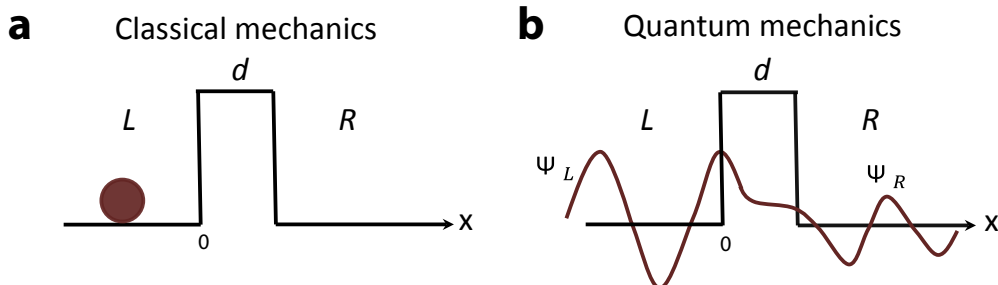


Fig. I.1 A particle in the front of a barrier potential in a) classical mechanics and b) quantum mechanics. The barrier has width d and height U .

As described by the equations :

$$\begin{aligned}\psi_L &= Ae^{ikx} + Be^{-ikx} \\ \psi_R &= Ce^{ikx} + De^{-ikx}\end{aligned}$$

the wavefunction ψ_L is the sum of two components propagating in opposite directions, $\psi_{in} = Ae^{ikx}$ which penetrates into the barrier and $\psi_{re} = Be^{-ikx}$ which is reflected by the barrier and travels backward. Meanwhile, the final state ψ_R is also the sum of two components, the transmitted wave $\psi_{tran} = Ce^{ikx}$, propagating away from the barrier and $\psi_{re} = De^{-ikx}$ travelling backward. The transmission coefficient T , i.e. the tunneling probability for a particle to cross the barrier is given by :

$$T = \frac{|\psi_{tran}|^2}{|\psi_{in}|^2} = \frac{CC^*}{AA^*}$$

Furthermore, the wavefunction ψ_B inside the barrier can be written as :

$$\psi_B = Ge^{ik_2x} + Fe^{-ik_2x}$$

The evolution of ψ_L , ψ_R and ψ_B is described by the Schrödinger equation :

$$\begin{aligned}\frac{\hbar^2}{2m} \frac{\partial^2}{\partial x^2} \psi_L + \varepsilon \psi_L &= 0 \\ \frac{\hbar^2}{2m} \frac{\partial^2}{\partial x^2} \psi_B + (U - \varepsilon) \psi_B &= 0 \\ \frac{\hbar^2}{2m} \frac{\partial^2}{\partial x^2} \psi_R + \varepsilon \psi_R &= 0\end{aligned}$$

These equations have to be solved with the following boundary conditions :

$$\psi_L(x=0) = \psi_B(x=0), \psi_B(x=d) = \psi_R(x=d)$$

which can be done in the so-called Wentzel-Kramers-Brillouin (WKB) approximation, giving the transmission coefficient T as function of the electron energy ε :

$$T(\varepsilon) \propto e^{-\frac{2\sqrt{2m(U-\varepsilon)}d}{\hbar}} \quad (\text{I.3})$$

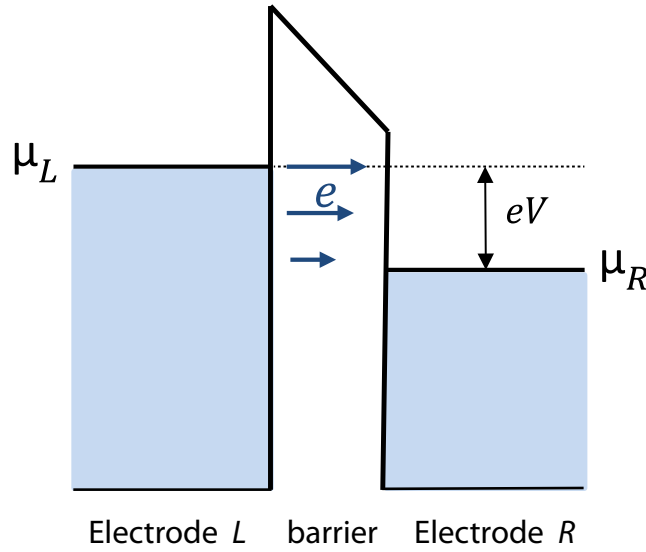


Fig. I.2 Sketch of the tunneling process between two metallic electrodes.

The application of quantum theory of tunneling to the case of two metallic electrodes separated by a thin insulating barrier was done in the 1960s by Bardeen[14] and Simon[15]. In this case, we have to consider tunneling between two Fermi liquids, as sketched Fig. I.2. An applied voltage V between two metallic electrodes leads to a shift of the electrochemical potentials. In this situation, empty electronic states of one metallic electrode are facing full electronic states of the other metallic electrode. If the insulating barrier is not too thick, quantum electron tunneling from the full states to the empty states is possible.

The tunneling current between the two metallic electrodes can be calculated from the Landauer formula[16, 17] :

$$I(V) = \frac{2e}{h} \int_{-\infty}^{\infty} T(\varepsilon) [f_L(\varepsilon) - f_R(\varepsilon)] d\varepsilon \quad (\text{I.4})$$

where $f_L(\varepsilon) = \frac{1}{\exp\left[\frac{\varepsilon - \mu_L - e\psi_L}{k_B T}\right] + 1}$ and $f_R(\varepsilon) = \frac{1}{\exp\left[\frac{\varepsilon - \mu_R - e\psi_R}{k_B T}\right] + 1}$ are the Fermi distributions of the left (L) and right (R) electrodes, respectively. $\mu_{L(R)}$ is Fermi energy of the left and right electrodes and $V = \frac{\mu_L - \mu_R}{e}$ is the voltage polarization of the junction.

Introducing the transmission coefficient (I.3) into the Landauer equation (I.4), one gets an expression for tunneling current, a formula first obtained by J. Simmons[15] :

$$I = I_0[U \exp[-AU^{1/2}] - (U + eV) \exp[-A(U + eV)^{1/2}]]$$

with :

$$I_0 = \frac{e}{4\pi^2\hbar(\beta d)^2}$$

$$A = \frac{-2\beta d\sqrt{2m}}{\hbar}$$

where $\beta \sim 1$. In the low voltage limit, this last formula can be written as :

$$I = \frac{e^2\sqrt{2mU}}{h^2d} V \exp[-\frac{2}{\hbar}\sqrt{2mdU}]$$

which shows that the tunnel junction has a ohmic behavior at low voltage, i.e. the tunneling current increases linearly with the voltage, $I \sim V$, and so the differential conductance dI/dV is constant and featureless at low bias. This formula also shows that the current decreases exponentially with the distance, $I \sim \exp(-\beta_0 d)$, where the attenuation coefficient $\beta_0 \sim 1\text{\AA}^{-1}$ for a tunnel barrier of height $U = 1\text{ eV}$.

The differential conductance $dI/dV(V)$ remains constant at low bias only when the density of states in the two metallic electrodes is constant as function of energy. When this is not the case, i.e. the density of states changes with energy, its effect on the tunneling current can be described by a formula similar to the Landauer formula :

$$I(V) = \frac{2e}{h} \int_{-\infty}^{\infty} \rho_S(\varepsilon) [f_L(\varepsilon) - f_R(\varepsilon)] d\varepsilon$$

where $\rho_S(\varepsilon)$ is the density of states in one of the metallic electrodes, from which it follows that the differential conductance is proportional to the density of states :

$$\frac{dI}{dV}(V_{\text{bias}}) \sim \rho_S(eV_{\text{bias}}) \quad (1.5)$$

Thus, dI/dV curves as function of bias voltage provide a measure of the local density of states on the sample surface as function of energy.

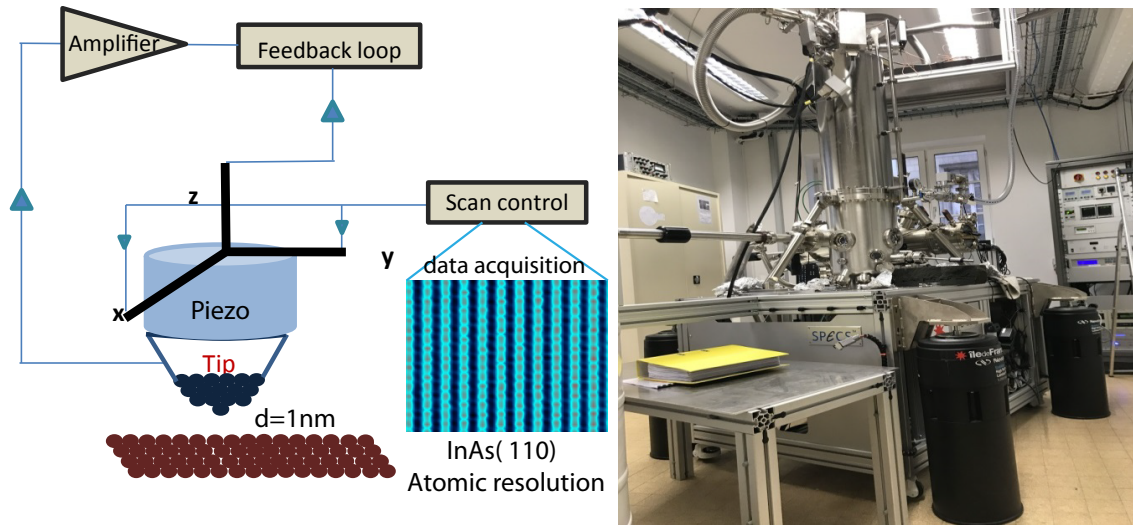


Fig. I.3 a) Sketch of an STM. b) Photo of LT-STM (SPECS) in LPEM.

I.2 Scanning Tunneling Spectroscopy

Gerd Binnig and Heinrich Rohrer built the first Scanning Tunneling Microscope[18, 19, 20] and won the Nobel Prize for this discovery in 1986. The STM has already played and will continue to play an important role in surface science. In this section, I will briefly introduce the working principle of STM. As sketched in Fig. I.3, a STM tip (which can be made of Pt/Ir, W, etc.) is fixed to a piezoelectric tube. Upon applying a voltage, up to 300 V, on the electrodes covering the piezoelectric tube, motion in the three spatial directions x , y and z is possible with sub-Angstrom resolution. The working range of the piezoelectric tube is only a few microns. For this reason, a piezoelectric motor is used to approach the tip, initially a few millimeter away from the sample, toward the surface of the sample, such that the tip-surface distance becomes smaller than $1 \mu\text{m}$, the working range of the piezoelectric tube. This piezoelectric motor moves by steps where one step is in the range of 20-200 nm. To approach the tip at a distance about $1 \mu\text{m}$ of the sample surface without *crashing* the tip, we use the following standard method : first, we make one step in the range 20-100 nm with the piezoelectric motor ; second, we extend the piezoelectric tube up to its maximum length while measuring the tunneling current. If no tunneling current is measured, we retract the piezoelectric tube and execute an additional step with the piezoelectric motor and so on. This procedure is automated and can even be launched overnight. It

stops when a tunneling current is detected.

Once the tip is in the tunneling regime, i.e. an electrical current between the tip and the surface can be measured, scanning tunneling microscopy and spectroscopy experiments can be executed.

The scanning process is controlled by a feedback loop and a scanning controller. There are two working modes of the STM. One is the constant current mode, the other is the constant height mode. The constant current mode is a convenient mode for making topographic images of the sample surface. With this method, a current setpoint is set into the feedback loop controller. This feedback loop adjusts constantly the height z of the tip so that the measured tunneling current is equal to the current setpoint. Then, by scanning the tip along the x and y directions above the surface, we obtain a matrix of values z as function of x and y . This two-dimensional matrix is the topographic image of the surface of the sample, as shown in the inset of Fig. I.3. In the constant height mode, the height of z is not changed. Note that in this mode, the STM tip can be crashed if the surface is not flat.

At each point of the scanning area, the lateral tip motion can be stopped to acquire a tunneling spectrum. To do that, one stops the feedback loop and measures the tunneling current as function of bias voltage V_{bias} , thus providing the $I - V$ curve. However, we are usually more interested by the differential conductance $dI/dV(V_{\text{bias}})$ as it is directly proportional to the density of states, see Eq.(I.5). This differential conductance curve can be obtained from numerical differentiation of the $I - V$ curve or can be measured directly with a lock-in amplifier. In this thesis, we use the lock-in method to measure dI/dV curves. The principle of this method is to add a sinusoidal signal $V_{\text{AC}} = V_0 \sin(\omega t)$ to the DC signal. This added signal V_{AC} causes an oscillation $I_{\text{AC}} = I_0 \sin(\omega t)$ of the tunneling current at the same frequency, whose amplitude I_0 is extracted by the lock-in amplifier. The differential conductance is directly given by :

$$\frac{dI}{dV} = \frac{I_0}{V_0}$$

Thus, the lock-in method enables a measurement of the $dI/dV(V)$ curves with high signal to noise ratio.

In this thesis, we work with the *SPECS* JT-STM installed at LPEM. This STM is functioning under Ultra-High Vacuum ($\approx 10^{-10}$ mbar) and can be cooled down to a temperature $T \approx 1.3$ K thanks to a Joule-Thomson stage. A picture of this STM is shown Fig. I.3b. This STM is equipped of a preparation chamber with an e-beam evaporator for the evaporation of elements such as Pb, Bi, Au, Sb etc.

I.3 Electronic properties of InAs

To obtain the results presented in this thesis, I extensively used the semiconductor InAs. I used it for the STM experiments, as a substrate for the growth of the nanocrystals of Bismuth and Lead, I also used it for the fabrication of Josephson junctions on bulk InAs and the two-dimensional heterostructure InAs/GaSb.

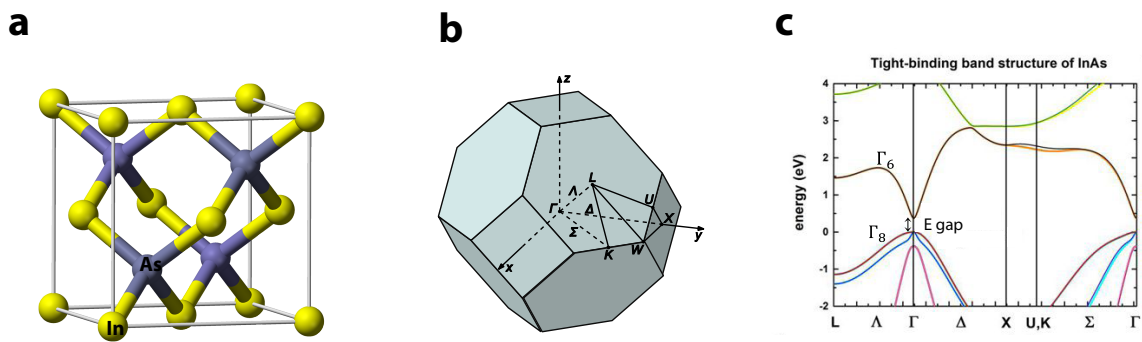


Fig. I.4 a) Sketch of a single unit cell of zinc blende InAs crystal. b) First Brillouin zone of bulk InAs. c) Band structure calculated by tight binding method extracted from Ref. [21].

InAs is a narrow-gap semiconductor where In is an element of column III and As is an element of column V, making this semiconductor a member of the so-called III-V family of semiconductors which also include the well known GaAs, AlSb, InSb. As one of these III-V semiconductors, InAs has a zinc blende crystal structure with space group $\bar{F}43m$. The unit cell and the first Brillouin zone are shown in Fig. I.4. Figure I.4c shows the band structure of InAs. It has a small direct band-gap $E_{\text{gap}} \sim 0.3$ eV at the Γ point separating the Γ_6 conduction band from the doubly degenerate valence band Γ_8 . The Γ_6 band results from the s-type orbitals from the In atoms while the Γ_8 bands results from the p-type orbitals from the As atoms. The s-type orbitals have even spatial symmetry while the p-type orbitals have odd spatial symmetry. As will be described in the last chapter, in InAs/GaSb heterostructures, this is the inversion of the symmetry of the conduction and valence bands that leads to non-trivial topology of the band structure in this 2D gas.

I.3.1 Metal-semiconductor interfaces

On a semiconductor surface, the adsorption of a metal overlayer leads to band bending as sketched in Fig. I.5. This band-bending leads to a carrier depletion at the surface of the semiconductor and is responsible for the formation of a Schottky barrier at the interface between the metal and the semiconductor. As we will see, in rare cases, the metal deposition leads to a carrier accumulation at the interface.

For metal-semiconductor interfaces, the barrier height ϕ_{Bn} for the electrons in the conduction band is generally given by the relation :

$$\phi_{\text{Bn}} = S_{\phi}(\phi_{\text{m}} - \chi_{\text{s}}) + (1 - S_{\phi})(W_{\text{ci}} - W_{\text{0i}}) \quad (\text{I.6})$$

where ϕ_{m} is the metal work function, χ_{s} is the semiconductor electron affinity, W_{ci} is the energy of the conduction band bottom, W_{0i} is the charge-neutrality level and $S_{\phi} = \frac{\partial \phi_{\text{Bn}}}{\partial \phi_{\text{m}}}$ is the slope parameter. This last parameter describes the dependence of the barrier height on the metal work-function[22].

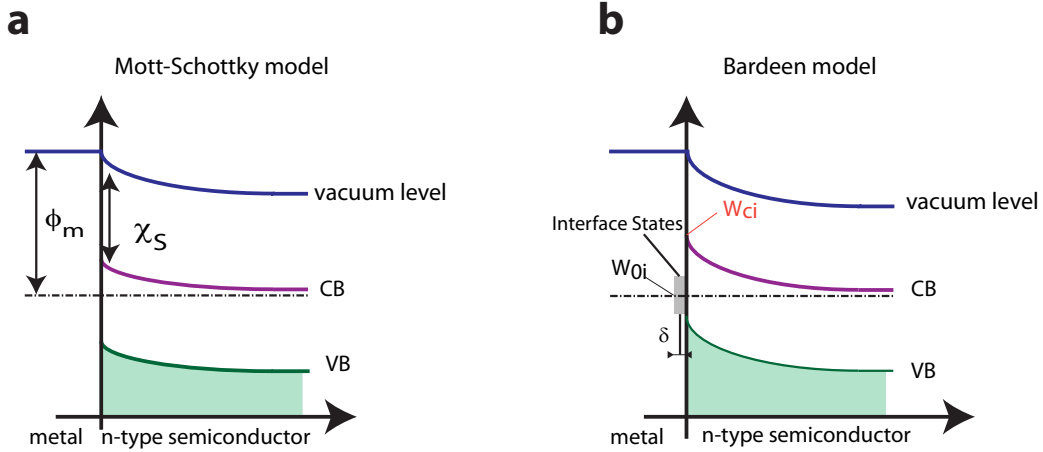


Fig. I.5 a) Mott-Schottky model of band-bending, which applies in the absence of interface states. b) Bardeen model of band-bending, which applies in the presence of interface states[23].

In a Mott-Schottky model, shown in Fig. I.5a, where no interface states are present, the slope parameter $S_{\phi} = 1$ in Eq. (I.6), then the barrier height is :

$$\phi_{\text{Bn}} = \phi_{\text{m}} - \chi_{\text{s}} \quad (\text{I.7})$$

According to Eq. (I.7), the barrier height is proportional to the amplitude of the metal work function.

In a Bardeen model, shown in Fig. I.5b, interface states are present, the slope parameter $S_\phi = 0$ in Eq. (I.6), then the barrier height is :

$$\phi_{\text{Bn}} = W_{\text{ci}} - W_{0\text{i}}$$

In this case, the Fermi level is pinned by interface states at the charge neutrality level. The charge-neutrality level separates the electron-type levels from the hole-type levels. As described in Refs. [22, 24, 25, 26], because the interface states derive from the band structure of the semiconductor, the charge neutrality level is an intrinsic property of the semiconductor, which implies that the barrier height does not depend on the metal work function.

A plot of the slope parameter measured experimentally for many distinct semiconductors, Fig. I.6, shows that in III-V semiconductors the slope parameter is close to zero, indicating that the barrier height is set by the Bardeen relation, where a large density of interface states is induced by the metal overlayer and leads to a pinning of the Fermi level. Ionic semiconductors presenting a large electronegativity difference between the cation and the anion, such as the chalcogenides CdS, CdSe, etc tend to have a large slope parameter, which implies that the Mott-Schottky model applies. In contrast, covalent semiconductors such as Si, GaAs and InAs (not shown on the graph) tend to have a small slope parameter implying the presence of a large density of interface states that pin the Fermi level at the charge neutrality level, i.e. Bardeen model.

The structural and electronic properties of metal layers deposited on III-V compounds have been the subject of an active research effort in surface physics. While transition metals react and/or interdiffuse when deposited on silicon and on III-V semiconductor surfaces, semimetals give ordered and epitaxial two-dimensional epilayers without alloying with the substrate. These atomically sharp interfaces are suitable model systems for experimental and theoretical studies of the atomic geometry and electronic properties of 2D ordered layers[27, 28]. For most III-V semiconductors, the charge neutrality level lies within the band gap except for small gap materials like InAs and InSb, where the charge neutrality level has been found within the conduction band[29, 30, 24, 31]. Consequently, the adsorption of a metal overlayer leads to the formation of accumulation layer of electrons as sketched in Fig. I.7b. In particular, on InAs (110), photoemission measurements have shown that the Fermi energy

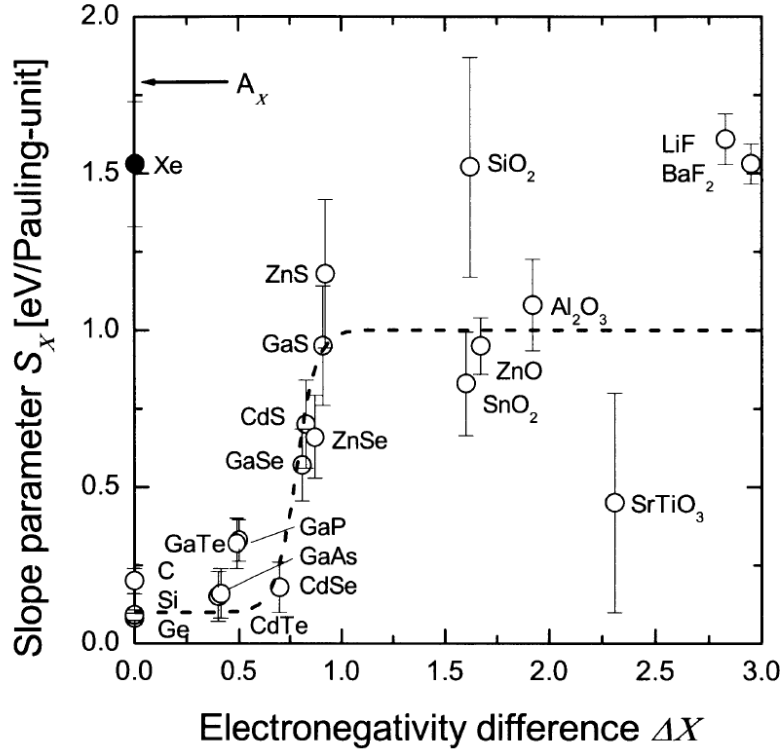


Fig. I.6 The slope parameter S_ϕ as function of electronegativity difference for a series of binary semiconductors[25].

is about 100-400 meV above the conduction band minimum upon deposition of different adsorbates such as H, O, N, Cl, Ag, Au, Ga, Cu, Cs, Na, Sb, Nb, Fe and Co[32, 33, 34, 35, 36, 37, 37, 38, 39, 40, 41, 42, 43, 44] and Fig. I.8. For Pb, while no data exists for the (110) surface, it was shown that one mono-layer of Pb on the (100) surface of InAs leads to an accumulation layer of electrons[45].

Pinning of the Fermi level can also occur at bare UHV cleaved surfaces as a consequence of native surface defects. On InAs, this leads to the formation of an accumulation layer at (100) and (111) surfaces[46, 47], but not on the (110) surface where the band remains flat, Fig. I.7a. The absence of defects on the (110) surface of InAs is well-known and make this surface particularly interesting for surface science studies. This (110) surface is non-polar, with a cation and an anion occurring in the surface unit cell. Strong electrostatic forces that could push the reconstruction process are not

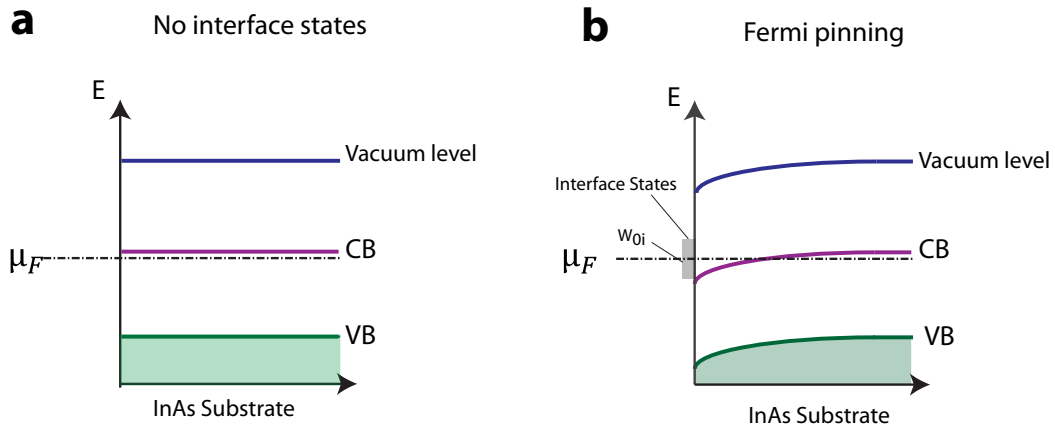


Fig. I.7 a) Flat band structure in absence of interface states. b) Fermi level pinning effect in the presence of interface states.

present and, hence, the bulk-terminated (1×1) translational symmetry is conserved. Furthermore, the (110) planes contain only weakly interacting zigzag chains of bonded group-III and group-V atoms, where each atom possesses a dangling bond. Thus, this surface is intrinsically neutral, free from defects and no reconstruction is ever observed for this surface[24]. Consequently, no pinning of the Fermi level is ever observed for the UHV cleaved (110) surface.

One remarkable consequence of the absence of Fermi level pinning is the possibility

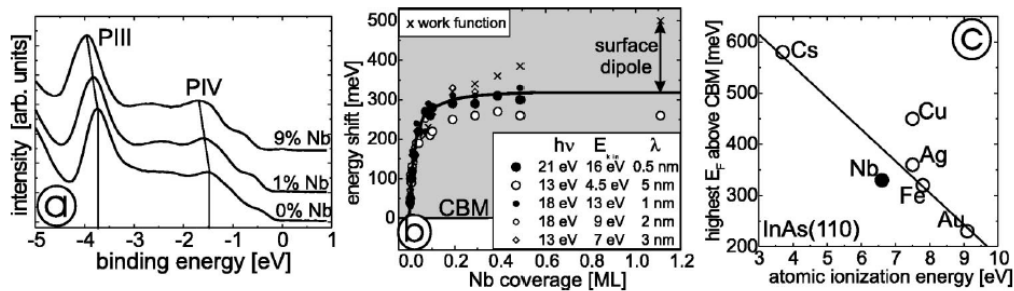


Fig. I.8 Figure extract from Ref. [43]. a) Photoemission spectra on n -type InAs (110) taken at different Nb coverages as indicated. The peaks shift to negative energies as metal is deposited indicates Fermi level shifting at the surface of InAs. b) Plot of the change in the shift of the Fermi energy with metal coverage. c) Measured highest positions of the Fermi level with respect to the conduction-band minimum for different adsorbate atoms as a function of the ionization energy of the corresponding atom.

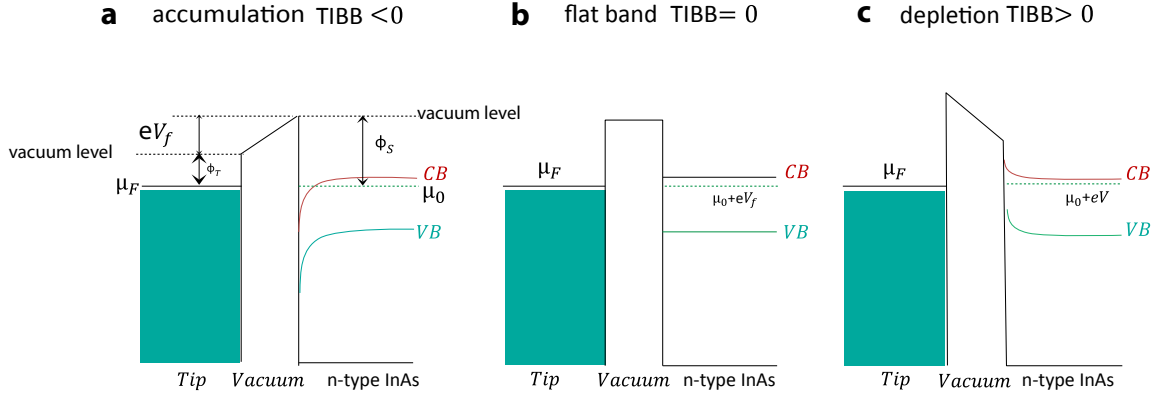


Fig. I.9 Tip induced band bending (TIBB) in three cases : $TIBB < 0$, $TIBB = 0$, $TIBB > 0$.

to shift the conduction band energy with the electric field induced by the STM tip, the so-called tip-induced band bending[48, 49, 50, 51].

To illustrate this phenomena, I show a sketch, Fig. I.9, of the band bending induced in a semiconductor by the applied bias on the tip, where the work-functions of the tip and the semiconductor are respectively ϕ_T and ϕ_S .

Three different cases are shown and described now :

Case I : $V_{\text{bias}} = 0$

No bias voltage is applied, $V_{\text{bias}} = 0$. In that case, because of the differences in the work functions between the metal and the semiconductor, the bands in the semiconductor will bend down at the approach of the surface. This leads to the formation of an electron accumulation layer at the surface of the semiconductor. The amplitude of this band bending can be defined as eV_f , where the V_f is the flat band voltage, i.e. the voltage needed on the tip to compensate for the work function difference and make the band flat in the semiconductor.

Case II : $V_{\text{bias}} = V_f$

A bias voltage $V_{\text{bias}} = V_f$ is applied. This compensates for the work function difference between the tip and the semiconductor and the band becomes flat as shown.

Case III : $V_{\text{bias}} < V_f$

The bands bend in the opposite directions. The electron gas at the surface of the semiconductor is completely depleted.

Because the tip-induced band-bending only occurs on a narrow size region below the tip, this leads to the formation of a quantum dot in the 2D electron gas at the

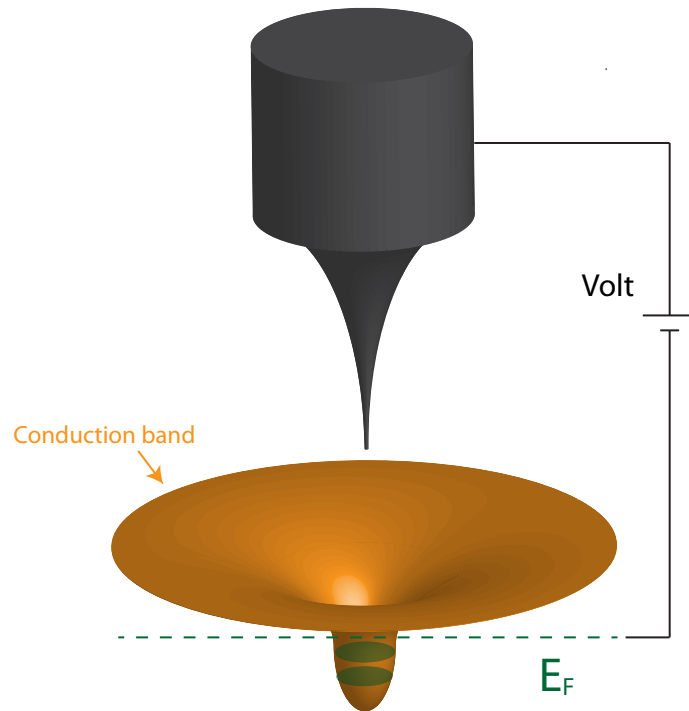


Fig. I.10 The band bending induced by the tip leads to the formation of a QDot into the accumulation layer at the surface of InAs. This QDot has discrete electronic levels as indicated by the green circles.

surface of InAs, so-called tip-induced quantum-dot, as sketched in Fig. I.10 which is going to be identified in the tunneling spectrum by conductance peaks resulting from the discrete electronic levels in the QDot.

I.3.2 STM spectroscopy of InAs

To perform the tunneling spectroscopy with atomic resolution, the substrate must be prepared in Ultra High Vacuum (UHV). In the case of III-V semiconductors, the method to prepare the surface is to cleave a piece of wafer in UHV. To that end, starting with a (001) InAs wafer, we cut a rectangle of dimensions $3.8 \text{ mm} \times 7 \text{ mm}$ using a diamond scribe, the long length direction of the rectangle is along the [100] direction, the short length is along the [110] direction. On this rectangle, a small mark is made with a diamond tip at mid-height of the sample, shown in Fig.I.11a. Then, the sample is fixed into a vise as shown in Fig. I.11b. Upon pushing on the side of the sample, the sample will be cleaved, providing the surface (110). In Fig.I.11c, in

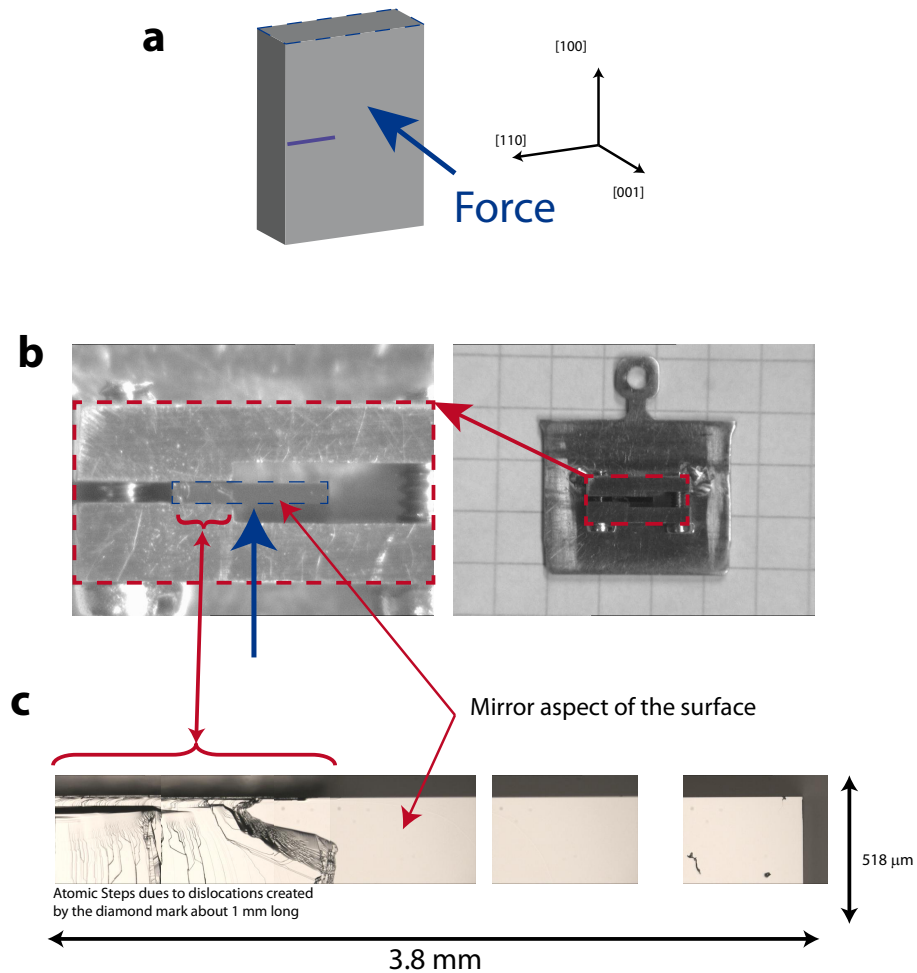


Fig. I.11 a) After cutting the wafer into a small rectangle ($3.8 \text{ mm} \times 7 \text{ mm}$), a mark made by a diamond tip at the mid-height is shown by the blue line. b) The sample is inserted into the vise on the sample holder and fixed by tightening the screws. c) The sample is cleaved by pushing on the side. A nice mirror-like surface is observed, while atomic steps due to dislocations are observed in area around the mark.

the area near the mark made by the diamond tip, many atomic steps are observed on the surface. However, beyond this area, the sample cleaves very nicely with a mirror finish and with few atomic steps as shown by the optical images. This method was developed by the STM group in C2N (J.C. Girard, C. David), and actually prepared the samples for us. We only had to fix the sample into the vise and cleave the sample into UHV. After inserting the sample into the UHV preparation chamber, the sample with its sample holder including the vise is baked at 250 °C to clean it. After cooling at room temperature, the sample is cleaved by pushing on the side with the wooble stick.

For the STM experiments, we used Sulfur doped substrates. Figure I.12b shows a topographic image of the InAs surface with atomic resolution. Figure I.12c is the measured dI/dV curve on this surface. From the curve, we can clearly identify the edges of the conduction and valence bands. The edge of the conduction band is the closest to zero bias, indicating that the Fermi level is in the conduction band as expected for this n doped InAs sample. With a dopant concentration, $N_D \sim 6 \times 10^{16} \text{cm}^{-3}$, the Fermi level E_F is 21 meV above the conduction-band minimum. A zoom of these spectra on the energy range [-150, 100] meV, Fig. I.12d, shows the presence of small conductance peaks. These peaks result from tip-induced QDots, as already observed in past works on (110) surface of InAs[52, 31]. So far, these tip-induced QDots have been observed only on the (110) surface of InAs, confirming that the Fermi level is not pinned at this surface. Had the Fermi level been pinned, it would not have been possible to shift the conduction band below the tip and so creates the QDot at the origin of the conductance peaks.

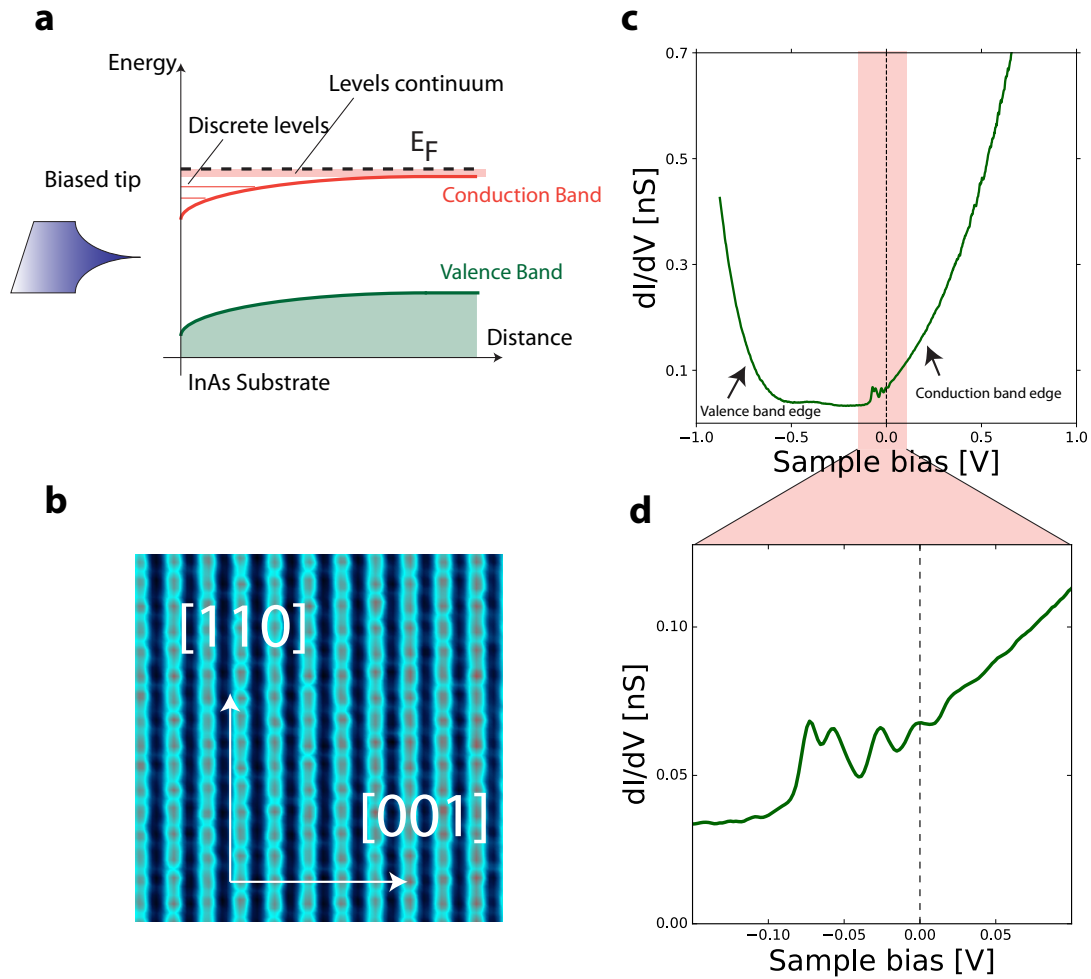


Fig. I.12 a) The band bending induced by the tip leads to the formation of a QDot into the accumulation layer at the surface of InAs. This QDot has discrete electronic levels that are seen as conductance peaks into the tunneling spectra shown panels c and d. b) Topographic image of the (110) surface of InAs. c) Conductance spectrum dI/dV measured on the InAs surface. The edges of the conduction and valence bands are clearly visible, as well as the conductance peaks due to the discrete levels in the tip-induced QDot. d) Zoom at low bias on these conductance peaks.

II – STM spectroscopy of Pb nanocrystals on InAs (110)

How small superconductors can be? For isolated nanocrystals subject to quantum size effect, P.W. Anderson conjectured in 1959[53] that superconductivity could only exist when the electronic level spacing δ is smaller than the superconducting gap energy Δ . In this chapter, I will describe a Scanning Tunneling Spectroscopy (STS) study of superconducting Pb nanocrystals grown on the (110) surface of InAs. We found that for nanocrystals of lateral size smaller than the Fermi wavelength of the 2D electron gas at the surface of InAs, the electronic transmission of the interface is weak. This leads to Coulomb blockade and enables the extraction of the electron addition energy of the nanocrystals. For large nanocrystals, the addition energy displays superconducting parity effect, a direct consequence of Cooper pairing. Studying this parity effect as function of nanocrystal volume, we find the suppression of Cooper pairing when the mean electronic level spacing overcomes the superconducting gap energy, thus demonstrating unambiguously the validity of the Anderson criterion.

In the first part of this chapter, I will provide the fundamental theoretical background on Coulomb blockade, quantum confinement and superconductivity, required to understand this experiment as well as a review on most relevant past study of quantum confinement effect on superconductivity. In the second part, I will describe the growth of the Pb nanocrystals on InAs(110). In the third part, I will describe the observation of the superconducting parity effect and its disappearance at the Anderson limit. In the fourth part, I will describe other various manifestations of quantum confinement effect on Pb nanocrystals. Finally, I will describe the observation of the superconducting proximity effect from the Pb nanocrystals into the InAs substrate.

II.1 State of the art

Atomic clusters and nanocrystals offer promising perspectives for the study of electronic orders and correlations at the scale of single electronic states in the quantum confined regime, through statistical analysis of the energy levels distribution or the study of the spatial structures of the corresponding wave-functions.

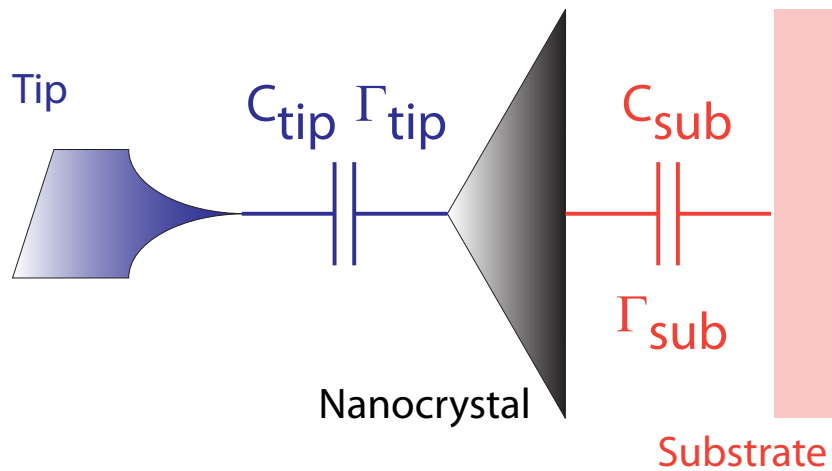


Fig. II.1 A nanoparticle weakly coupled to electrodes where Coulomb blockade can block electronic transport.

Numerous STM work of UHV grown metallic clusters strongly coupled to the substrate have already been published[54]. Indeed, the STM seems particularly well adapted to the study of quantum confinement effect on nanocrystals : the STM can provide both a topographic image of the nanocrystals and spectroscopic data, which enables not only the observation of discrete electronic levels but also a mapping of the corresponding wave-functions. However, the study of quantum confinement effects in isolated UHV grown nanocrystals has been hampered by two contradicting requirements : on one hand, the substrate should be conducting enough to enable a current path to the ground ; on the other hand, the nanocrystals should also be separated from this substrate by a second tunneling barrier to preserve Coulomb blockade and quantum confinement. One major contribution of my thesis is the identification of a highly clean system where the superconducting nanocrystal is only weakly coupled to

the conducting substrate, thus, enabling tunneling spectroscopy of nanocrystals in the regime of quantum confinement.

II.1.1 Coulomb blockade

Coulomb blockade is a mesoscopic phenomenon. It occurs in small metal islands where electrons produce a repulsive Coulomb force that prevents other electrons from flowing in.

For double tunnel barrier junctions as sketched in Fig. II.1, electronic transport from one electrode to the other through a nanocrystal implies necessarily charge variations in the nanocrystal of the amount of at least a single charge e . When the size of the nanocrystal is small enough, the effect of an excess electron can be large enough to react back on the tunneling probability of another electron. This charge feedback is called Coulomb blockade which has been found in the early 1950's by Gorter[55]. The Coulomb blockade can take place not only in metal and semiconductor islands where the charge carriers are electrons or holes but also in superconducting islands in which the charge carriers are Cooper pairs.

To charge an island, which is coupled to electrodes by capacitance whose sum amount to C_Σ , with an electron of charge e requires the Coulomb energy :

$$E_C = \frac{e^2}{2C_\Sigma} \quad (\text{II.1})$$

The Coulomb blockade model is only valid if electron states are localized on the island. This implies that the tunnel resistance R_T between the nanocrystal and the electrodes is sufficiently high. An estimation of the minimum resistance required can be obtained by considering the Heisenberg energy uncertainty :

$$\Delta E \Delta t > \frac{\hbar}{2}$$

where $\Delta E = E_C$ is given by the Coulomb energy and the characteristic time for charge fluctuation, Δt , is given by the time required for charging a capacitance C_Σ through a tunnel resistor R_T :

$$\Delta t = R_T C_\Sigma$$

These relations lead to the minimum tunnel resistance for the existence of the Coulomb blockade, which is :

$$R_T > \frac{h}{e^2} = 25.8k\Omega$$

A second condition required for the observation of the Coulomb blockade is that the Coulomb energy exceeds the energy of thermal fluctuations :

$$E_C \gg k_B T$$

II.1.2 Quantum confinement

A direct consequence of quantum confinement is to induce discrete energy levels [56, 57]. This occurs when the size of a nanostructure is comparable to the Fermi wavelength in metals or the Debye wavelength in semiconductors. The quantum confined regime has been intensively studied in semiconducting Quantum Dots (QDots), either in colloidal QDots[58, 59, 60, 61, 62, 63, 64, 65, 66, 67, 68] or in micro-fabricated QDots[69, 70, 71, 72, 73, 74], where the mean level spacing δ given by :

$$\langle \delta \rangle = \frac{2(\pi\hbar)^2}{m^*k_F \text{Volume}}$$

is large because of the large Fermi wavelength $\lambda_F = 2\pi/k_F$, which makes the experimental identification of the discrete levels in the spectrum easier than in metallic QDots where the Fermi wavelength is short. Moreover, the energy distribution of the electronic levels and the structure of the associated wavefunctions is expected to depend on the location of the energy levels with respect to the Thouless energy :

$$E_T = h/\tau$$

where τ is the propagation time of the electrons across the QDot. With this definition of the Thouless energy, one finds that the ratio $E_T/\langle \delta \rangle$ (II.2) depends only on the ratio of the QDot radius r with the Fermi wavelength λ_F .

$$E_T/\langle \delta \rangle = (4\pi/3)(r/\lambda_F)^2 \simeq 0.5(r/\lambda_F)^2 \quad (\text{II.2})$$

Two regimes of quantum confinement can be distinguished with $E_T/\langle \delta \rangle > 1$ for the chaotic regime and $E_T/\langle \delta \rangle < 1$ for the regular regime.

The chaotic regime $E_T/\langle \delta \rangle > 1$, where the level spacing is smaller than the Thouless energy, is reached in QDots of radius much larger than the Fermi wavelength. In this

case, for electronic states whose energy measured with respect to the Fermi energy is smaller than the Thouless energy, the electronic wave-functions are delocalized on the whole QDot and consequently, the electronic states are correlated through their Fermi statistics. In presence of electron-electron interactions and disorder, this leads to the formation of a complex quantum system with chaotic dynamic[75, 76]. The energy levels are expected to follow a distribution $P(\varepsilon)$ given by Random Matrix Theory (RMT)[77, 78] characterized by levels repulsion $P(\varepsilon \rightarrow 0) \simeq 0$ at zero energy as a consequence of Pauli exclusion. Furthermore, the wavefunctions are expected to display large amplitude fluctuations with random or possibly fractal structure[79]. This chaotic regime has been studied in micrometer sized QDots micro-fabricated from III-V heterostructures and measured at milli-kelvin temperature in dilution fridges[69, 70, 71, 72, 73, 74]. Fluctuations of the amplitude of the wave-function have been observed to govern the statistics of the tunnel conductance in the Coulomb blockade regime[79, 69, 73, 80].

The regular regime $E_T/\langle\delta\rangle < 1$, where the level spacing is larger than the Thouless energy, is reached in QDots of radius smaller than the Fermi wavelength or, equivalently, the Bohr radius. In that case, no level repulsion and no chaotic regime is expected. The electronic states follow a regular pattern described by atomic-like quantum numbers 1S, 1P and so on. This regime has been mostly studied through tunneling spectroscopy on colloidal QDots by Scanning Tunnel Microscopy (STM) [59, 60, 61, 62, 63, 64, 65, 66] or on-chip tunnel spectroscopy[58, 67, 68]. STM mapping of the electronic wave-functions has been attempted on colloidal QDots of InAs[61]. As expected in those nanometer-sized QDots of radius smaller than the Bohr radius, the wave-functions had simple spherical and toroidal structures expected for the S and P symmetry respectively.

One major condition for the observation of quantum confinement is that the coupling Γ of the electrodes to the nanocrystal should be smaller than the level spacing δ . As the tunnel resistance is inversely proportional to the coupling, $R_T \propto \Gamma^{-1}$, this also implies that the tunnel resistance should be large. A second condition for the observation of quantum confinement is that the thermal broadening should be smaller than the level spacing.

The study of quantum confinement effects on superconductivity is particularly difficult as superconductivity only arises in metals where the density of states is large and so where the level spacing is very small.

II.1.3 Superconductivity

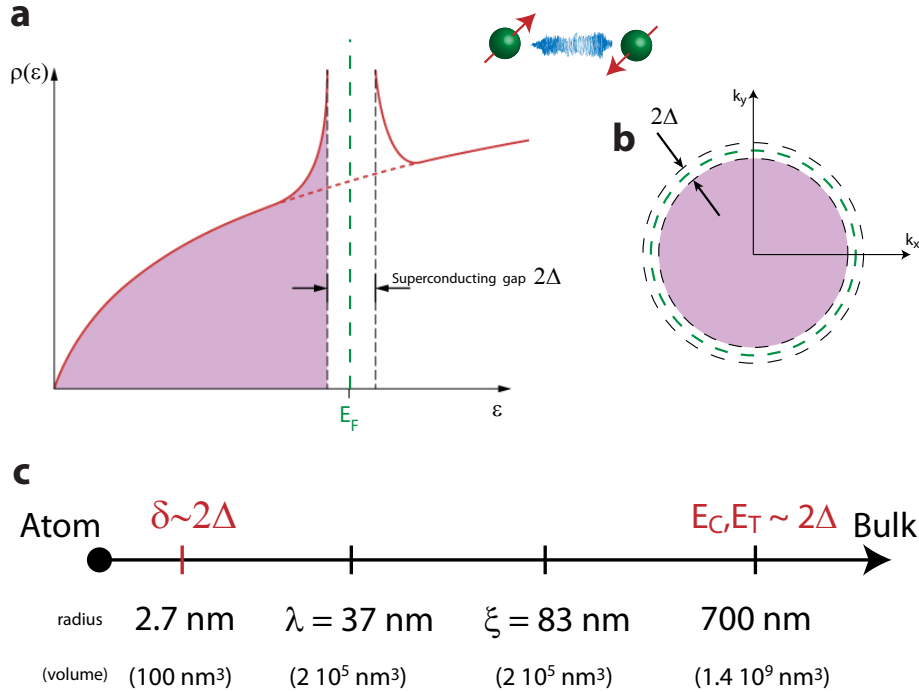


Fig. II.2 a) Density of states as function of energy for a metal (dash line) and a superconductor (continuous line). A gap Δ appears in the superconducting state at the Fermi level. b) Sketch of a Fermi surface in the reciprocal space (k_x, k_y) showing the opening of the superconducting gap all around the Fermi surface. c) Characteristic length scales for a superconducting nanocrystal of Pb.

Superconductivity results from the Bose condensation of electron pairs, the so-called Cooper pairs, into a superfluid condensate described by an order parameter $\psi(r) = |\psi_0|e^{i\phi(r)}$, where the module $|\psi_0|$ is proportional to the Cooper pairs density, i.e. the superfluid density, and $\phi(r)$ is a global phase. This superfluid condensate carries electrical current without dissipation, it is responsible for the null resistance and the perfect screening of the magnetic field, the so-called Meissner effect. The wavelike structure of the superconducting order parameter allows the fabrication of interferometer-like devices such as Josephson junctions. In conventional superconductors such as Pb used in our experiment, electron-phonon interactions are known to be at the origin of the formation of the Cooper pairs. The microscopic theory of superconductivity has been elaborated by Bardeen, Cooper and Schrieffer, leading to the

eponymous BCS theory of superconductivity[81]. One major result of this theory is that the Cooper formation leads to the opening of a superconducting gap Δ at the Fermi level, as sketched Fig. II.2. Theoretically, the amplitude of this gap is related to the superconducting transition temperature through the BCS formula (Eq. (II.3)).

$$2\Delta = 3.5k_B T_c \quad (\text{II.3})$$

For Pb, the gap amplitude is $2\Delta = 2.7$ meV and $T_c = 7.2$ K, which gives for the BCS ratio $2\Delta/k_B T_c = 4.35$, slightly larger than expected theoretically. The existence of this gap at the Fermi level is well established experimentally with different spectroscopic methods such as tunneling spectroscopy, photoemission and infra-red spectroscopy.

To understand my work on the study of quantum confinement on superconductivity, we need to list all the relevant particular lengths of superconductivity. These particular lengths are shown Fig. II.2 for a spherical nanocrystal of radius r . For Pb, the largest particular length is the correlation length $\xi = 83$ nm. This is the characteristic length on which variations and fluctuations of the superconducting order parameter are possible. The second particular length is the London penetration depth $\lambda_L = 37$ nm, which corresponds to the distance on which the magnetic field is screened. In addition, for nanocrystals, two additional lengths must be provided. The longest one is $r_C = 700$ nm which corresponds to the nanocrystal radius below which the Coulomb energy becomes comparable to the superconducting gap energy. With size smaller than r_C and at temperature lower than the superconducting transition temperature, the nanocrystal is in the regime of Coulomb blockade. This length is calculated from the self-capacitance of the nanocrystal. For a nanocrystal of radius r , the self-capacitance is given by $C_{\text{self}} = 4\pi\epsilon_0\epsilon_r r$ and the Coulomb energy is calculated from Eq. (II.1). Finally, the smallest particular length is the Anderson length $r_{\text{Anderson}} = 2.7$ nm. Nanocrystals of radius smaller than this length have a mean level spacing $\langle \delta \rangle$ larger than the superconducting gap energy.

Let's resume the list of size effects on superconductivity, starting from a superconducting bulk crystal. As the radius of the nanocrystal becomes smaller than $r_C = 700$ nm, Coulomb blockade appears but does not alter the superconductivity of the nanocrystal. The Cooper pair condensate still fully exists with bulk-like Meissner effect. Because of the Heisenberg-like relation, $\langle N \rangle \langle \phi \rangle > \hbar$, between the number N of Cooper pairs and the phase ϕ , the Coulomb blockade leads to quantum fluctuations of the global phase of the superconducting order parameter. However, these fluctuations have no measurable effects on the superconductivity of a single nanocrystal. To

observe effects related to these phase fluctuations, devices including more than one nanocrystal coupled through Josephson junctions must be fabricated. Furthermore, upon decreasing the radius below the value of the superconducting correlation length, no effect is expected on superconductivity. Decreasing the radius a little further, crossing the London penetration depth, leads to a reduction in the amplitude of the Meissner effect, which is visible in magnetization measurements. However, the superconducting transition temperature should be identical to the bulk. Finally, only when the nanocrystal reaches the Anderson radius, $r_{\text{Anderson}} = 2.7 \text{ nm}$, do we expect that quantum fluctuations of Cooper pairing will reduce superconducting correlations and lower the critical temperature. This question of Cooper pairing in systems with a small number of fermions is relevant not only to superconductivity in nanocrystals but is also relevant to pairing between nucleons (protons and neutrons) in atomic nucleus[82] or more recently, to the pairing between fermionic atoms in cold atomic traps containing only a few number of atoms[83]. This question has been extensively studied theoretically, in particular, using exact solutions of the Richardson-Gaudin pairing Hamiltonian[84]. These theoretical work have shown that the initial guess by P.W. Anderson in 1959 is correct and that Cooper pairing should be suppressed when the level spacing δ becomes comparable to the superconducting gap energy Δ .

II.1.4 Past works on quantum size effects on superconductivity

Unlike confinement effect that requires nanocrystals of very small volume about $V_{\text{Anderson}} = 100 \text{ nm}^3$, the Coulomb blockade can be observed already in superconducting islands of large size $\approx 1 \mu\text{m}$, which can be obtained through microfabrication. Having a Coulomb energy about 1 meV, experiments in standard dilution cryostat with base temperature of 25 mK enable the observation of the Coulomb blockade in those microfabricated islands.

In the years about 1990-1995, the study of Coulomb blockade in microfabricated superconducting islands led to the discovery of the superconducting parity effect. The energy cost for adding an electron to a superconducting island, i.e. addition energy, depends on the parity of the electron occupation number of the island as a consequence of the formation of Cooper pairs[85, 86]. So far, this parity effect has been observed in large $\sim 1 \mu\text{m}$ microfabricated islands, through direct measurement of the charge capacitance of the island[86], through the even-odd modulation of the addition energy in single electron transistors[87, 88, 89, 90, 91], or the parity dependence of the Josephson current in Cooper pair transistors[92, 93, 94].

The observation of the parity effect is challenging as it requires clean systems, free of impurity states responsible for the so-called quasiparticle poisoning[95, 94].

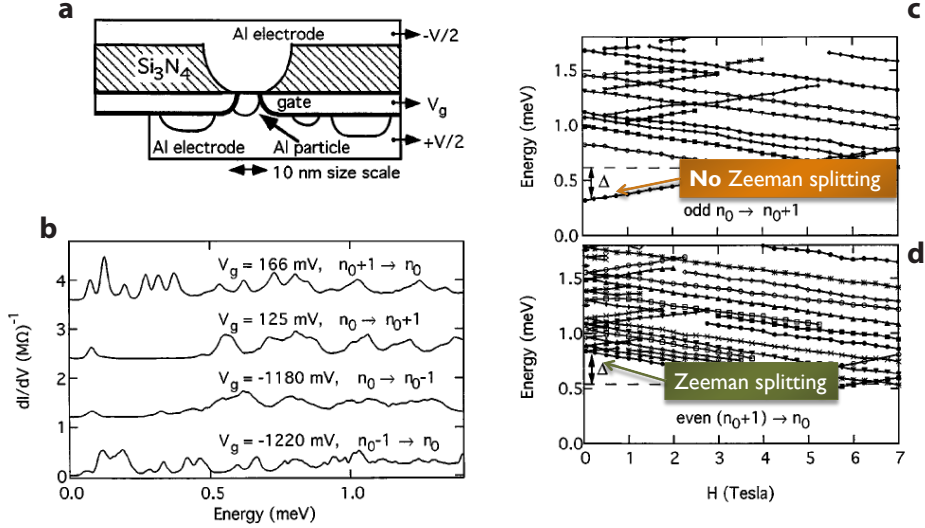


Fig. II.3 a) Nanoparticle of Aluminum located between two electrodes. b) Differential conductance as function of energy for different gate voltages. The curves show conductance peaks that results from the discrete electronic levels in the nanoparticle. c-d) Energy position of the conductance peaks as function of magnetic field. In nanoparticles with odd number of electrons, all electronic levels are doubly degenerate (Kramers theorem) and split under magnetic field as shown panel d. In nanoparticles with even number of electrons, the degeneracy of electronic levels is not protected by Kramers theorem, so generally, the electronic levels are expected not to be degenerate and don't split with the magnetic field.

A major breakthrough in this field occurred a few years later with the work of Ralph, Black and Tinkham, who managed to microfabricate double tunnel junctions circuits including a superconducting grain of Aluminum whose volume was about the Anderson volume[96, 97], shown in Fig. II.3. In these experiments, the $2e$ modulation of the addition energy could not be observed directly, instead, the number parity of a given grain was determined by studying the evolution of the discrete spectrum in an applied magnetic field[98, 99], or by looking for the presence of the superconducting gap in the tunneling spectrum[96, 99]. These results stimulated numerous theoretical works to describe the crossover from the bulk-limit, where Cooper pairs are condensed into the superfluid state, to the nano-sized regime dominated by superconducting fluctuations[100, 101, 102]. In this work by Ralph, Blach and Tinkham, they demons-

trated the persistence of Cooper pairing in nanoparticles of volume about the Anderson volume. However, because of the complicated microfabrication process, they have not been able to establish a curve of the superconducting gap energy and transition temperature as function of nanocrystal volume. This is where STM spectroscopy can be an interesting experimental solution.

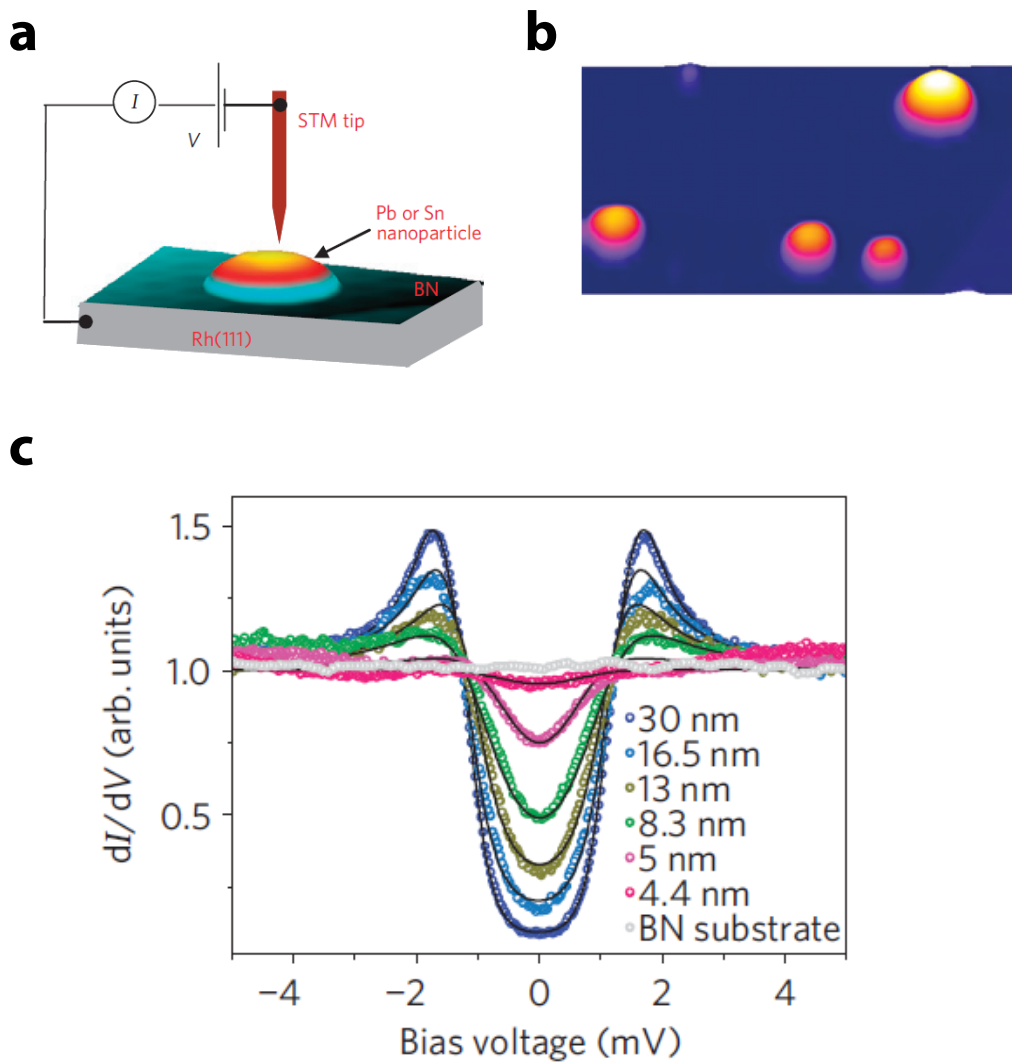


Fig. II.4 a) Schematic of tunneling experiment on Pb or Sn grown on BN/Rh(111). b) STM image of Sn grown on BN/Rh(111). c) Normalized dI/dV curves on Pb nanocrystals of distinct sizes[103].

Using STM, one of the latest most important work in the field has been published

by Bose et al.[103]. As shown in Fig. II.4, they have grown Pb and Sn nanoparticles on an insulating hBN layer deposited on the conducting surface of Rh. Thus, they wanted to use hBN as a tunnel barrier to prevent the strong coupling between the superconducting nanoparticles and the substrate. While they manage to observe the superconducting gap, they did not observe the Coulomb gap. Because the Coulomb energy is much larger than the level spacing δ , the absence of Coulomb blockade also implies the absence of Coulomb confinement in the nanoparticle. For this reason, in this experiment, the disappearance of superconductivity observed in the small nanoparticles may not be related to the Anderson limit but the inverse proximity effect produces by the normal substrate on the superconducting nanoparticle.

Thus, the search of an appropriate system for the study of weakly coupled superconducting nanocrystals through STM spectroscopy was still open at the start of my thesis. We should mention that previous STM works have been attempted on nanoparticles separated of the conducting substrate by a thin tunnel barrier, where the Coulomb blockade was observed. Among most recent works, we should cite the work of C. Brun et al[104], who studied the Coulomb blockade in Pb nanocrystals grown on Ag(111)/NaCl where a thin layer of NaCl separated the nanocrystal from the conducting substrate. While they observed the Coulomb blockade, they did not observe the superconducting parity effect, though.

As we see now, our system, Pb on InAs, is the first one enabling the STM observation of both the Coulomb blockade and the superconducting parity effect. As the superconducting parity effect is easily suppressed by quasi-particle poisoning, our observation of the superconducting parity effect is an indication of the high quality of the system.

II.2 Growth of Lead(Pb) nanocrystals

The Pb nanocrystals are grown on the (110) surface of InAs. As described in the previous chapter, the surface is obtained by cleaving an $\langle 001 \rangle$ oriented substrate in-situ, which is doped with sulfur to a carrier concentration of $N_D \simeq 6 \times 10^{16} \text{ cm}^{-3}$. The Pb nanocrystals are obtained by thermal evaporation of a nominal 0.3 monolayer of Pb on the substrate heated at $T=150 \text{ }^\circ\text{C}$.

As shown on the topographic image in Fig. II.5a, Pb grows in the Volmer-Weber, i.e. island mode[54]. Island growth of metals evaporated on III-V semiconductor has been observed for various elements on GaAs such as Ag[105, 106, 107, 108], Au[109],

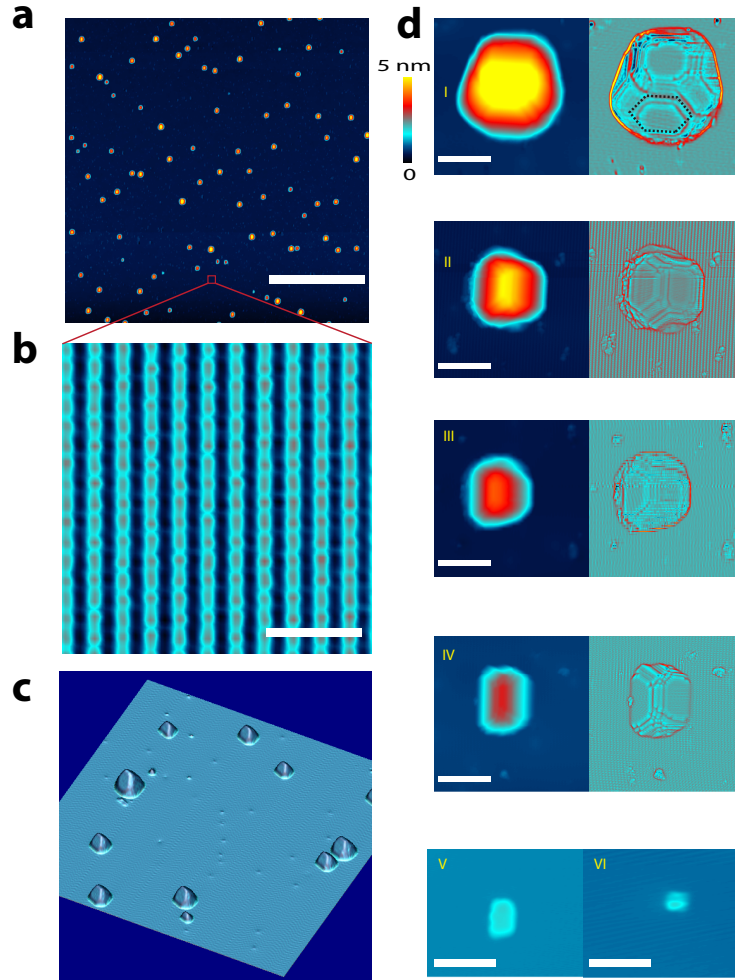


Fig. II.5 a) $1 \mu\text{m} \times 1 \mu\text{m}$ topographic STM image (1 V, 30 pA) of Pb nanocrystals grown on the (110) InAs surface. Scale bar 300 nm. b) $6.5 \text{ nm} \times 6.5 \text{ nm}$ atomic resolution image of InAs (110) zooming around Pb nanocrystals. Scale bar 2 nm. c) 3D $150 \text{ nm} \times 150 \text{ nm}$ topographic STM image (1 V, 30 pA) of Pb nanocrystals grown on the (110) InAs surface. d) Nanocrystals I to VI : 6 topographic images of nanocrystals of different sizes shown with the same x, y and z scales. The volume is decreasing successively from $\sim 800 \text{ nm}^3$ to $\sim 1.5 \text{ nm}^3$. Scale bar 10 nm. Laplacian $\Delta_{xy} z(x, y)$ images of I-IV nanocrystals are shown, in corresponding to the topographic images.

Fe[110] as well as metals on InAs such as Co[111, 112]. The nanocrystals have a size ranging from 800 nm³ to 1.5 nm³, we will focus particularly on the six nanocrystals I to VI shown in Fig. II.5d. Surrounding these nanocrystals, the surface remains free from any adsorbate and atomic resolution on the InAs(110) surface is possible, seen in Fig. II.5b, zoomed from Fig. II.5a.

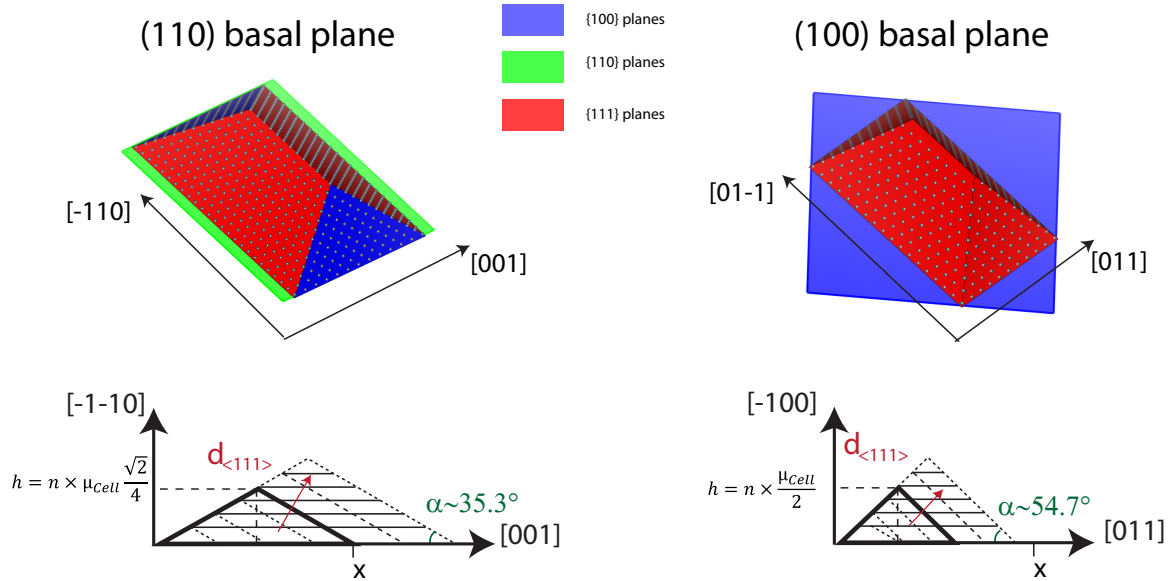


Fig. II.6 Sketch of two pyramidal nanocrystals indicating the main crystallographic directions for (110) basal plane (left) and (100) basal plane (right).

The STM images enable a clear identification of the (111) planes of the Face Centered Cubic (FCC) structure of Pb, thanks to the hexagonal shape of the facets. The nanocrystals have a pyramidal structure with truncated top. Two possible pyramidal shapes are possible with either an (100) basal plane or an (110) basal plane. As sketched in Fig. II.6, these two pyramidal shapes can be distinguished by the angle that the (111) plane makes with the basal plane. To figure out what is the correct basal plane, we are going to plot the height and volume of the nanocrystals as function of their area and compare it with the following simple model.

Knowing the unit cell length $u_{\text{cell}} = 0.495 \text{ nm}$ of Pb, for the pyramid model with base plane (110), the distance between atomic rows along the $\langle 011 \rangle$ directions is :

$$d_{\langle 011 \rangle} = u_{\text{cell}} \times \frac{\sqrt{2}}{4} = 0.175 \text{ nm}$$

and so the height of the pyramid is given by :

$$h_1 = n \times u_{\text{cell}} \times \frac{\sqrt{2}}{4}$$

where n is the atomic rows number.

For pyramid model with base plane (100), the distance between atomic rows along the $\langle 001 \rangle$ direction is :

$$d_{\langle 001 \rangle} = u_{\text{cell}} \times \frac{1}{2} = 0.247 \text{ nm}$$

and so the height of the pyramid is given by :

$$h_2 = n \times u_{\text{cell}}/2$$

We can then calculate the nanocrystal areas :

$$S = x^2, x = \frac{2h}{\alpha}$$

where the angle $\alpha \sim 35.3^\circ$ for the pyramid with (110) basal plane and $\alpha \sim 54.7^\circ$ for the pyramid with (100) basal plane.

The volumes of the nanocrystals are obtained from :

$$V = \begin{cases} S \times h/2, & \text{for pyramid with vertical end faces} \\ S \times h/3, & \text{for pyramid with triangular base} \end{cases}$$

The expected theoretical heights and volumes plotted as function of nanocrystal base area are plotted Fig. II.7 for the two possible pyramid structures of basal planes (110) and (100) respectively. The base area of the nanocrystal is used as the varying parameter because the surface is the quantity measured with the highest precision by STM topography. The surface, the height and the volume of nanocrystals are extracted from the STM topographic images and compared with the theoretical model (110) basal plane and (100) basal plane also in Fig. II.7.

This plot shows that the pyramids with (110) basal plane best describe the data. As the area of the nanocrystal decreases, one sees that the height deviates significantly from the model which reflects that the pyramid have a truncated top. For the volume, the experimental value is obtained with good precision from a flooding method. For

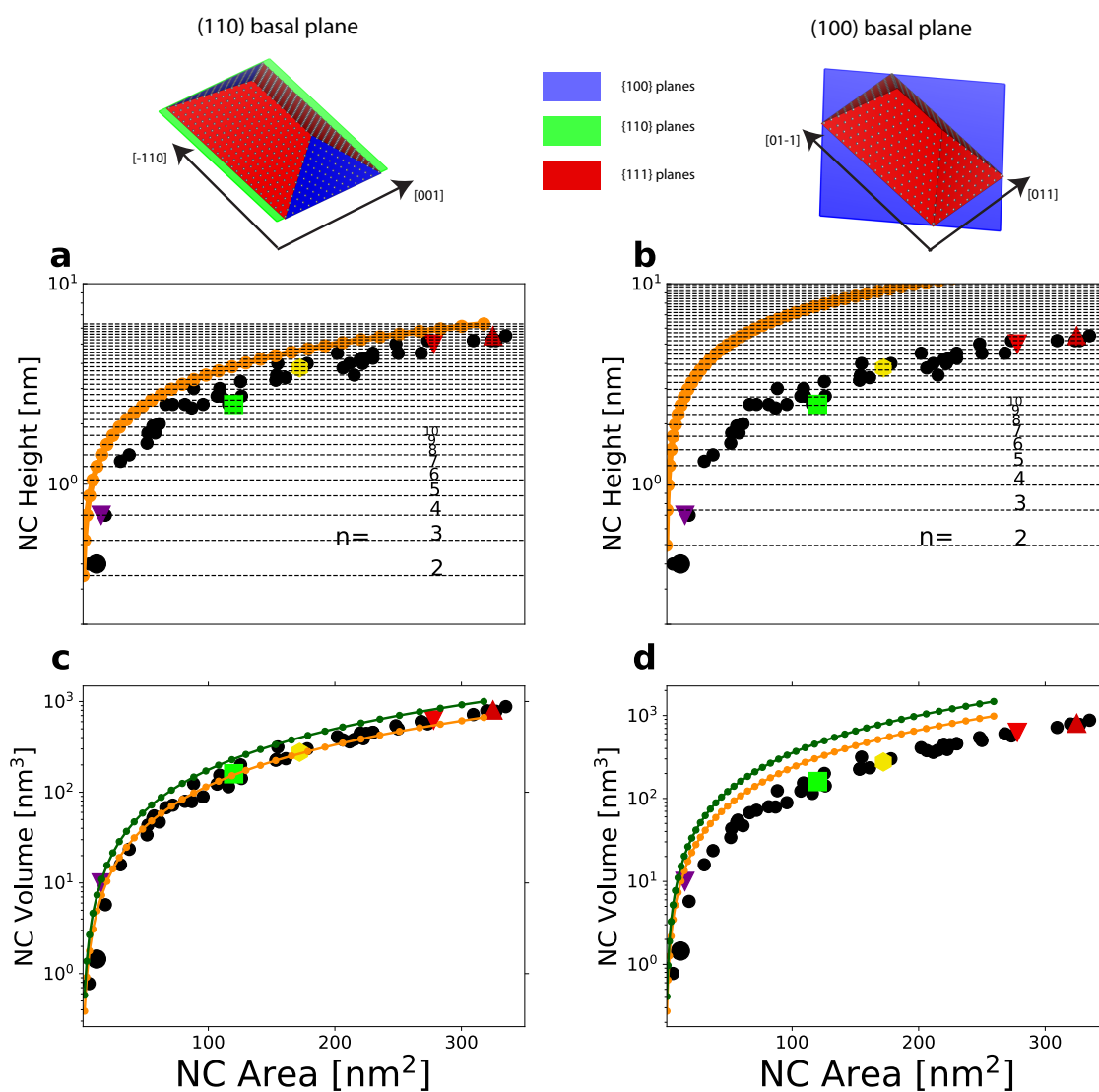


Fig. II.7 Theoretical height and volume of nanocrystals for two possible pyramid structures with (110) basal plane (left) and (100) basal plane (right). They are compared to the experimental values from topographic STM images.

large nanocrystals, the volume is properly described by the theoretical model, deviations are getting larger in small nanocrystals, again because of the truncated top.

	n	Height [nm]	Area [nm ²]	Vol [nm ³]
I	31	5.5	807	324
II	29	5	627	278
III	22	3.8	275	172
IV	14	2.5	160	120
V	4	0.7	10	15
VI	2	0.4	1.5	5

Table II.1 Nanocrystals parameters (volume, height, area) are extracted from the STM images. The effective number of atomic row is calculated from $n_{\text{eff}} = h/d_{(011)}$. For nanocrystals I-IV, the error bar on the volume is 10-20 %. For nanocrystals V and VI, an error bar on the volume by a factor of 2 cannot be excluded, as this corresponds to a change of 25 % for the linear size of nanocrystals.

Table II.1 provides the experimental parameters (height, surface, volume) extracted from topographical STM images for selected nanocrystals I to VI. This table also provides the effective number of atomic rows calculated from $n_{\text{eff}} = h/d_{(011)}$.

II.3 Tip Induced QDot on InAs(110)

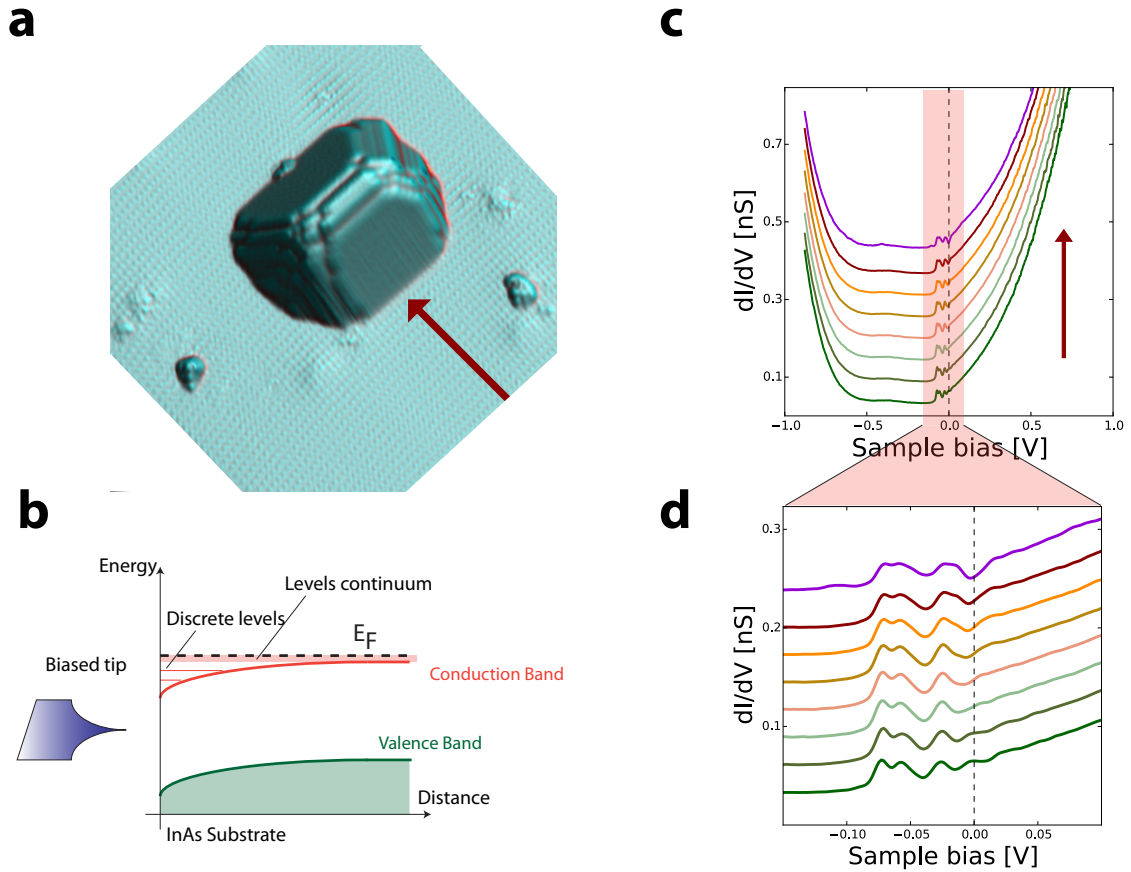


Fig. II.8 a) 3D Laplacian $\Delta_{xy}z(x, y)$ image of nanocrystal IV. b) Sketch of the band bending induced by the tip leading to the formation of a quantum dot. c) Differential conductance as function of sample bias and distance measured along the red arrow shown in a. d) Zoom at low bias showing the conductance peaks due to the discrete levels of the tip-induced quantum dot.

Figure II.8c shows the differential conductance measured on the InAs surface at several distances, from 0 to 10 nm, away from a Pb nanocrystals. This is essentially the same InAs wafer shown in chapter 1. The data are measured at $T = 1.3$ K, unless indicated otherwise, using a standard lock-in procedure. On the differential curves, we can clearly identify the edge of the conduction bands and valence bands. The data indicates that the Fermi level is in the conduction band of InAs as expected for this n doped sample. With a sulphur dopant concentration, $N_D \sim 6 \times 10^{16} \text{ cm}^{-3}$, the Fermi

level is 21 meV above the conduction-band minimum.

A zoom on these spectra, Fig. II.8d, shows multiple peaks that result from the discrete levels of the tip-induced QDot, as discussed in chapter 1 and sketched in Fig. II.8b. Interestingly, we see that the QDot levels are not altered on short distances (< 10 nm) near the nanocrystal. Only a weak broadening of the QDot levels is observed at the approach of the nanocrystal, likely a consequence of their weak tunnel coupling with the Pb nanocrystals. This demonstrates that Pb deposition on InAs does not produce any significant defects and doping. Indeed, the observation of the tip-induced QDot levels indicates that the Fermi level is not pinned at the surface. This would be the case in presence of interface states induced by the nanocrystal.

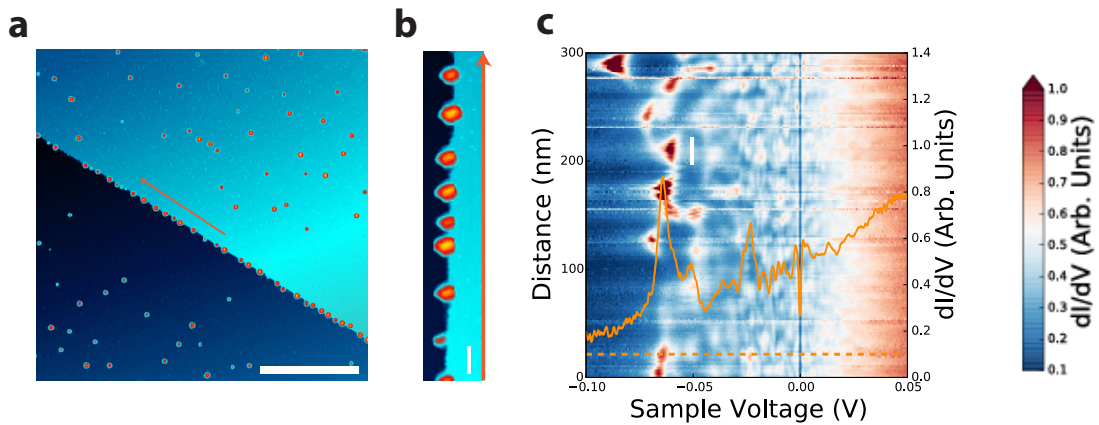


Fig. II.9 a) Large topographic image ($1\mu\text{m} \times 1\mu\text{m}$) showing an atomic step edge against which the nanocrystals agglomerate. The scale bar is 300 nm. b) Zoom on the area near the red arrow in panel a showing aligned nanocrystals along the atomic step edge. The scale bar is 30 nm. c) Differential conductance map as function of sample voltage and distance measured along the red arrow shown in panel b. The scale bar is 30 nm. The orange line is the conductance curve extracted from the map at the location indicated by the horizontal dash line.

Figure II.9 shows a differential conductance map on the energy range $[-100$ meV, 50 meV] as function of distance along a row of nanocrystals that have accumulated along an atomic step edge of the substrate. In this map, one can see that the energy position of the tip induced QDot shift in energy. This is likely a consequence of variations in the electrostatic environment due to the random distribution of Pb nanocrystals and sulphur dopants. These fluctuations are long range (> 30 nm). This length is of the

order of the Fermi wavelength of the 2D electron gas.

II.4 Coulomb blockade and nature of the tunnel barrier

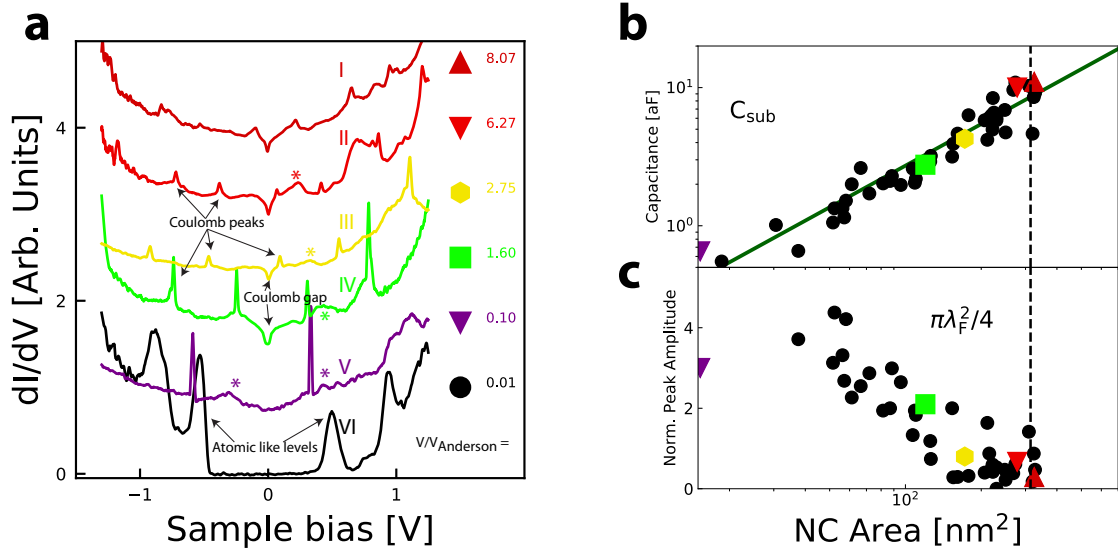


Fig. II.10 a) Differential conductance spectra for the six nanocrystals shown in Fig. II.5. The spectra are indicated in order of increasing volume, in units of Anderson volume. For the largest nanocrystals, I to V, Coulomb peaks and a zero-bias Coulomb gap are observed, as well as quantum well states indicated by stars. For the smallest Pb nanocrystal ($\simeq 0.01 V_{\text{Anderson}} \simeq 1 \text{ nm}^3$), the differential conductance shows only broad atomic like levels separated by a large energy. No Coulomb blockade peaks are observed. b) Substrate-nanocrystal capacitance C_{sub} plotted as a function of nanocrystal area in contact with the substrate. c) Normalized amplitude of the Coulomb peaks as a function of the nanocrystal area. The peak amplitude goes to zero for nanocrystal area approaching $\pi\lambda_F^2/4$ where λ_F is the Fermi wavelength of the 2D electron accumulation layer at the InAs surface.

On nanocrystals of six distinct sizes shown Fig. II.5d, representative differential conductance spectra are shown Fig. II.10a. They display a Coulomb gap at zero bias and sharp Coulomb peaks at higher voltage. Similar differential conductance spectra with sharp Coulomb peaks have been observed previously[113, 114, 115, 116, 117]. The Hanna and Tinkham model[114] can be used to describe the data, as shown Fig. II.11.

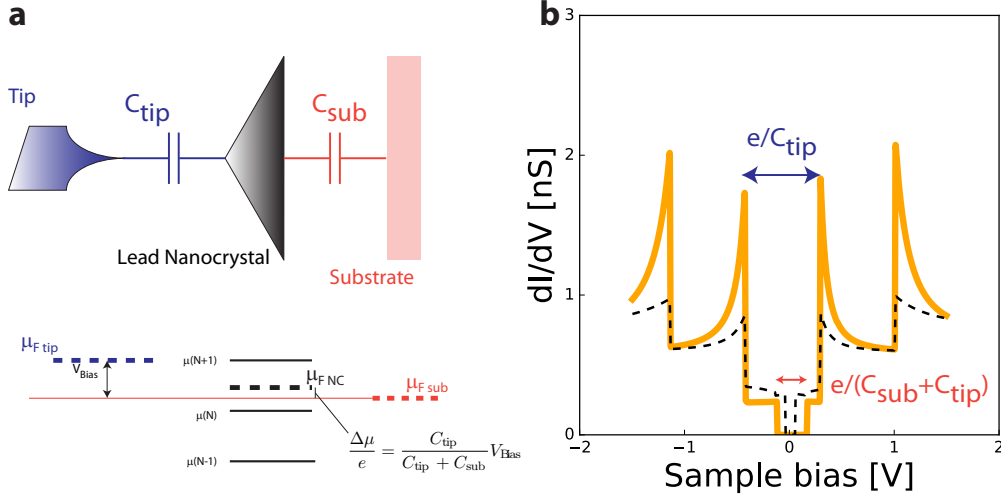


Fig. II.11 a) Schematic of the double junction Tip-Nanocrystal-Substrate displaying the electrochemical potentials for the tip, the nanocrystal and the substrate. b) Simulation of the conductance spectrum using Hanna and Tinkham model[114] for two distinct values of the capacitance C_{sub} , shown by the continuous and dash lines. The voltage interval between the Coulomb peaks do not change with the capacitance C_{sub} , only the amplitude of the Coulomb gap at zero bias changes, as indicated by the double-headed arrow.

This weak coupling model describes four regimes, labelled I to IV, distinguished by the ratio $C_{\text{tip}}/C_{\text{sub}}$ and the fractional residual charge Q_0 on the nanocrystal. For our system Pb/InAs, the tip-nanocrystal capacitance is within the range $C_{\text{tip}} \approx 0.1 - 0.5$ aF, while the substrate-nanocrystal capacitance is within the range $C_{\text{sub}} \approx 1 - 10$ aF. While both values are increasing with the nanocrystal area A , we find that the ratio $C_{\text{sub}}/C_{\text{tip}} \approx 10$ is only weakly changing. This value of the capacitance ratio implies that case III of Ref.[118] applies to our system, where the residual charge has a negligible effect on the width of the Coulomb gap at zero bias.

The Coulomb gap at zero bias results from Coulomb blockade that prevents charge fluctuations in the nanocrystal. As sketched in Fig. II.11a, Coulomb blockade is lifted when the Fermi level of either one of the electrodes is aligned with one of the excited levels of the nanocrystal. Thus the amplitude of the Coulomb gap at zero bias observed in the differential conductance is given by :

$$\delta V_{\text{sub}} = \frac{e}{C_{\Sigma}} = 2 \times \frac{E_C}{e}$$

with the Coulomb energy :

$$E_C = \frac{e^2}{2C_\Sigma}$$

The Coulomb peaks observed at higher voltages result from the shift of the electrochemical potential of the nanocrystal upon increasing the voltage bias across the two junctions. This shift is given by :

$$\frac{\Delta\mu}{e} = \eta V_{\text{Bias}}$$

where the arm lever $\eta = \frac{C_{\text{tip}}}{C_{\text{tip}} + C_{\text{sub}}}$.

Charge states with increased number of electrons become accessible when the electrochemical potential changes by $2E_C$. Thus the voltage difference between two charge states is given by :

$$\Delta V_{\text{add}} = \frac{1}{\eta} \times \frac{2E_C}{e} = \frac{e}{C_{\text{tip}}} \quad (\text{II.4})$$

Reciprocally, the addition energy E_{add} can be obtained from the addition voltage ΔV_{add} through the relation :

$$E_{\text{add}} = \eta e \Delta V_{\text{add}}$$

In this Hannah and Tinkham model, the magnitude of the Coulomb peaks increases with the ratio $R_{\text{tunnel}}/R_{\text{contact}}$, as observed on the differential conductance curves measured as function of tip height above the nanocrystals as shown Fig. II.12. For this nanocrystal, this model shows that the contact impedance is of the order of $R_{\text{contact}} \sim 10 \text{ M}\Omega$, implying that the transmission coefficient $T = R_{\text{contact}}e^2/h = 0.0025$ is weak as expected given that we are observing Coulomb blockade. Equation (II.4) shows that the addition voltage ΔV_{add} depends only on the capacitance C_{tip} and not on the capacitance C_{sub} . Figure II.11b shows a simulation of the conduction spectrum, using the Hanna and Tinkham model [114] for two distinct values of the capacitance C_{sub} . This simulation shows that indeed the addition voltage does not depend on the capacitance C_{sub} .

As we are now convinced that the Coulomb gap at zero bias is only set by C_{sub} , Fig. II.10b shows that C_{sub} extracted from the Coulomb gap at zero bias is a linear function of nanocrystal area A as it should be expected. From this dependence $C_{\text{sub}} =$

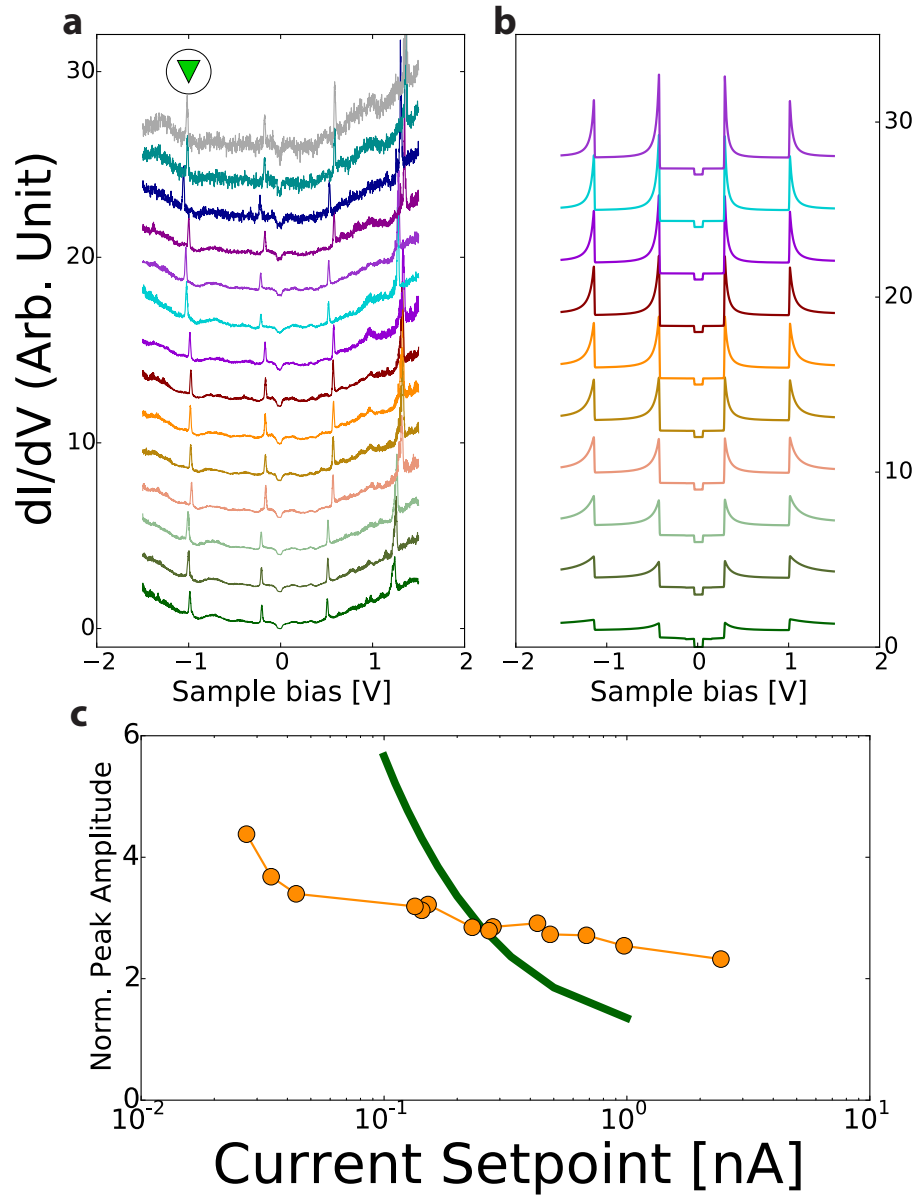


Fig. II.12 a) Normalized and shifted differential conductance curves, measured at different setpoints from $I_{\text{set}} = 5 \text{ nA}$ (bottom) to $I_{\text{set}} = 30 \text{ pA}$ (top). b) Corresponding theoretical differential conductance curves obtained from the weak coupling model. c) Normalized peak amplitude measured experimentally (symbols) compared to the weak coupling model (line).

	Nanocrystals Volume [nm ³]	E_C [meV]	δ_{F1} [meV]	δ_{F2} [meV]	E_{Thouless} [meV]
I	807	14	0.2	0.14	44
II	627	15	0.3	0.18	48
III	275	35	0.6	0.4	63
IV	160	52	1.1	0.7	75
V	10	200	17	11	191
VI	1.5	1040	123	77	364

Table II.2 Nanocrystal volume, Coulomb energy E_C , level spacings δ_{F1} and δ_{F2} calculated for the two Fermi surfaces of Pb and Thouless energy E_{Thouless} for the selected nanocrystals I to VI.

$A\varepsilon/d$, using $\varepsilon = 12.3$, the dielectric constant of InAs one extracts $d = 4$ nm for the effective tunnel barrier thickness. Finally, from the addition voltage, one can also extract the capacitance C_{tip} . Table II.2 shows a summary of parameters extracted for nanocrystals I to VI, i.e. the nanocrystal volume extracted from topographic images, the Coulomb energy calculated from the measured C_{tip} and C_{sub} , the calculated mean level spacing for the two Fermi surfaces of Pb and the Thouless energy.

The observation of Coulomb blockade and quantum confinement on Pb nanocrystals raises the question of the nature of the tunnel barrier. As no dielectric insulator has been deposited on the surface and no Schottky barrier exists at metal-InAs interfaces as discussed in chapter 1 [119, 120], the origin of the tunnel barrier appeared clearly only after we plotted the amplitude of the Coulomb peak, normalized to its base value, as function of nanocrystal area, shown Fig. II.10c. This figure shows that the amplitude of the Coulomb peaks decreases with the increase in nanocrystal area and goes to zero for an area about 300 nm². This decrease in the amplitude of the Coulomb peaks can also be observed on the differential conductance curves shown Fig. II.13 for many nanocrystals, where it can be seen that the smallest nanocrystals have Coulomb peaks of large amplitude while the Coulomb peaks are almost gone in the largest ones.

So why are the Coulomb peaks disappearing for nanocrystals area reaching 300

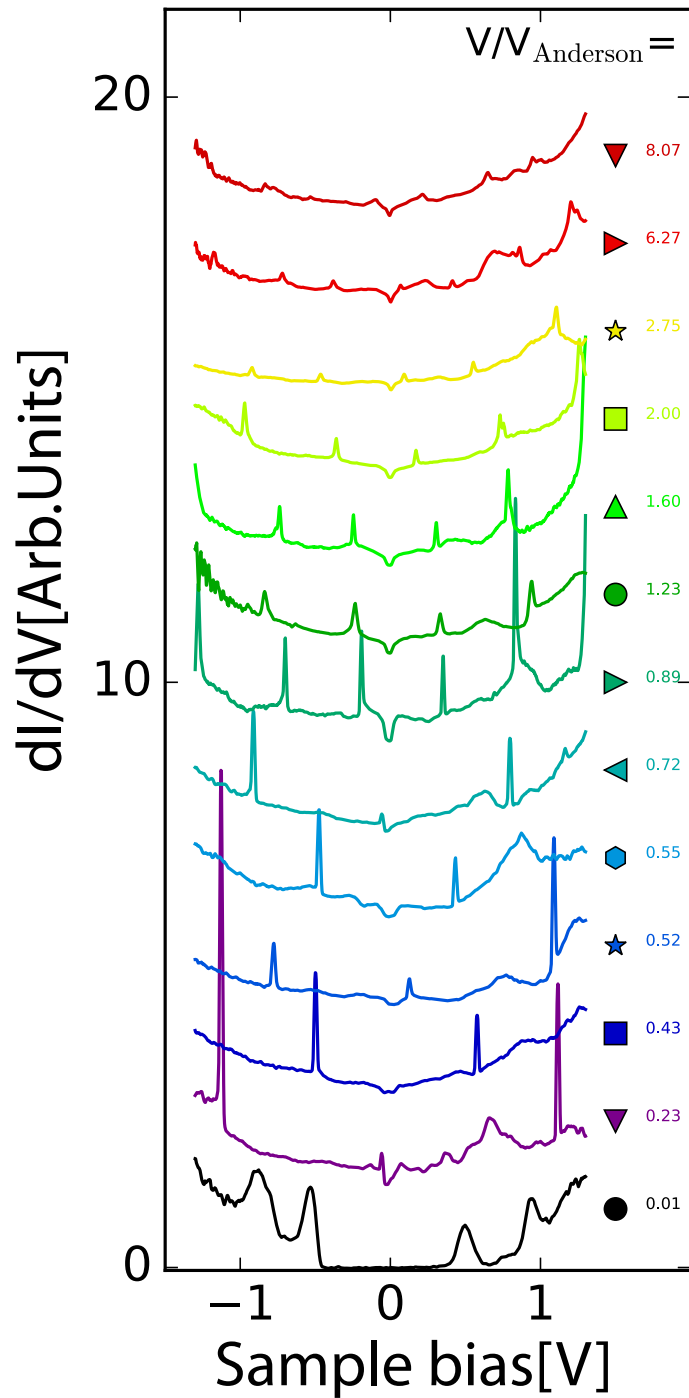


Fig. II.13 For each dI/dV curve, the corresponding nanocrystals and the volume ratio V/V_{Anderson} are denoted on the right of the panel. The spectra are indicated in order of increasing volume, in units of Anderson volume.

nm²? We could imagine that the disappearance is due to the Coulomb energy becoming smaller than thermal broadening. However, we can estimate that, even for the largest nanocrystal, the Coulomb energy is 14 meV, about 10 times larger than thermal energy at $T = 1.3$ K.

If this is not the temperature, then it should be the transparency of the tunnel barrier that is increasing with the nanocrystal area. Knowing that at the interface between the Pb nanocrystal and InAs, the Fermi energy in InAs is at the charge neutrality level, $E_F = 150$ meV, Ref. [119, 120], we can calculate the Fermi wavelength $\lambda_F = 20$ nm of the 2D electron gas that has accumulated below the Pb nanocrystal, as sketched in Fig. II.14a. Thus, we are lead to conclude that despite the absence of a Schottky barrier between the Pb nanocrystal and the 2D electron gas, for nanocrystal of area smaller than the Fermi wavelength of the 2D electron gas, the transmission of the interface is no more ballistic but fall into the tunneling regime.

Thus, in our experiment, the dielectric thickness $d = 4$ nm extracted from C_{sub} above is actually set by the Debye length of the 2D gas and C_{sub} actually corresponds to the quantum capacitance of InAs. Finally, a survey of the literature shows that Coulomb blockade has already been observed in metallic clusters deposited on InAs[121, 111, 112]. The nature of the tunnel barrier was not identified in those works, though.

The crossover from ballistic transport to tunneling transport upon reducing a constriction below the Fermi wavelength is well known from numerous works with quantum point-contacts formed in 2D electron gas[122, 123], where the transmission coefficient T decreases for constrictions smaller than the Fermi wavelength. Thus, in our experiment, because the area of nanocrystal is smaller than $\simeq \lambda_F^2$, their transmission coefficient with the 2D gas is significantly smaller than one, which corresponds to a tunneling regime and explains the observation of the Coulomb blockade. As the area of the nanocrystal increases, the transmission of the tunnel barrier also increases leading to a reduction of the amplitude of the Coulomb peaks. When the area reaches $\simeq \lambda_F^2/4$, ballistic transport occurs between the nanocrystal and the 2D electron gas leading to the disappearance of the Coulomb blockade.

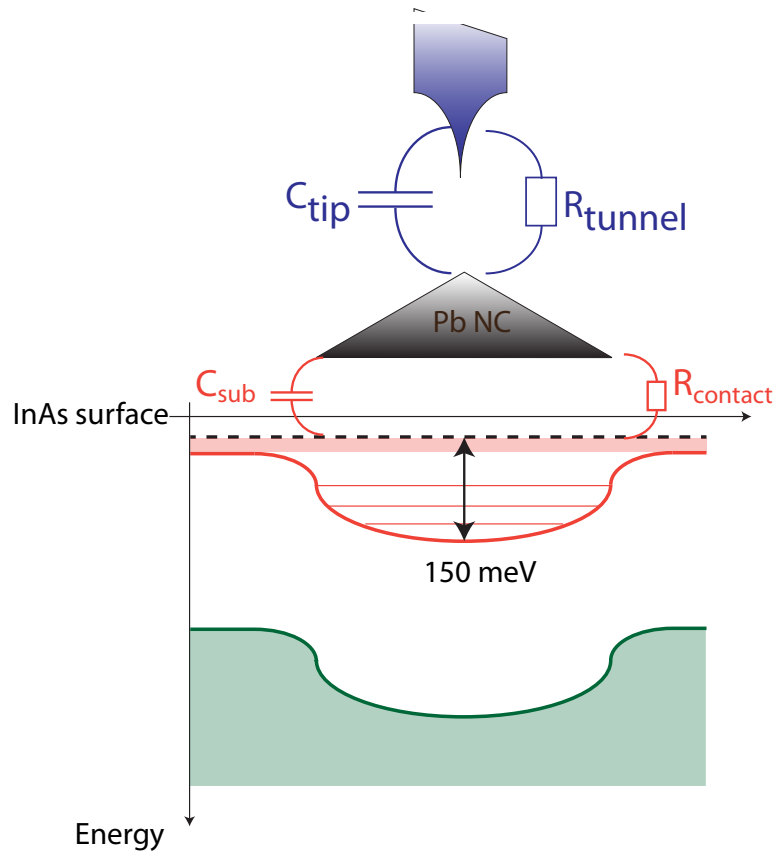


Fig. II.14 a) Schematic diagram of the double junction Tip-Nanocrystal-InAs Substrate. An accumulation of electron should exist below the Pb nanocrystal with a Fermi wavelength about $\lambda_F = 20$ nm.

II.5 From the Superconducting Parity Effect to the Anderson limit

Thanks to this highly clean type of tunnel junction, free from quasi-particle poisoning, the superconducting parity effect in the nanocrystals can be observed through the even-odd modulation of the addition voltage, as shown Fig. II.15d. The addition voltages can be precisely extracted owing to the sharpness of the Coulomb peaks, which voltage positions are obtained through a fit with a Lorentz function, see Fig. II.15e. As sketched in Fig. II.15c, the addition voltage δV_{even} for injecting an electron in an even parity nanocrystal is higher than δV_{odd} for injecting an electron in an odd

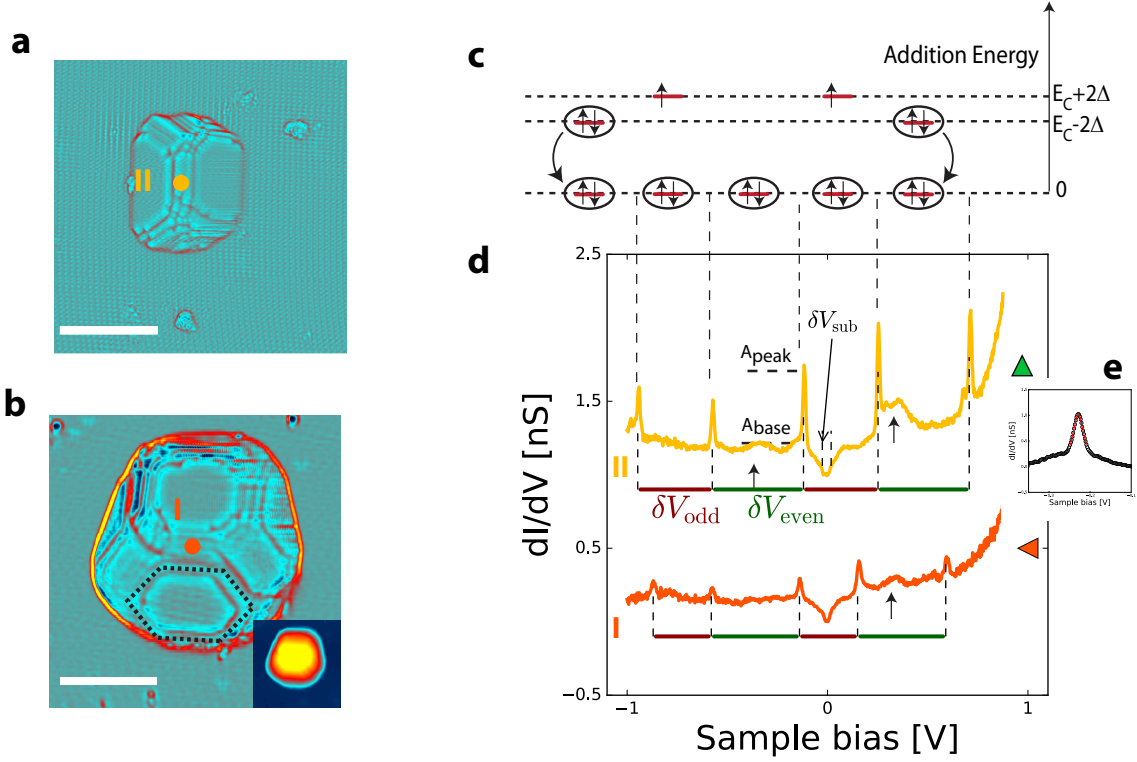


Fig. II.15 a,b) $30 \text{ nm} \times 30 \text{ nm}$ Laplacian $\Delta_{xyz}(x,y)$ topographic images (30 pA , 1 V) of nanocrystals of decreasing size, labeled I and II, where the hexagonal shape of the (111) facets is visible, as shown by the dash line on panel b. Scale bars is 10 nm . The insets show the corresponding topographic STM images. c) Sketch of electron occupation of nanocrystal II. d) Differential conductance measured at centre of nanocrystals I and II. e) Lorentz fit of a single Coulomb peak.

parity nanocrystal, where the energy difference is given by the binding energy of the Cooper pair. This is the so-called superconducting parity effect.

We detail now the calculation of the addition energy for a superconducting nanocrystal, based on Ref. [124, 85].

The total energy of a nanocrystal with N electrons is given by :

$$E(N) = \frac{(Ne)^2}{2C_\Sigma} + E_0(N)$$

$$E_0(N) = \begin{cases} \Delta & \text{for odd } N, \\ 0 & \text{for even } N, \end{cases}$$

The electrochemical potential of a nanocrystal with an even (odd) N ($N + 1$) number of electrons is given by :

$$\begin{aligned}\mu(N) &= E(N + 1) - E(N) = \left(N + \frac{1}{2}\right) \frac{e^2}{C_\Sigma} + \Delta \\ \mu(N + 1) &= E(N + 2) - E(N + 1) = \left(N + \frac{3}{2}\right) \frac{e^2}{C_\Sigma} - \Delta\end{aligned}$$

From these last equations, one obtains the addition energies for a nanocrystal with an even (odd) N ($N + 1$) number of electrons :

$$\begin{aligned}E_{even} &= \mu(N) - \mu(N - 1) = \frac{e^2}{C_\Sigma} + 2\Delta \\ E_{odd} &= \mu(N + 1) - \mu(N) = \frac{e^2}{C_\Sigma} - 2\Delta\end{aligned}$$

Thus, the difference of addition energies between two successive charge states is given by :

$$\delta E = E_{even} - E_{odd} = 4\Delta$$

Finally, the full addition energy for a superconducting nanocrystal is given by :

$$E_{even(odd)} = \frac{e^2}{C_\Sigma} + (-)2\Delta + \delta$$

where the first term is the Coulomb energy, the second term arises from Cooper pairing and the last term is due to quantum confinement.

Figure II.16a shows the differential conductance for a large nanocrystal, $V/V_{\text{Anderson}} = 1.6$, as function of temperature. The corresponding addition voltages, shown Fig. II.16b, are almost equal above $T_c = 7.2$ K, the superconducting transition temperature of bulk Pb. However, an even-odd modulation is observed at low temperature $T = 1.3$ K. The difference in the addition energies between two successive charge configurations is obtained from :

$$\delta E = e\eta(\delta V_{even} - \delta V_{odd})$$

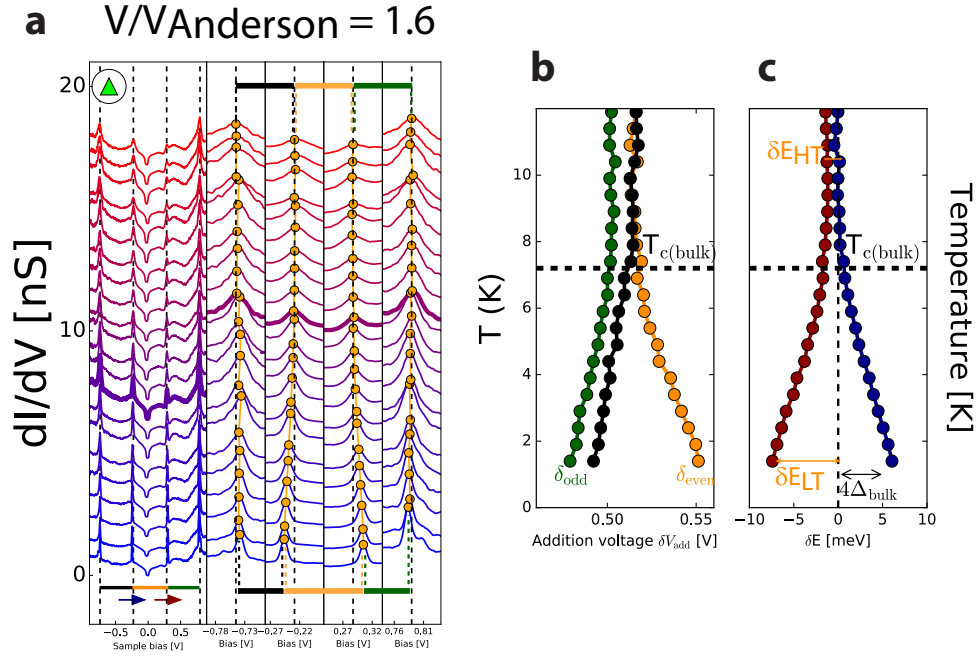


Fig. II.16 Nanocrystal volume $V/V_{\text{Anderson}}=1.6$ a) Differential conductance curves as function of temperature. The voltage separation between the Coulomb peaks, i.e. the addition voltage, is indicated by the horizontal bars of different colors. In the same panel, zoom on the Coulomb peaks are shown where the maxima are indicated by orange dots. b) Corresponding addition voltages plotted as function of temperature c) Addition energy difference between two charge configuration given by Eq. (II.5), where the head (tail) refers to the arrows shown in the corresponding panels. The value $T_{c(\text{bulk})}$ is indicated as a black dash line. A double-headed arrow provides the scale for the energy gap $4\Delta_{\text{bulk}}$ of bulk Pb.

For this large nanocrystal, four Coulomb peaks are observed which provide three distinct addition voltages indicated by the horizontal bars. From these addition voltages, two distinct values of the addition energy difference δE between two charge configurations are obtained and given by :

$$\delta E = e\eta(\delta V_{Head} - \delta V_{Tail}) \quad (\text{II.5})$$

where the Head (Tail) refers to the colored arrows in the panel. These two values of δE are shown Fig. II.16c as function of temperature.

This value is near zero at high temperature, $\delta E_{HT} \sim 0$, and increases below $T_c=7.2$ K to reach, at low temperature, the theoretically expected value $|\delta E_{LT}| \sim 4\Delta_{\text{bulk}}$, Ref. [85], where $\Delta_{\text{bulk}} = 1.29$ meV is the superconducting gap of bulk Pb. The value δE_{LT} changes sign as one goes from the difference between two addition energies $\delta E = e\eta(\delta V_{\text{even}} - \delta V_{\text{odd}})$ to the next difference $\delta E = e\eta(\delta V_{\text{odd}} - \delta V_{\text{even}})$.

For the nanocrystal of volume $V/V_{\text{Anderson}} = 0.89$, shown in Fig. II.17a, while the level spacing δE_{HT} is large, the shift of the Coulomb peaks due to the parity effect is still dominating the temperature dependence and can be observed directly on the raw data and the addition energy difference δE plotted as function of temperature on Fig. II.17c. A line $\delta E_{HT_{\text{ext}}}$ is extrapolated from high temperature and the difference $\delta E(T) - \delta E_{HT_{\text{ext}}}(T)$ gives the temperature dependence of the superconducting gap, Fig. II.17c, which shows that the critical temperature $T_c \simeq 6$ K is smaller than the bulk value. The amplitude of the superconducting gap is obtained from :

$$\Delta = (\delta E(T = 1.2\text{K}) - \delta E_{HT_{\text{ext}}}(T = 1.2\text{K}))/4$$

For this nanocrystal, the superconducting energy gap is about two times smaller than the bulk value, $\Delta = \Delta_{\text{bulk}}/2$.

For the smaller nanocrystal of volume $V/V_{\text{Anderson}} = 0.55$, Fig. II.18, the level spacing δE_{HT} is larger and has a temperature dependence that dominates the shift of the Coulomb peaks with temperature. This shift could be the consequence of thermally induced electro-chemical shifts or temperature dependent strain or electric field effects. While the parity effect is barely visible on the raw data, using the procedure employed for the previous nanocrystal, the temperature $T_c \simeq 5$ K value and the energy gap can be extracted to :

$$\Delta \simeq \Delta_{\text{bulk}}/4$$

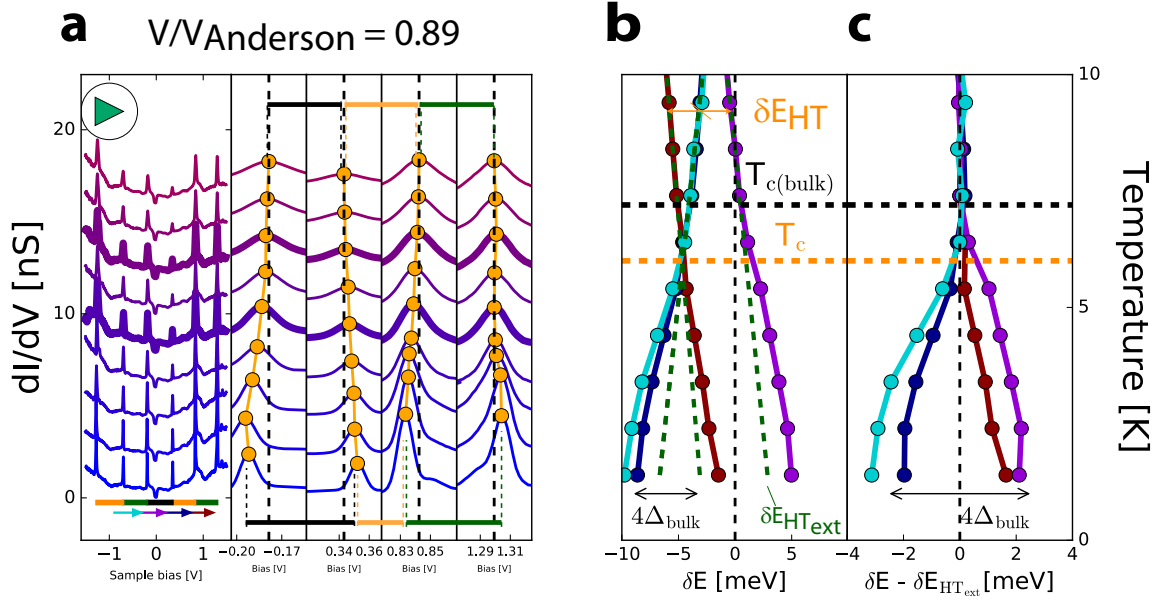


Fig. II.17 Nanocrystal volume $V/V_{\text{Anderson}} = 0.89$. a) Differential conductance curves as function of temperature. The voltage separation between the Coulomb peaks, i.e. the addition voltage, is indicated by the horizontal bars of different colors. In the same panel, zoom on the Coulomb peaks are shown where the maxima are indicated by orange dots. b) Addition energy difference between two charge configuration given by $\delta E = e\eta(\delta V_{\text{Head}} - \delta V_{\text{Tail}})$, where the head (tail) refers to the arrows shown in the corresponding panel a. c) Addition energy difference $\delta E - \delta E_{\text{HT,ext}}$ where the dash green line $\delta E_{\text{HT,ext}}$ is obtained from the extrapolation of δE at high temperature shown in panel b. The value $T_c(\text{bulk})$ is indicated as a black dash line. The extracted T_c are shown as orange dash lines. A double-headed arrow provides the scale for the energy gap $4\Delta_{\text{bulk}}$ of bulk Pb.

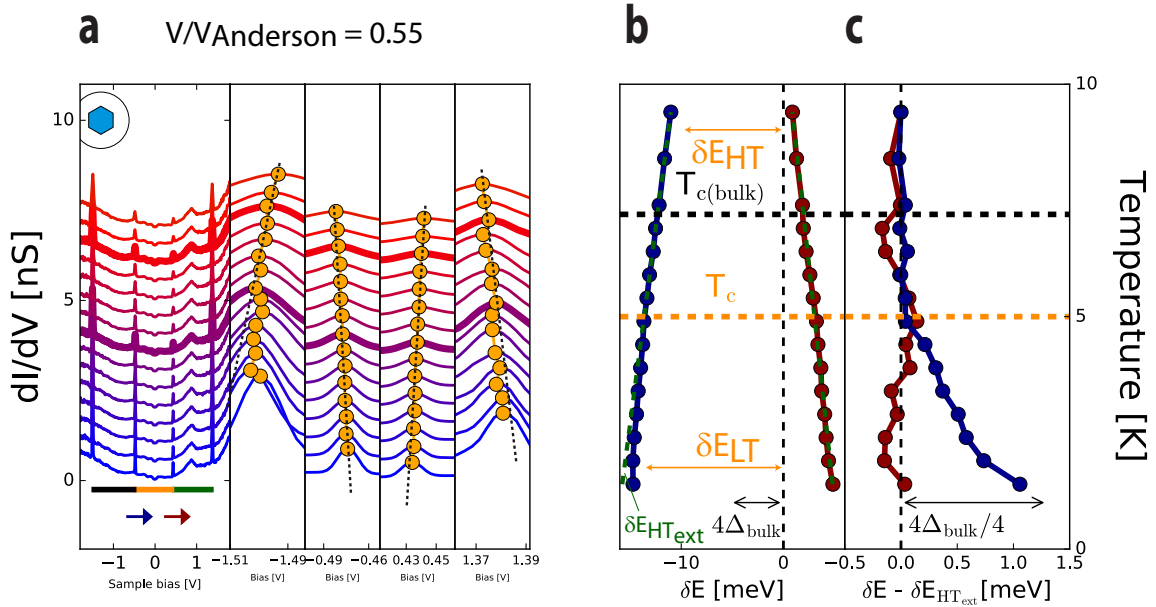


Fig. II.18 Nanocrystal volume $V/V_{\text{Anderson}} = 0.55$. a) Differential conductance curves as function of temperature. The voltage separation between the Coulomb peaks, i.e. the addition voltage, is indicated by the horizontal bars of different colors. In the same panel, zoom on the Coulomb peaks are shown where the maxima are indicated by orange dots. b) Addition energy difference between two charge configuration given by $\delta E = e\eta(\delta V_{\text{Head}} - \delta V_{\text{Tail}})$, where the head (tail) refers to the arrows shown in the corresponding panel a. c) Addition energy difference $\delta E - \delta E_{\text{HT,ext}}$ where the dash green line $\delta E_{\text{HT,ext}}$ is obtained from the extrapolation of δE at high temperature shown in panel b. The value $T_c(\text{bulk})$ is indicated as a black dash line. The extracted T_c are shown as orange dash lines. A double-headed arrow provides the scale for the energy gap $4 \Delta_{\text{bulk}}$ of bulk Pb.

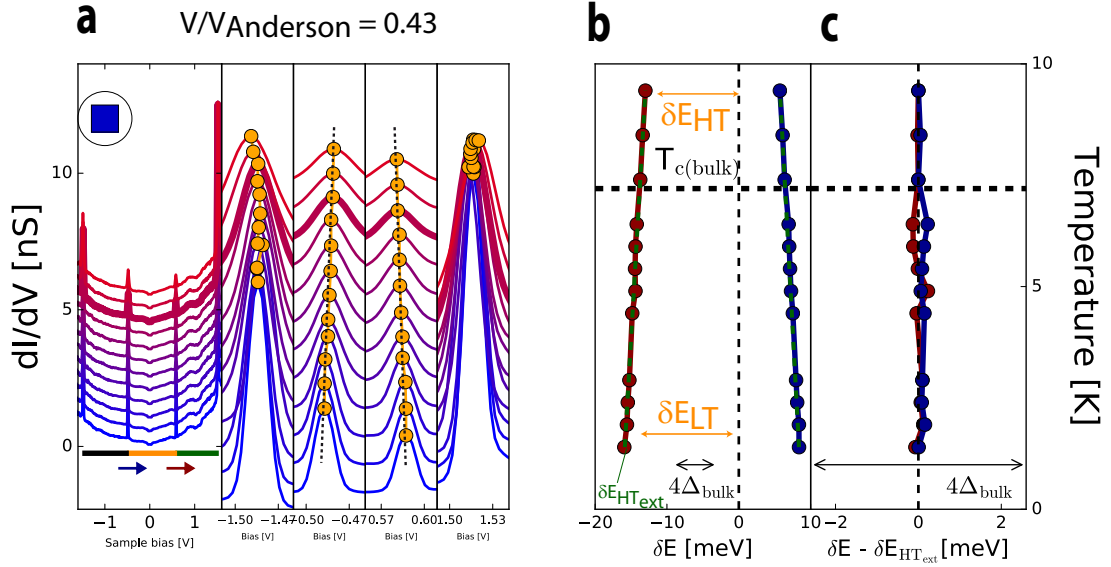


Fig. II.19 Nanocrystal volume $V/V_{\text{Anderson}} = 0.43$. a) Differential conductance curves as function of temperature. The voltage separation between the Coulomb peaks, i.e. the addition voltage, is indicated by the horizontal bars of different colors. In the same panel, zoom on the Coulomb peaks are shown where the maxima are indicated by orange dots. b) Addition energy difference between two charge configuration given by $\delta E = e\eta(\delta V_{\text{Head}} - \delta V_{\text{Tail}})$, where the head (tail) refers to the arrows shown in the corresponding panel a. c) Addition energy difference $\delta E - \delta E_{\text{HT,ext}}$ where the dash green line $\delta E_{\text{HT,ext}}$, is obtained from the extrapolation of δE at high temperature shown in panel b. The value $T_{c(\text{bulk})}$ is indicated as a black dash line.

For the smallest nanocrystals $V/V_{\text{Anderson}} = 0.43$, shown in Fig. II.19. It has the largest level spacing δE_{HT} and, even though the addition energies are measured with much higher resolution than the superconducting gap energy, no parity effect can be observed on Fig. II.19c.

Finally, for all the nanocrystals where the differential conductance curves have been acquired as function of temperature, the level spacing, the superconducting gap energy and the transition temperature are extracted and plotted Fig. II.20a, b and c, respectively. Upon reducing the nanocrystal volume, both quantities display a sharp decrease to zero when the level spacing becomes of the order of the superconducting gap energy, $\simeq 1$ meV. On the top of the figure, all the length scales associated with superconductivity have been indicated. It appears clearly that the disappearance of

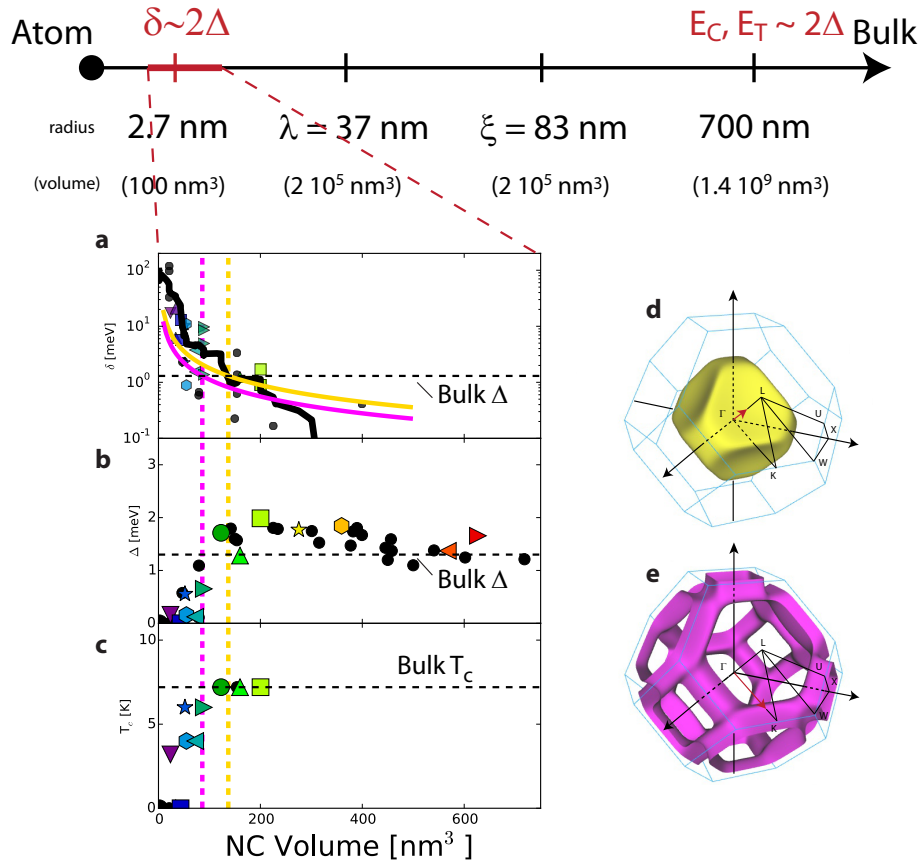


Fig. II.20 a) Level spacing extracted from the addition energies measured above T_c . The experimental data (symbols) are highly scattered as a consequence of the random electronic level distribution. However, the average level spacing, shown by the smoothed black line, is of the order of magnitude of the calculated theoretical values shown as colored lines. The horizontal dash line indicates the bulk superconducting energy gap. b) Superconducting gap Δ extracted from the difference in addition energies between high and low temperature. The horizontal dash line indicates the bulk superconducting energy gap. c) Transition temperature as function of nanocrystal volume. The horizontal dash line indicates the bulk transition temperature $T_c = 7.2$ K. For all panels, the two vertical dash lines indicate the volumes where the level spacing reaches the superconducting energy gap at the wave vectors shown by red arrows on the two Fermi surfaces on the right. The colored symbols identify the corresponding differential conductance curves in the other figures. For the black circles, the differential conductance curves are not shown. d) Fermi surface (FS1) of the hole-type band of Pb. e) Fermi surface (FS2) of the electron-type band of Pb.

superconductivity is related to the Anderson radius and not to any other scale such as the superconducting correlation length. Figure II.20 suggests that superconductivity disappears when the mean level spacing at the Fermi surface of the electron-type band (FS1) increases up to the superconducting gap energy. This is consistent with recent theoretical calculations [125] and STM measurements [126] which have shown that electron-phonon coupling is stronger for this electron-type band owing to its p-d character. Regarding the BCS ratio, within the experimental resolution, no significant deviation from the bulk value has been observed.

II.6 Quantum confinement in Pb nanocrystals

In addition to the Coulomb peaks, the differential conductance curves also display additional peaks resulting from discrete levels induced by the quantum confinement. On the largest nanocrystals I to V, the peaks are of small amplitude, they are indicated by stars in Fig. II.10. On the smallest nanocrystal, labeled VI, no Coulomb peaks are observed but only large atomic-like levels resulting from strong quantum confinement in this atomic cluster. These three distinct regimes of quantum confinement are now discussed in more details.

To identify the origin of conductance peaks indicated by stars in Fig. II.10. Figure II.21a shows a differential conductance map as a function of distance X and voltage on nanocrystal IV, along the arrow shown on the nanocrystal topographic image Fig. II.21d. One can see : first, that the voltage position of Coulomb peaks changes slightly with the tip position above the nanocrystal, as a consequence of the variation in the tip-nanocrystal capacitance C_{tip} ; second, faint local conductance maxima indicated by red dots. Figure II.21b shows differential conductance maps as a function of lateral XY position measured on the square area indicated by thin lines in Fig. II.21d. These maps are plotted only at selected bias indicated by red arrows in Fig. II.21c. These maps show maxima running along the Y direction of the nanocrystal, which is the direction of constant nanocrystal height as sketched Fig. II.21d. This observation indicates that the observed maxima are the consequence of quantum confinement along the vertical direction Z of the nanocrystal. Averaging these maps along the Y direction leads to a differential conductance map as a function of X-voltage, shown in Fig. II.21c, where one sees appearing clear local maxima as in Fig. II.21a. These local maxima correspond to quantum well states whose energy is essentially controlled by the thickness of the nanocrystal. Similar quantum confinement has also been observed for $\langle 111 \rangle$ oriented 2D Pb thin films grown on silicon, where the quantum well states have been observed by photoemission[127] and STM[128, 129].

These quantum well states are also visible in the panel a, indicated by small red dots. The X-voltage coordinates of these states on the differential conductance map Fig. II.21c, labeled by the index (P,n), can be reproduced properly by the simple phase accumulation model[130, 127]. In this model, the condition for a standing wave and the formation of quantum well states is :

$$2k(\varepsilon)Nd_{111} + \delta\phi = 2\pi n$$

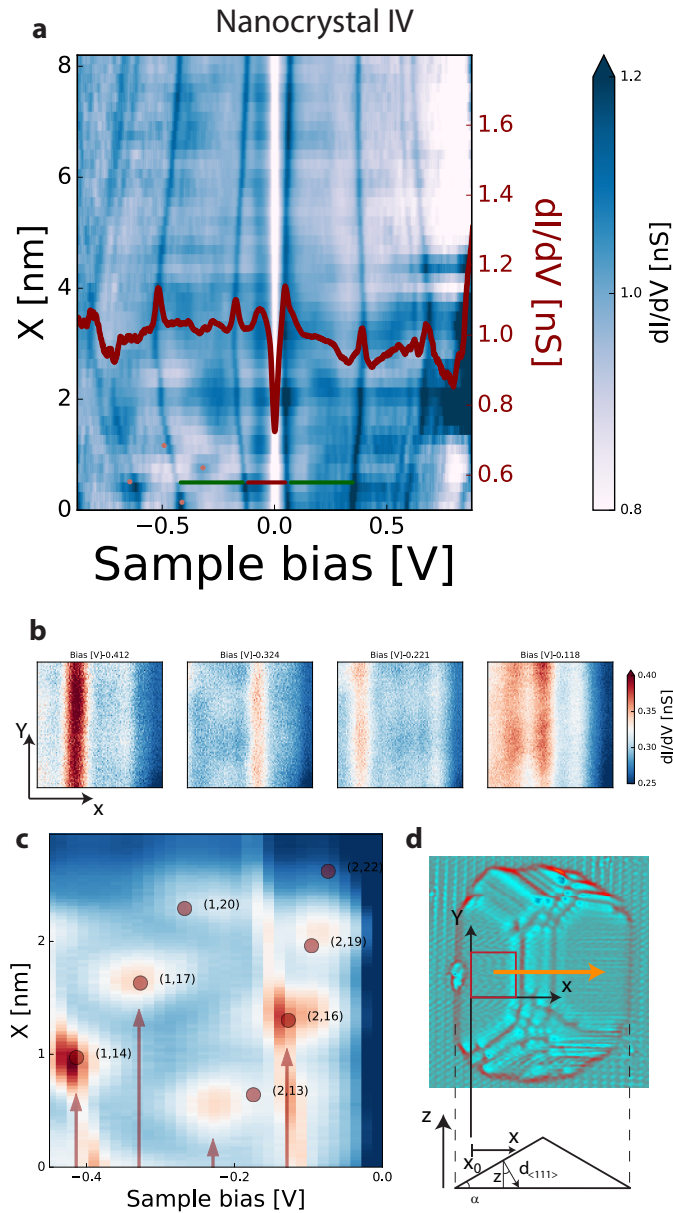


Fig. II.21 a) Differential conductance map as a function of sample bias and direction X measured along the arrow indicated in panel d. The map shows that the energy of the Coulomb peaks change with the tip position as a consequence of the changing tip-nanocrystal capacitance. They also show faint maxima indicated by small red dots. These maxima are seen more clearly on panel c. b) Differential conductance maps measured at different sample voltages on the X - Y area indicated by a red square ($3 \text{ nm} \times 3 \text{ nm}$) on panel d. At these selected voltages, the quantum well states appear as maxima of the differential conductance along the direction X . The voltage position of these maxima does not change along the Y direction. Averaging the differential conductance maps along the Y direction leads to an X -voltage map shown panel c. The vertical red arrows are located at the voltages of the maps shown in panel b.

where N is the number of atomic layers traveled by the electrons in the $\langle 111 \rangle$ direction, n is an integer, and $\delta\phi$ is an additional phase shift experienced by the electron at the boundaries of the nanocrystal. The different families of quantum well states are labeled by the index $P = 2n - 3N$. The energy of the quantum well states changes in the X direction following the change in the length $d_{\langle 111 \rangle}$.

Thus, this Fabry-Perot regime of quantum confinement produces states regularly organized in space and energy and constitutes the regime of quantum confinement observed in large Pb nanocrystals.

For very small nanocrystals, i.e. atomic clusters, such as nanocrystal VI, of volume about 1.5 nm^3 , the differential conductance presents large conductance peaks that result from quantum confinement in all directions of the nanocrystal. This spectrum has an atomic-like look with large energy level separation about almost 1 eV as visible in Fig. II.10a. This atomic-like regime constitutes the regime of quantum confinement observed in atomic clusters.

For intermediate nanocrystal volume about 10 nm^3 between the Fabry-Perot regime and the cluster regime, such as nanocrystal V, the level spacing becomes large enough for the discrete electronic levels to be seen as small peaks in the differential conductance, as indicated by dashed lines on Fig. II.22a. For this nanocrystal, the Coulomb gap at zero bias is about 200 mV. The 6 differential conductance spectra shown in this figure are extracted from a grid of $128 \times 128 = 16384$ spectra taken on the square indicated by dotted lines on the topographic image Fig. II.22b. The location where these 6 spectra have been taken are indicated by symbols on the topographic map Fig. II.22b and differential conductance maps Fig. II.22c. From this spectra grid, one can extract maps of the differential conductance at 8 different voltage values, they are shown Fig. II.22c. The first 6 differential conductance maps are taken at voltage values corresponding to the discrete electronic levels, they show that the amplitude of these small peaks changes with the lateral position on the nanocrystal. The last two differential conductance maps are taken at voltages values close to the Coulomb peak value, they show Coulomb rings that correspond to contours of constant electrostatic energy.

To quantify the number of discrete levels in the nanocrystal, we run an algorithm on all the 16384 spectra to find all local maxima on the voltage range $[-0.275 \text{ V}, -0.025 \text{ V}]$, as shown Fig. II.23a where the local maxima are indicated by red dots. Then, a histogram of the voltage positions of the local maxima is plotted, Fig. II.23b, and shows that there are only 6 well-defined peaks on this voltage range.

This observation of 6 peaks only into the histogram allow concluding that the

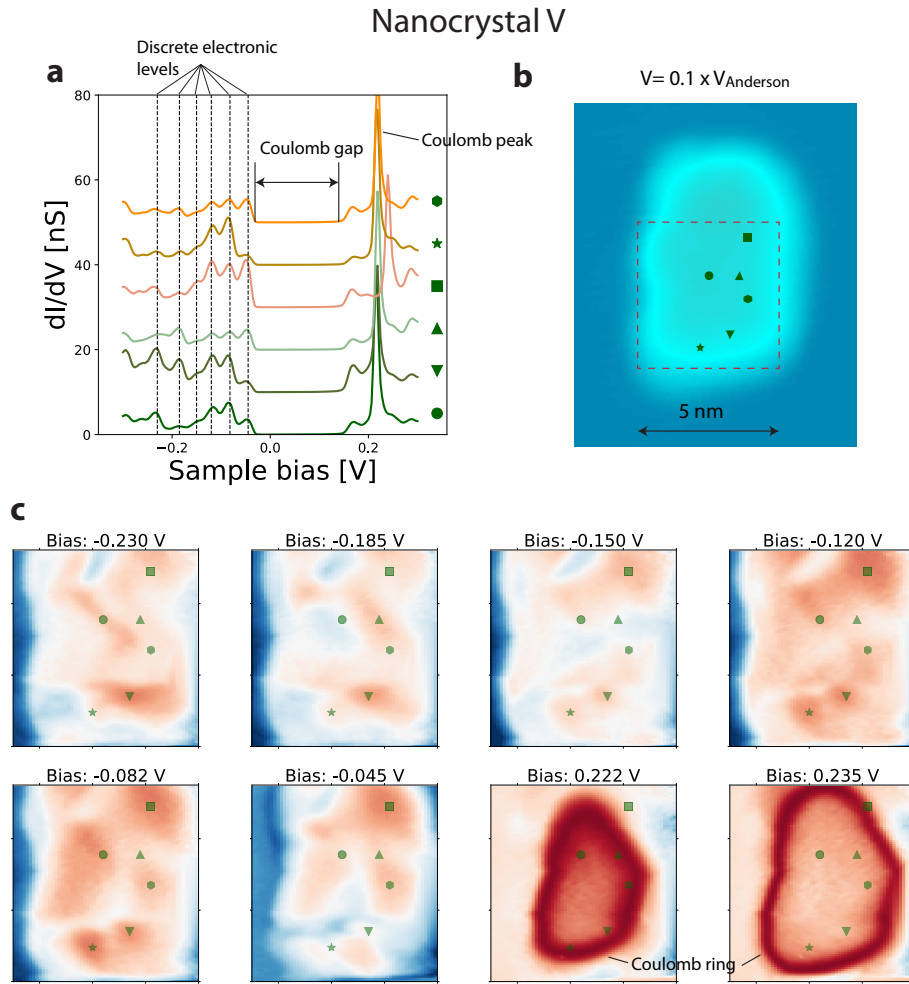


Fig. II.22 a) Differential conductance spectra as a function of sample bias measured at different positions indicated by symbols on the nanocrystal shown panel b). The spectra display a single Coulomb peak, a Coulomb gap and 6 discrete electronic levels. c) Differential conductance maps taken at the different voltages indicated by dash lines on panel a) on the XY area indicated by a dash red square on panel b). The Coulomb peak appears as a Coulomb ring on the differential conductance maps taken at $V_{\text{Bias}} = 0.222$ V and $V_{\text{Bias}} = 0.235$ V.

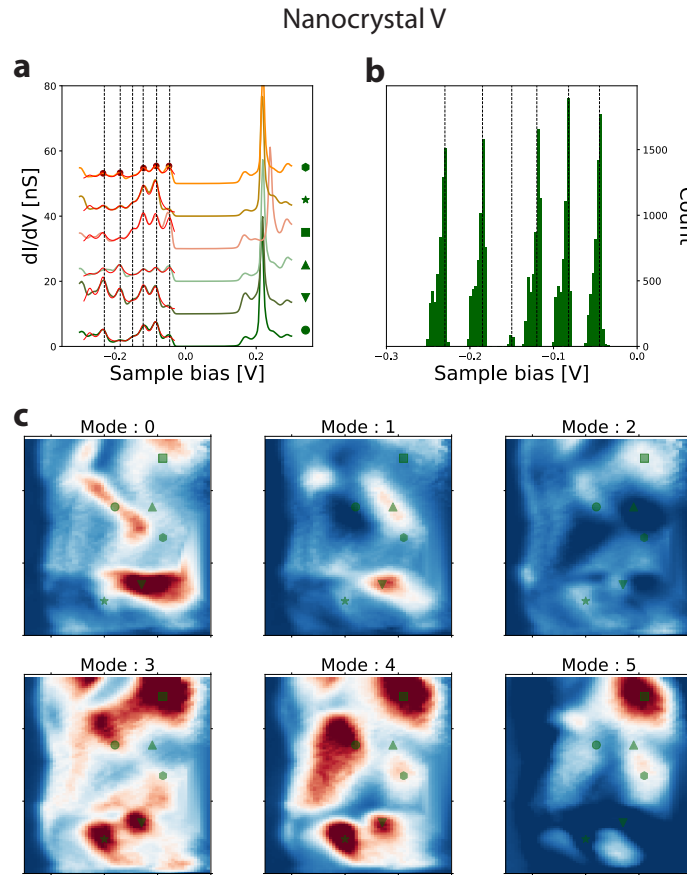


Fig. II.23 a) Differential conductance spectra identical to those shown Fig. II.22a. The local maxima in the differential conductance curve due to the discrete levels are identified by red dots. In the voltage range $[-0.275 \text{ V}, -0.025 \text{ V}]$, the spectra can be fitted by the sum of six Lorentzian centered on the voltage values extracted from the histogram panel b. The fit are shown as thin red curves. The green symbols on the left indicate on the maps shown panel c the XY position where the spectra have been taken. b) Histogram of the voltage positions of the local maxima identified in the 128×128 acquired differential conductance spectra. The histogram shows only 6 well defined peaks indicating that only 6 discrete levels exist on this energy range. These 6 voltage values are used as the voltage positions of the Lorentz functions used to fit the differential conductance spectra, as shown in panel a. c) Maps of the amplitude of the 6 Lorentzian as a function of position XY. These maps can be interpreted as maps of the amplitude of the wave-functions associated with the discrete levels.

electronic spectrum of the nanocrystal can be described, on this voltage range, by only 6 distinct electronic levels. From the voltage difference between the peaks, we find an average level spacing about 35 meV. This value is about 2 times larger than the theoretical value calculated for the Fermi surface FS1 and about 3 times larger than the value calculated for the Fermi surface FS2, see Table II.1. For this small nanocrystal, an error on the volume by a factor of 2 cannot be excluded, as this corresponds to a change for the linear size of the nanocrystal. Furthermore, shell effects or random level distribution effects could possibly explain this discrepancy between the measured level spacing and the expected theoretical mean value. Despite this discrepancy, the small peaks can be safely assigned to single electronic levels within the Pb nanocrystal. To extract the amplitude of the wave-function for each state, we fit the spectrum on the voltage range $[-0.275\text{V}, -0.025\text{V}]$ with the function (II.7), i.e. the sum of 6 Lorentzian describing the 6 levels centered at the energies ε_i identified in the histogram and linewidth $\Gamma = 13\text{meV}$:

$$\rho(V) = \sum_{i=0}^5 \frac{A_i}{(\varepsilon - \varepsilon_i)^2 + \Gamma^2} \quad (\text{II.7})$$

Following the fit of all spectra, we can plot maps of the amplitude A_i of the Lorentzian as a function of the XY position, shown Fig. II.23c. These maps represent the amplitude of the wave-functions associated with the discrete electronic levels.

While mapping wave-functions has already been done previously on InAs QDots [61], where wave-functions of simple spherical or toroidal symmetry were observed, it is the first time that a map of the wave-functions of discrete levels in metallic nanocrystal is presented. In contrast to the QDot InAs, we find that the wave-functions in our metallic nanocrystals have a random structure. This is actually not surprising. As shown in Table II.1, the Thouless energy for this nanocrystal is about 190 meV which is above the energy of these discrete levels, except for the first one. This implies that the states are in the chaotic regime and the wave-functions should have a random structure[77, 78].

II.7 Superconducting proximity effect from the nanocrystals into InAs

When a superconductor is in contact with a conducting but non-superconducting material, such as a metal or doped semiconductor, we can expect that superconducting

correlations from the superconductor will leak into the normal conducting region, this is the so-called superconducting proximity effect[131]. One remarkable consequence of the proximity effect is the generation of a pseudo-gap into the normal region whose amplitude is related to the BCS gap in the superconducting material. As it was already visible in previous Figures such as Fig. II.9, a superconducting gap induced into the 2D electron gas at the surface of InAs is clearly visible in the tunneling spectrum. Obviously, this gap must have been generated by the Pb nanocrystals grown on the electron accumulation at the surface of InAs.

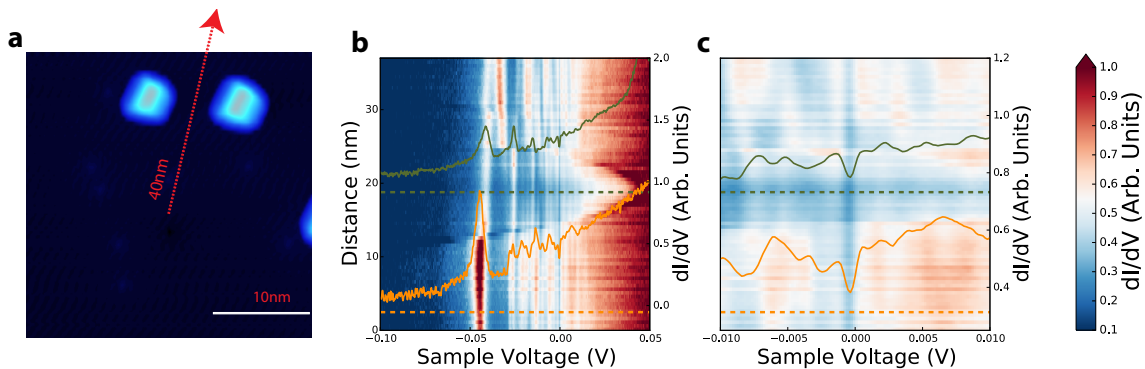


Fig. II.24 a) STM topographic image(1V,15pA). Scale bar is 10 nm b) dI/dV map as function of bias voltage and distance along the red arrow in a. The horizontal dash lines indicate the positions where the two differential conductance curves shown have been taken. c) Zoom of the panel b on the voltage range [-10 mV,10 mV].

We tried to establish a correlation between individual Pb nanocrystals and the superconducting gap observed in the electron accumulation layer. Figure II.24 shows differential conductance maps as function of energy and distance for a trajectory going between two closely spaced Pb nanocrystals. On the map shown on the energy range [-100 meV, 50 meV], Fig. II.24b, we find that the tip-induced QDots are slightly altered by the presence of the nanocrystals. However, on the map shown on the energy range [-10 meV, 10 meV], one cannot establish an obvious correlation between the superconducting gap and the position of the Pb nanocrystals.

The topographic image in Fig. II.25 shows multiple nanocrystals of different size on the InAs substrate. We measured the spectrum near all these nanocrystals and compared it with the spectrum measured on a point of the surface far from any nanocrystals, labeled '0'. On the spectra shown in this figure, we find no obvious correlations between the amplitude of the observed superconducting gap and the presence of the nanoparticle.

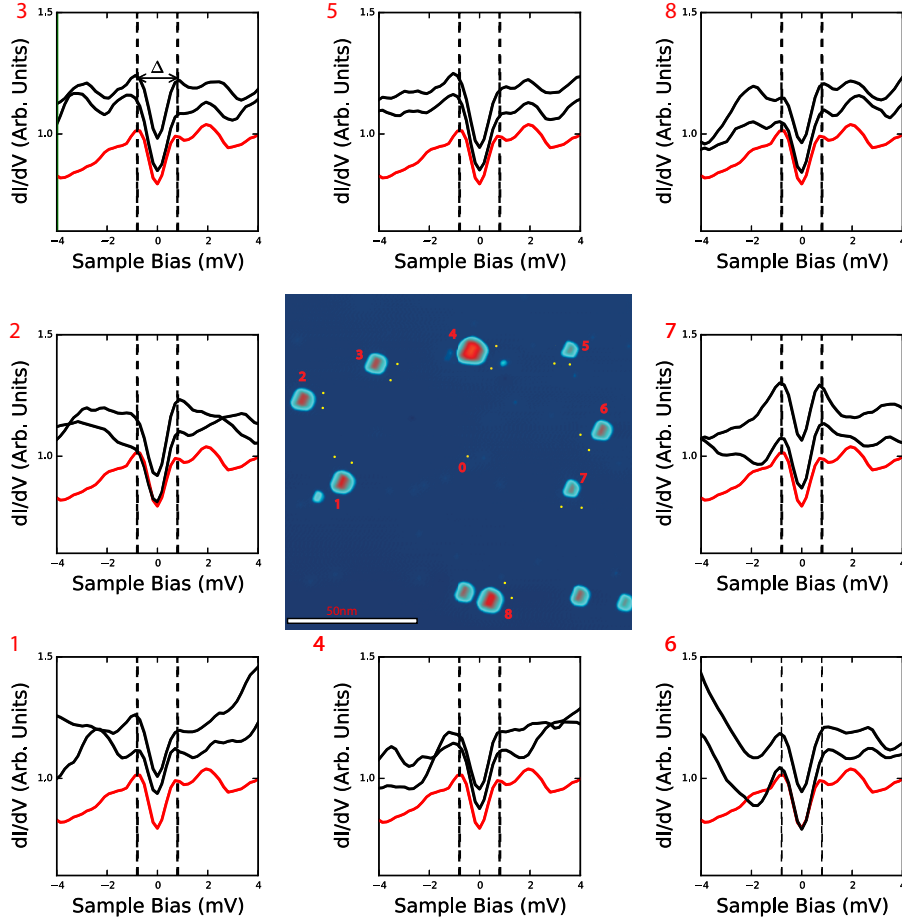


Fig. II.25 Differential conductance curves at distinct locations on $\text{InAs}(110)$ surface near nanocrystals. The red differential conductance curve is measured at the center point labeled with 0.

As we were worrying that the tip may have been polluted by Pb, we repeated the experiment several times with two different tips but repeatedly observed the same superconducting gap induced in the accumulation layer at the surface of InAs .

To finally convince ourselves that this superconducting gap is really induced into the electron accumulation layer, we measured the spectrum as function of tip height, i.e. current setpoint, the result of which is shown in Fig. II.26. This figure shows that the superconducting gap gets deeper as the tip approaches the surface. This seems consistent with the fact that approaching the tip leads to a higher density of states and so a stronger proximity in the surface.

The ubiquitous observation of a superconducting gap everywhere on the InAs surface and the absence of a correlation between the measured gap and the position of the

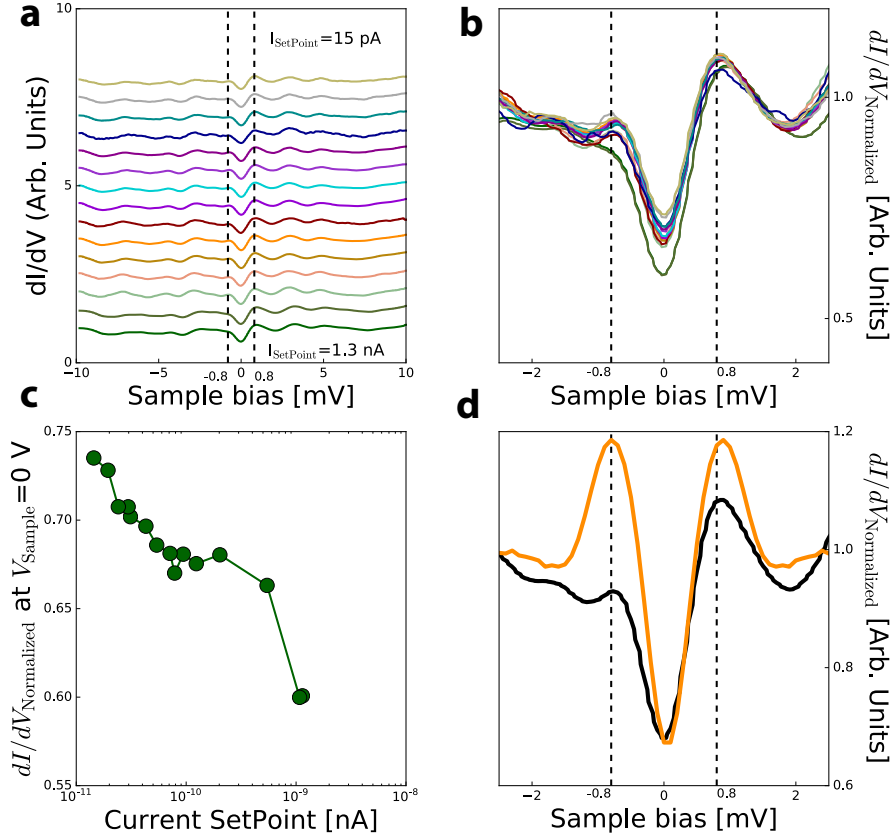


Fig. II.26 a) Differential conductance curves are measured with different current setpoint in the range [15 pA, 1.3 nA]. b) Normalized differential conductance. c) dI/dV values at $V_{\text{bias}} = 0$ are extracted from the normalized curves shown in b and plotted as function of current setpoint. One can see that the depth of the superconducting gap depends on the current setpoint, i.e. the tip position, suggesting that the superconducting gap originates from the 2D electron gas. d) Comparison of the spectrum measured on InAs (black curve) with the theoretical spectrum calculated with the Usadel equations (orange curve) where $x = 1.7 \xi_N$.

II.7 SUPERCONDUCTING PROXIMITY EFFECT FROM THE NANOCRYSTALS INTO INAs61

nanocrystals suggest that the correlation length in the electron accumulation layer is very large, larger than the average distance between the nanocrystal which we estimate to be about 200 nm.

The proximity effect can be analyzed theoretically with the Usadel equations[132]. Following the Refs. [133, 134, 131], the density of states in the normal region can be calculated from :

$$\text{DOS}(E, x) = N(0)\text{Re}(\cos(\theta(E, x)))$$

where x is the distance from the superconductor/normal interface, $N(0)$ is the density of states at the Fermi level in the normal region and :

$$\theta(E, x) = 4 \arctan(\theta_0/4) \exp(-\sqrt{(2\omega/Dx)})$$

where D is the diffusion constant in the electron accumulation layer.

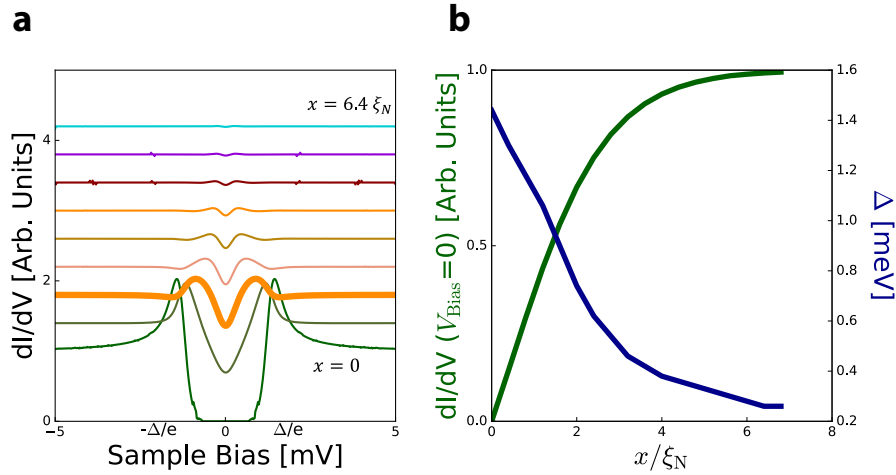


Fig. II.27 a) Simulation of the proximity induced gap in the density of states in the normal region at distinct distances with respect to the interface. The bottom is the nearest to the interface($x=0$), while the top is the most distant($x=6.4 \xi_N$). b) Zero-bias density of states (green line) and superconducting gap (blue line) versus the distance from the S-N interface.

From this model, one can see that the characteristic length for the decay of the superconducting gap in the normal region is given by the Thouless length :

$$\xi_N = \sqrt{\frac{\hbar D}{k_B T}}$$

Given that we don't see any spatial variation of the superconducting gap at the surface of InAs, this suggests that this correlation length ξ_N is much larger than the average distance between the nanocrystals.

II.8 Conclusion

While STM seems an ideal experimental method for the study of quantum confinement effect in nanocrystals grown in UHV, its development was hampered by two contradicting requirements : first, the substrate should be conducting enough to provide a current path to the ground, second, the nanocrystal should be separated from this substrate by a tunnel barrier. Using an InAs substrate presenting an electron accumulation layer of large wavelength ~ 20 nm, we found that nanocrystals of lateral size smaller than this length are in the regime of Coulomb blockade. This results from the constriction of the electronic wave-function across this interface whose lateral size is smaller than the Fermi wavelength, implying that the electronic transmission across this interface drops below unity, even in the absence of any *real* insulating barrier at the interface between the nanocrystal and the InAs substrate. This highly clean tunnel barrier, free from quasiparticle poisoning, enabled the first STM observation of the superconducting parity effect followed by an unambiguous test of the Anderson criterion for the existence of superconductivity.

In addition, this system enabled the observation of discrete electronic levels due to quantum confinement in the Pb nanocrystals. We identified three regimes of quantum confinement. In the largest nanocrystals, we found a Fabry-Perot regime where regular quantum well states are formed due to quantum interference along the $\langle 111 \rangle$ direction of the Pb nanocrystal. In the smallest nanocrystal, i.e. atomic clusters, we found atomic-like electronic levels. Finally, in the intermediate regime, we found the signature of discrete electronic levels in the differential conductance spectra for which we mapped the corresponding wave-functions. We found that these wave-functions had a random spatial structure as expected for nanocrystals in the chaotic regime of RMT. Future works in this direction with higher energy resolution at lower temperature may enable extracting correlations effects from the wave-function amplitude, such as due to Fermi statistics, superconducting correlations or more generally, electron-electron

interactions. This observation of discrete electronic levels in metallic Pb nanocrystals establishes today Pb/InAs as the most suitable system for the study of quantum confinement effects in metallic/superconducting nanocrystals.

Finally, on the electron accumulation layer at the surface InAs, we identify the superconducting gap induced by proximity effect.

This InAs/Pb system offers promising perspectives. A first interesting development would be to keep exploring the quantum confinement in the Pb nanocrystals at lower temperature (<1 K), using a STM microscope with longer autonomy ($>$ week), to make sharper and more detailed maps of the wavefunctions in the nanocrystals. Such studies would enable the study of the complex structures expected for the wavefunctions in those nanocrystals. A second interesting development could be the exploration of this system under magnetic field, to study the evolution of the parity effect with magnetic field as well as the quantum confined states.

III – STM spectroscopy of hinge states in Bismuth nanocrystals

In this chapter, I will describe my work on the STM Spectroscopy of Bismuth nanocrystals grown in UHV on the (110) surface of InAs. This work was motivated by the numerous theoretical and experimental works on Bismuth trying to elucidate the topological nature of bulk Bi. The deposition of a few atomic monolayer of Bi on InAs leads to the formation of nanowires extending along the $[\bar{1}10]$ direction of InAs. At higher Bi thickness, Bi nanocrystals form with well defined crystallographic orientations. Unlike Pb nanocrystals grown on InAs, the Bi nanocrystals are not in the regime of Coulomb blockade as they are strongly coupled to the first atomic layers of Bi covering the substrate. Thus, the differential conductance curves dI/dV can be directly interpreted as measure of the density of states. In maps of the differential conductance taken at different energies, we identified edge-states on the (111) surface of the Bi nanocrystals. While the (111) surface has C_6 symmetry, these edge states have C_3 symmetry, appearing only for 1 edge over 2. This observation has much similarity with the observation of Drozdov *et al.*[135], who identified edge states on atomic-size cavity formed in UHV cleaved (111) surface of Bi. As in our experiment, the edge-states have been found only on 1 edge over 2. In this last paper, it was concluded that the observed edge states were the consequence of the topological nature of the Bismuth bi-layer, as predicted by Murakami[136, 137]. While this theoretical prediction implies that the topological states should exist on all edges, the disappearance of the edge states for every 2 edges was interpreted as a consequence of the coupling of the edge with the bulk Bi. Indeed, two types of edge termination are possible for a [111] oriented Bismuth bilayer. For the type A, the last Bi atom is pointing up, for the type B, the last atom is pointing down. In our experiment, because we can identify the crystallographic orientations of all the facets forming the nanocrystal, we can identify the atomic terminations at the edges of the (111) surface. We found that the edge states

appear most clearly on the type B edge, in contradiction with the scenario proposed by Drozdov *et al.*[135]. It has been suggested recently that bulk Bi could be a 2^{nd} order topological insulator[138, 139] implying the existence of 1D hinge states. These hinge-states have a C3 symmetry and provide a natural explanation for our observation of edge-states with C3 symmetry. To describe this observation in more details, the first section will provide a review on topological materials, the second section will provide a review on the properties of Bismuth, the experimental data and their analysis will be presented in the third section.

III.1 Introduction to topological materials

One major objective of solid state physics is the characterization and classification of states of matter. Many electronic states can be classified through their broken symmetry. For example, the breaking of time reversal symmetry characterizes the apparition of magnetic states, the broken gauge symmetry characterizes the apparition of the superconducting state, and so on.

The limitations of this classification based on broken symmetries started to become apparent with the discovery by Thouless *et al.*[140] that the quantum Hall insulator could be distinguished from the trivial 2D electron gas only by an integer topological invariant. They have shown that this TKKN topological invariant is related to the Hall conductivity $\sigma_{xy} = ne^2/h$ and characterizes its Hamiltonian $H(k)$, defined as a function of k in the Brillouin zone. Later, Haldane discovered that 2D graphene submitted to a periodic magnetic field could also display a topological phase even for an average zero magnetic field[141]. Later, a major breakthrough was obtained with the discovery by Kane and Mele that spin-orbit interaction in graphene leads to the formation of a Quantum Spin Hall insulator, characterized by a Z2 topological invariant[142, 143] and gapless chiral edge-states. The existence of these edge-states is a fundamental consequence of the non-trivial topology, through the bulk-boundary correspondence, which relates the topological class of the bulk system to the number of gapless fermion edge-states on the sample boundary. This theoretical work was followed by the prediction of 2D topological insulator behavior in HgTe/CdTe quantum wells by Bernevig *et al.*[144], in single Bi bi-layer by Murakami[136] and in InAs/GaSb quantum wells by Liu *et al.*[1]. The first experimental observations of the Hall quantification signaling the presence of chiral edge-states has been obtained in HgTe/CdTe quantum wells by Molenkamp's group[145]. This was followed by experiments on this

same system demonstrating non-local transport due to conduction through the edge states[146] and spin-polarization of the edge-states[147]. Later, transport signatures of edge-states were also obtained in InAs/GaSb quantum wells[2, 3, 4, 5].

The effective Hamiltonian describing these two-dimensional systems has the form :

$$H_{eff}(k_x, k_y) = \begin{pmatrix} H(k) & 0 \\ 0 & H^*(-k) \end{pmatrix},$$

$$H(k) = \varepsilon(k) + d_i(k)\sigma_i$$

which is a block-diagonal 4×4 matrix where the two blocks correspond to the two spin polarizations where σ_i are the Pauli matrices and :

$$d_1 + id_2 = A(k_x + ik_y) = Ak_+,$$

$$d_3 = M - B(k_x^2 + k_y^2),$$

$$\varepsilon_k = D(k_x^2 + k_y^2).$$

For an infinite two-dimensional system, k_x, k_y are good quantum numbers, they represent momenta in the plane of the two-dimensional electron gaz and M, A, B, D are material specific constants. Table III.1 provides these values for HgTe[148] and the Bi bilayer[149].

	A (eVÅ)	B (eVÅ ²)	D (eVÅ ²)	M (eV)
HgTe/CdTe (7 nm)	3.65	-68.6	-51.2	-0.01
Bi (1 bilayer)	7.1	69.9	-57.8	0.291

Table III.1 *Materials parameters for HgTe/CdTe quantum wells and Bi bilayer extracted respectively from Ref. [148] and Ref. [149].*

For each spin polarization, the 2×2 matrix $H(k)$ describes the coupling between states of the conduction band with states of the valence band. The gap between the conduction and valence bands are given by $2M$, the mass term of the conduction (valence) band is given by $B_p = B + D$ ($B_m = B - D$). This Hamiltonian can be simply diagonalized to give the band structure of the 2D bulk, the result is shown Fig. III.1a where one can see the conduction and the valence bands separated by the semiconducting energy gap.

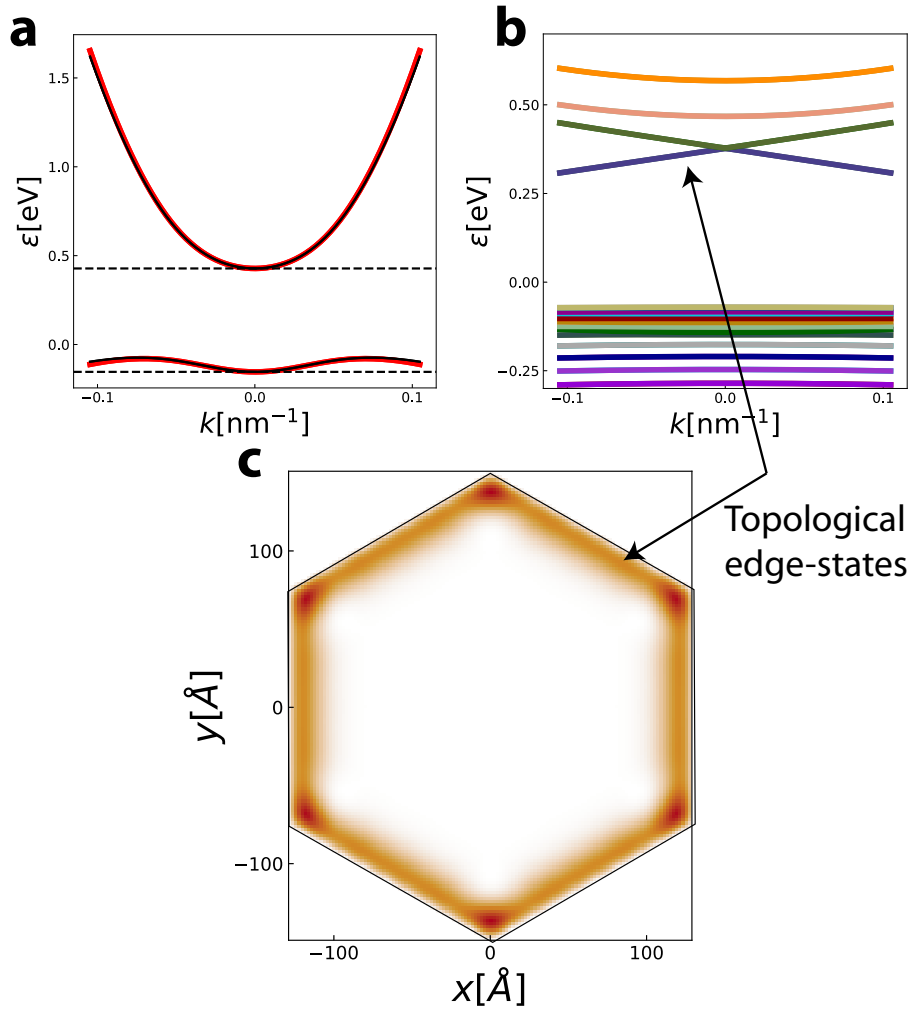


Fig. III.1 a) Dispersion relations $E(k)$ for the Hamiltonian given in Eq. III.1 solved numerically assuming an infinite system. In that case, only bulk states exist that correspond to the valence and the conduction bands. b) Numerical solution of the same Hamiltonian solved on a finite size system shown panel c). In addition to states in the conduction and valence bands, we also identify Dirac states within the band gap. A plot of the wavefunction for one of the Dirac states shows that the state is indeed localized on the edges of the system.

To solve the Hamiltonian on a system of finite size such as the hexagon shape displayed Fig. III.1c, one needs to use a numerical method such as the tight-binding method.

Starting from a crystal described by a Hamiltonian H :

$$H\psi(r) = E\psi(r)$$

One can solve this eigenvalue equation by expressing the wavefunction as a linear combination of atomic orbitals $\phi_n(r)$:

$$\psi_c(r) = \frac{1}{\sqrt{N}} \sum_{n=1}^N c_n \phi_n(r)$$

where $n = 0..N$ is the index of the atomic orbital and c_n are the components of the wavefunction in this basis set $\{\phi_n(r)\}$. N is the size of the basis set, it is given by the number of atomic sites times the number of orbitals per atomic site.

If this basis set is orthonormal, the Schrodinger equation can be written as :

$$\sum_{n=1}^N H_{nm} c_m = E c_n$$

with $m = 1..N$

where the coefficients $H_{nm} = \langle \phi_n | H | \phi_m \rangle$ are the matrix elements on this basis. Assuming that the only non-zero matrix elements are the onsite matrix elements, $H_{nn} = \epsilon_0$, and nearest neighbors matrix elements $H_{nn\pm 1} = \gamma$, the equation III.1 can be written as :

$$\begin{pmatrix} \epsilon_0 & \gamma & 0 & 0 & 0 & 0 & \cdot \\ \gamma & \epsilon_0 & \gamma & 0 & 0 & 0 & \cdot \\ 0 & \gamma & \epsilon_0 & \gamma & 0 & 0 & \cdot \\ 0 & 0 & \gamma & \epsilon_0 & \gamma & 0 & \cdot \\ 0 & 0 & 0 & \gamma & \epsilon_0 & \gamma & \cdot \\ \cdot & \cdot & \cdot & \cdot & \cdot & \cdot & \cdot \end{pmatrix} \begin{pmatrix} c_1 \\ c_2 \\ c_3 \\ c_4 \\ c_5 \\ \cdot \end{pmatrix} = E_c \begin{pmatrix} c_1 \\ c_2 \\ c_3 \\ c_4 \\ c_5 \\ \cdot \end{pmatrix}$$

One then need to diagonalize numerically this large ($N \times N$) matrix. We performed these calculations with the software Kwant[150]. Fig. III.1b shows the calculated spectrum for the hexagonal shape displayed Fig. III.1c. In addition to the electronic states in the conduction and valence bands, this spectrum also displays gapless Dirac states whose corresponding wavefunctions are localized on the edge of the nanocrystal, as shown Fig. III.1c.

Soon after these theoretical works on 2D topological insulators, 3D topological insulators have been predicted[152] where the topological properties are protected by time-reversal symmetry. These 3D topological insulators are characterized not by one

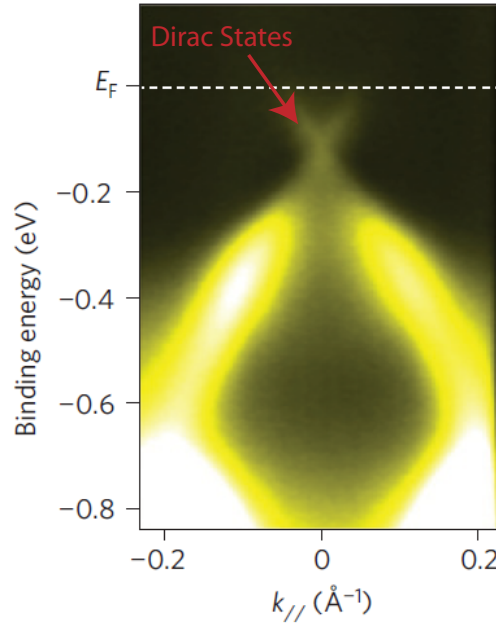


Fig. III.2 ARPES spectrum, extracted from Ref. [151] of the 3D topological insulator Bi_2Se_3 showing the Dirac states.

but four Z2 topological numbers labelled $\nu_0; (\nu_1\nu_2\nu_3)$. When $\nu_0 = 0$ and one of the index ν_1, ν_2, ν_3 is different from zero, the system is a weak 3D topological insulator. When $\nu_0 \neq 0$, the system is a strong 3D topological insulator. Strong topological insulator behavior has been predicted for α -Sn, $\text{Bi}_{1-x}\text{Sb}_x$ and HgTe under strain[153], as well as in tetradymites such as Bi_2Se_3 , Bi_2Te_3 , Sb_2Te_3 [154], in Heusler alloys[155, 156] and in Thallium-based ternary chalcogenides[157, 158, 159]. On these 3D topological insulators, ARPES has been extensively employed to demonstrate the existence of these surface states. They appear as linear dispersion $\varepsilon(k) \propto k$ as expected for the Dirac spectrum of these surface states, as shown Fig. III.2. Finally, the family of topological materials expanded again with the theoretical predictions of topological superconductors and topological semi-metals which come into two flavors, the Weyl semi-metals and the Dirac semi-metals. Numerous review on topological insulators[160, 161, 148, 162, 163, 164], topological superconductors[163, 148, 165, 166, 167, 164, 168, 169] and topological semi-metals have been published[170, 171, 172], as well as several books[173, 174].

Despite the essential role of Bismuth in topological studies, the topological nature of the pure Bismuth remains controversial.

III.2 Electronic properties of Bismuth

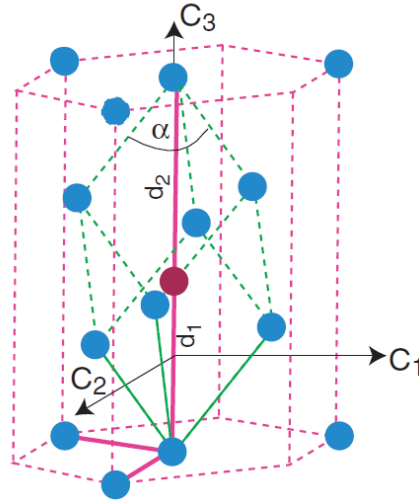


Fig. III.3 Sketch of the Bismuth hexagonal unit cell (dashed red lines) and rhombohedral unit cell (green lines). [175]. In the hexagonal unit cell, three axes are denoted as C_1 , C_2 and C_3 , where the C_3 is the axis of three-fold rotation symmetry.

Bismuth, a group V semimetal, crystallizes with rhombohedral symmetry, of space group $R\bar{3}m$, Fig. III.3. It has two atoms in the unit cell, and from simple electron counting it should be a semiconductor, having an energy gap between the valence band and the conduction band. Due to the slight structure distortion along the trigonal axis, i.e. rhombohedral [111] direction, Bismuth becomes a semimetal with the valence and conduction bands having an approximately 40 meV overlap. As a result the Fermi surface of bulk Bi has small hole pockets at the Γ points and small electron pockets at the L points, as sketched Fig.III.4a. It exhibits a long Fermi wavelength (≈ 50 nm), a long mean free path ≈ 1 mm at 4.2 K, a small carrier density, anisotropic and small carrier effective masses. Each atom has three equidistant nearest-neighbour atoms and three equidistant next-nearest neighbours slightly further away. This results in bilayers of Bi atoms perpendicular to the rhombohedral [111] direction in which each atom is covalently bonded to its three nearest neighbours[175].

A photoemission map of the Fermi surface taken on the (111) surface of Bismuth is displayed in Fig. III.4d and e, extracted from[175]. The observed Fermi surface does not result from the bulk band structure but from surface states. One can actually see two

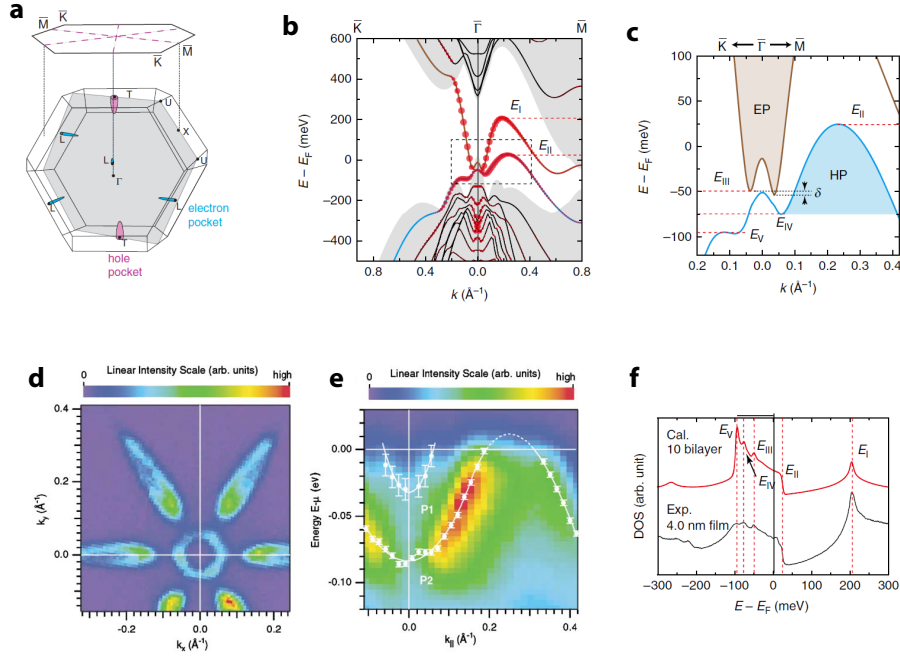


Fig. III.4 a) Bulk Brillouin zone of Bi and projection on the (111) surface. The elements of the bulk Fermi surface are indicated. The surface Brillouin zone has a threefold rotational axis and three mirror lines, shown as pink dashed lines. b) Calculated band structure (solid lines) of Bi(111) surface using a model of 10 Bi bilayers. The surface-state weightings are denoted by the relative size of the red dots. The shadow background is the calculated projection of bulk band structure Ref.[176]. c) Magnified band structure around the Γ point of the dashed rectangle region in panel a. The dashed red lines correspondingly indicate the energy positions of E_i ($i = I, II, \dots, V$), and the dashed black lines in panel c indicate the depth δ of the additional tiny pockets with respect to the E_{III} . d) Photoemission intensity at the Fermi level of Bi(111). k_x and k_y are the parallel components of the electron momentum along the C–M and C–K direction, respectively. (e) Band structure along the C–M direction. From Ref.[177]. f) Calculated density of states (DOS, solid red curve) with a Gaussian broadening of 3.0 meV, in comparison with the experimental dI/dV spectrum (in black) measured by STM on the (111) surface.

different surface-state-derived Fermi surfaces, a hexagonal electron pocket centered at the Γ point and an elongated hole pocket surrounding the hexagonal pocket. For the hole pocket, the Fermi velocity is of the order of $1.3 \text{ eV}\text{\AA}$, while the electron pocket is

much steeper with a velocity of about 3.2 eV\AA . These surface states are topologically trivial, their existence is known for a long time and has been described extensively in Ref. [175]. DFT calculations can reproduce these surface states as shown Fig. III.4b and c.

For a long time, pure bulk Bi was believed to be a topologically trivial system. This belief was based on several calculations[178, 179, 180, 181, 182, 183, 184], which had been considered to agree with angle-resolved photoelectron spectroscopy (ARPES) measurements[177, 185, 180].

However, as mentioned above, it was predicted by Murakami that a single bilayer of Bi should constitute a 2D Quantum Spin Hall insulator[136, 186, 137]. To test this theoretical proposal, several groups have prepared single Bi bi-layer on different substrates, i.e. Bi on Bi_2Te_3 [187, 183, 188], $\text{Bi}_2\text{Te}_2\text{Se}$ [189], and identified the signature of the topological edge states through STM spectroscopy.

Because bulk Bi can be seen as a stack of weakly coupled Bi bilayers, the theoretical prediction of topological edge-states on a single Bi bilayer raises the question of the nature of the crossover from the topological Bismuth bilayer to the trivial bulk Bismuth. It was suggested that multi-bilayer Bi (111) film should exhibit an odd-even oscillation of the topological index with film thickness[136] or that bulk Bi could constitute a weak 3D topological insulator [152].

This question was addressed theoretically through ab-initio calculations by numerous groups. It has been predicted that below 5 bilayers ($\approx 2 \text{ nm}$), Bismuth is a two-dimensional (2D) semiconductor without surface states, while above 5 bilayers, a surface state is present[190, 191]. Furthermore, it was argued that Bismuth should constitute a 2D topological insulator up to 4 bilayer thick[190], and up to 8 bilayer with hydrogen passivation of dangling bonds despite the surface becoming metallic[190]. Above this thickness, Bi should recover a trivial topology[192]. In addition, theoretical works suggested that if bulk Bismuth is topologically trivial for a relaxed lattice structure, it becomes non-trivial when compressed[183].

This theoretical understanding has been shattered by recent experimental works. First, working with bulk crystals of Bismuth, the Yazdani's group identified the signature of edge-states on atomic-size cavity formed in UHV cleaved (111) surface of Bi[135]. The edge states were only found at one edge type, as shown Fig. III.5. These edge states were interpreted as the signature of the topological states resulting from the 2D topological insulator formed by the topmost Bismuth bilayer. The disappearance of the edge states every two edges was interpreted as a consequence of the electronic coupling between the edges and the bulk structure. For an hexagonal cavity on the

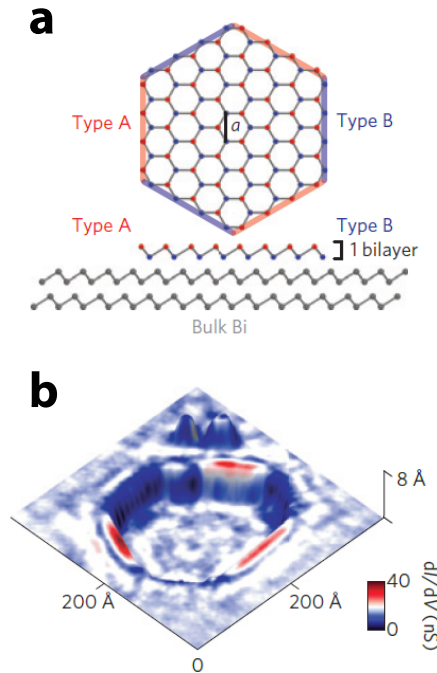


Fig. III.5 a) Edges type A and B in Bismuth bilayers are indicated by red and blue lines respectively. b) False-coloured differential conductance map at energy 183 meV [135].

(111) surface of Bismuth, it can be shown that the last atom can either point up (type A) or down (type B), with these two edges alternating around the Bi cavity. Thus, to explain their experimental observation, the Yazdani's group suggested that the edge states were appearing only on the type A edge, which is only weakly coupled to the bulk Bismuth. Later, it was found in Bi nanocrystals grown on superconducting Nb[193] that edge states appear on all edges but with different energies. In addition, recent high-resolution ARPES result suggest the surface bands are actually different from previously calculated ones and that Bi possesses a nontrivial topology[194, 195, 196]. Topologically protected edges states are also suggested from transport measurements in Bismuth nanoribbons[197, 198] and superconducting interference effects in Bismuth nanowires[199, 200].

Thus, while these last experimental work seem in contradiction with the earlier theoretical work indicating that bulk Bismuth is topologically trivial, the recent theoretical development of higher-order topological insulator[201, 202, 203, 204, 138], seems to provide a natural explanation for the observation of edge states in bulk Bismuth crystals.

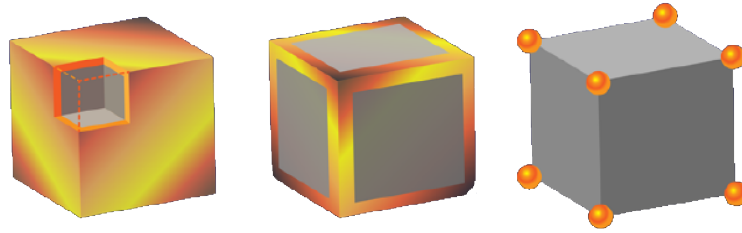


Fig. III.6 Figure extracted from Ref. [205]. 3D topological insulators conduct via gapless states on their 2D surfaces but are insulating in their bulk (left). Second-order and third-order 3D topological insulators have gapless states on their 1D hinges (middle) or 0D corners (right), respectively.

While usual topological insulators are electronic insulators in their d -dimensional interior (bulk) but allow metallic conduction on their $(d - 1)$ -dimensional boundaries. The *higher-order* topological insulators[138] have $(d - 1)$ -dimensional boundaries that, unlike those of conventional topological insulators, do not conduct via gapless states but instead are themselves topological insulators. As sketched Fig. III.6, an n^{th} order topological insulator instead has gapless states that live on $(d-n)$ -dimensional subsystems. For instance, in three dimensions, a second-order topological insulator has gapless states located on 1D *hinges* between distinct surfaces, whereas a third-order topological insulator has gapless states on its 0D corners. So far, higher-order topological insulator with hinge states have been predicted explicitly for the materials SnTe[138] and bulk Bi[139].

III.3 Growth of Bismuth nanocrystals

Among all possible adsorbates on III-V (110) surface, the group-V semi-metals (Sb, Bi) are particularly interesting. Room-temperature deposition of a monolayer of Sb or Bi on III-V (110) surfaces leads to an epitaxial (1×1) structure with a one-to-one correspondence between the substrate and overlayer atoms, with the semimetal continuing the III-V bulk structure to give a so-called epitaxial continued layer structure, ECLS[206, 207].

Annealing of a Sb- or Bi-thick layer results in the desorption with the exception of the first semimetal monolayer, giving rise to stable and highly ordered 2D systems[208, 209].

While Sb always provides (1×1) highly ordered structures, bismuth can present

novel superstructures upon thermal treatment[210, 211]. Bi on GaAs (110) results in a poorly commensurate adlayer, with regular dislocations with missing Bi chains every six unit cells[210]. Considering the strain in the Bi/GaAs(110) system, a larger surface unit cell could better lodge Bi to form a long-range-ordered structure. Appropriate thermal annealing of a few monolayers of Bi deposited on InAs (110), GaSb (110), and InSb (110) surfaces, leads to a partial desorption of the semimetal and to the appearance of a distinct (1×2) low-energy electron diffraction (LEED) pattern[211, 212].

Bismuth nanocrystals are grown on the (110) surface of InAs. The surface is obtained by cleaving an $\langle 001 \rangle$ oriented substrate in situ, which is n doped with sulfur to a carrier concentration of $N_D \simeq 6 \times 10^{16} \text{ cm}^{-3}$.

Bismuth nanowires and nanocrystals are obtained by thermal evaporation of 2.5 monolayers of Bismuth on the substrate heated at $T=150 \text{ }^\circ\text{C}$. Then, the sample is annealed at $T=150 \text{ }^\circ$ and monitored with LEED until the Bi (1×2) reconstruction pattern appears after about one hour of annealing. This leads to nicely crystallized Bi nanocrystals deposited on a monolayer of Bi nanowires oriented in the $[110]$ direction of InAs, as shown in Fig. III.7.

The nanocrystals fall in one out of four characteristic shapes that are shown Fig.III.8. The (111) plane is easily recognizable with its characteristic hexagonal shape. The evolution from one shape to the other can be followed and we can recognize all the crystallographic planes, the (111) but also the (100) and the (110) planes. As for the (111) surface, the (100) face is also a pseudo-cubic (111) surface, i.e. giving hexagonal facets. In contrast, the (110) face is a pseudo-cubic (100), i.e. providing tetragonal facets. The identification of the (110) and (100) facets of the Bi nanocrystals is a major result of this work as it allows the identification of the atomic terminations of the edges of the (111) facet.

III.4 Scanning Tunneling Spectroscopy of Bismuth nanocrystals

We performed STM spectroscopy at low temperature $T \simeq 1.3 \text{ K}$. For this study, we made spectroscopic maps of about 12 nanocrystals. Representative results are shown Fig. III.10 and Fig. III.11 for four nanocrystals, labelled I to IV.

As shown in Fig. III.10ab, the differential conductance spectra taken in the middle of the (111) faced, indicated by a black dot, has similar characteristics to differen-

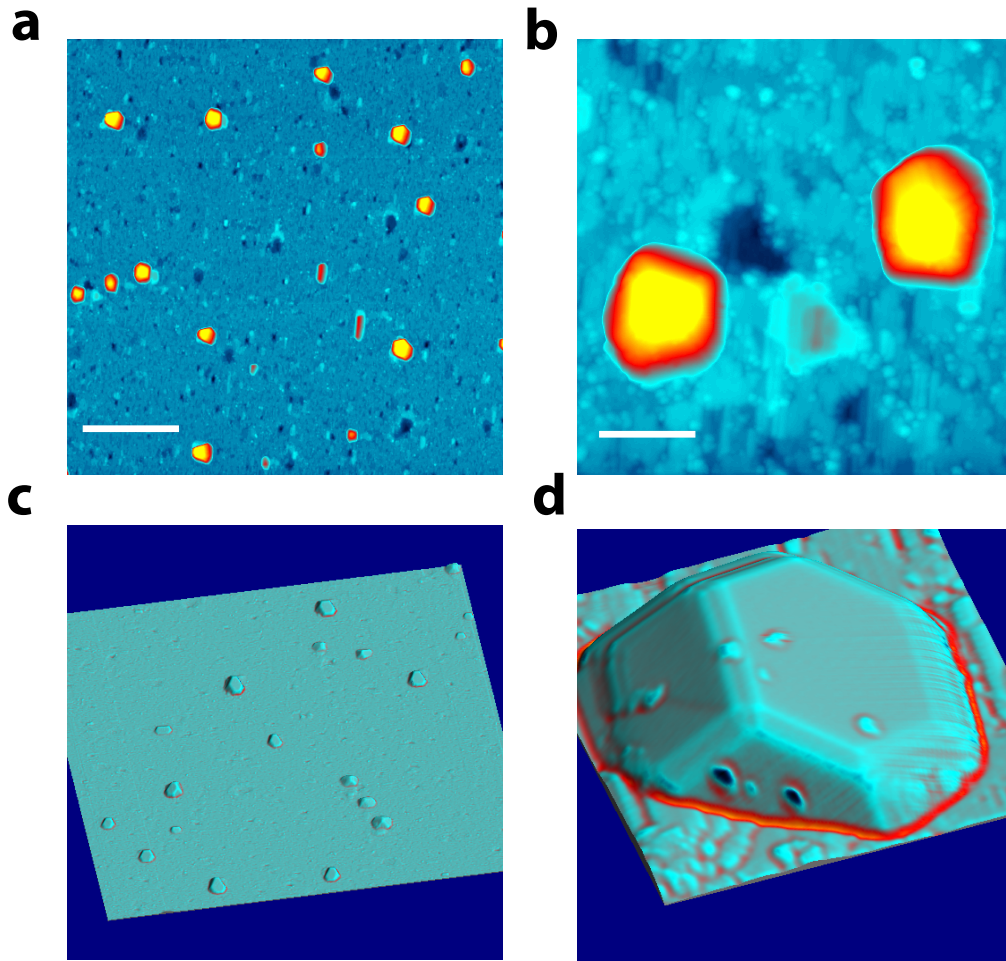


Fig. III.7 a) $800 \text{ nm} \times 800 \text{ nm}$ STM topographic image (1.5 V , 30 pA) of Bi nanocrystals grown on $\text{InAs}(110)$ surface. The scale bar is 160 nm . b) $100 \text{ nm} \times 100 \text{ nm}$ STM topographic image (0.5 V , 30 pA) of Bi nanocrystals. In the background, Bi nanowires extending along the $[110]$ direction are visible. The scale bar is 20 nm . c) 3D image of the Laplacian $\Delta_{xyz}(x, y)$ applied to the topographic image shown panel a showing that the nanocrystals are oriented along the same crystallographic axes. d) $40 \text{ nm} \times 40 \text{ nm}$ 3D image of the Laplacian $\Delta_{xyz}(x, y)$ zoomed on a single nanocrystal where the crystallographic planes are clearly visible.

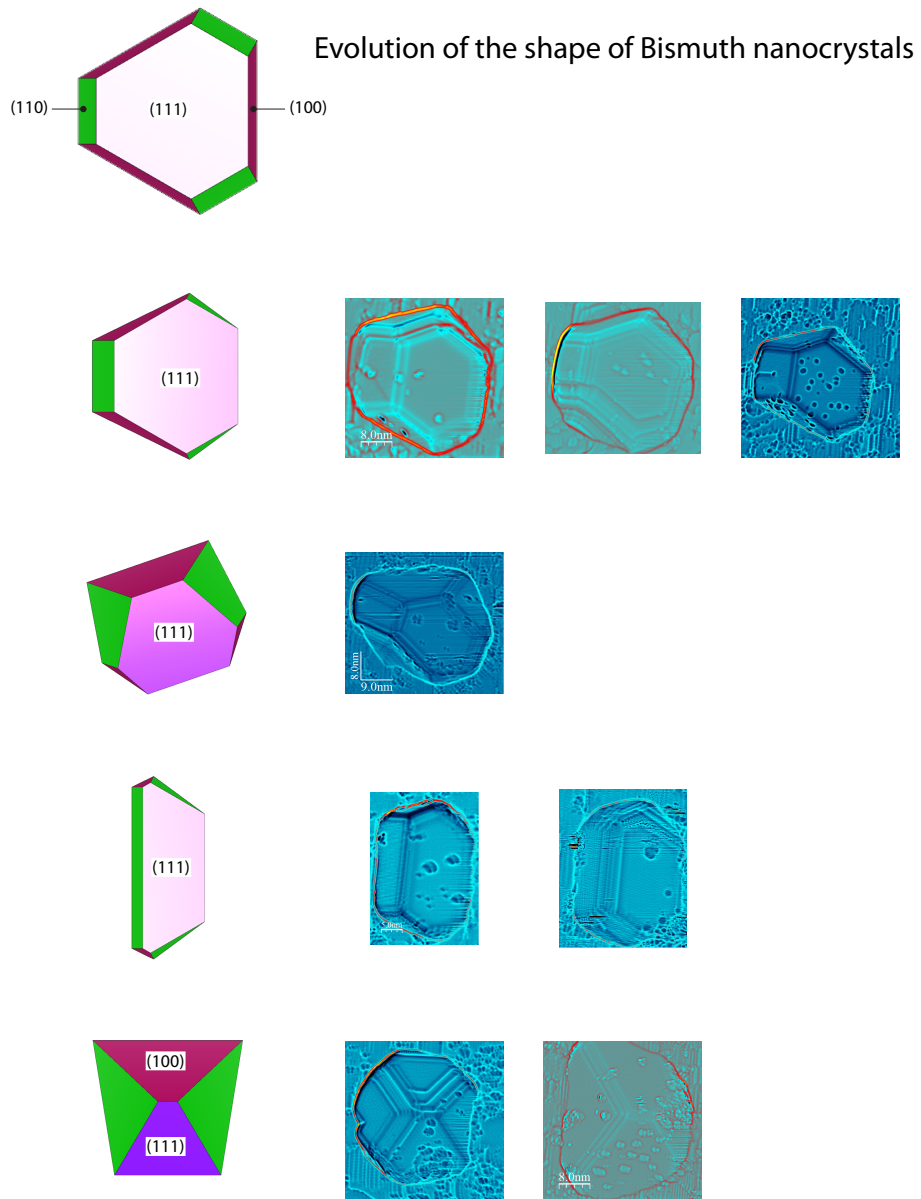


Fig. III.8 Different shapes observed for the Bi nanocrystals. (Left) Schematic of expected shapes for Bi nanocrystals with indications of the crystallographic surfaces. The (111) surface is indicated on each shape, the (100) and (110) surfaces are indicated only for the topmost shape. For the other shapes, the crystallographic orientations are recognized by the color used : red for (100) and green for (110). (right) Topographic STM images of Bi nanocrystals of different shapes.

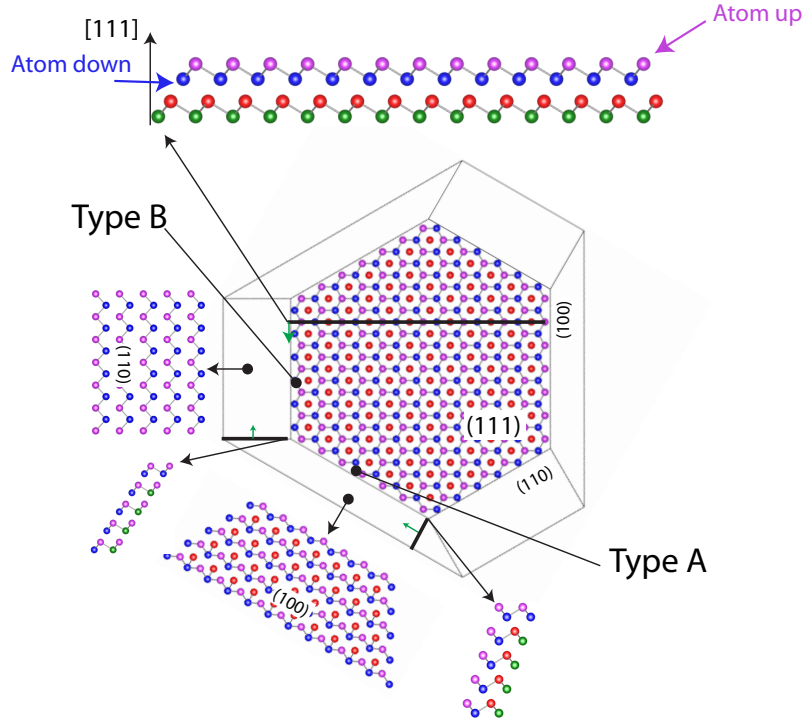


Fig. III.9 Atomic representation of a Bismuth nanocrystal where the $[111]$ direction is in-out of the page. From this sketch, one can see analyze in details the intersection between the (111) surface and the lateral surfaces (110) and (100) . The edge at the intersection between the (111) and the (100) planes is of type A, i.e. last atom pointing up. The edge at the intersection between the (111) and the (110) planes is of type B, i.e. last atom pointing down.

tial conductance spectra measured on the (111) surface of bulk Bismuth in previous works[176], as shown Fig. III.4. In particular, the differential conductance spectra present two main peaks, indicated by thick red dash lines. These two peaks are observed at voltage positions corresponding to extrema in the band dispersion of surface states where maxima in the density of states are expected. One maxima is observed at 235 meV, close to the extrema in the relation dispersion of the surface state SSI at $E_I = 204$ meV, indicated on the band diagram Fig. III.4bc, a second broad maxima is observed between -50 meV and -95 meV, close to the extrema in the relation dispersion of the surface state SSII at $E_{III} = -50$ meV, $E_{III} = -75$ meV and $E_{III} = -95$ meV, also indicated on the band diagram. For clarity, only a single thick red dash line indicates the energy E_{III} . In addition, the extrema in the relation dispersion of the surface state SSII at $E_{II} = 23$ meV is also visible as a sharp conductance edge, indicated

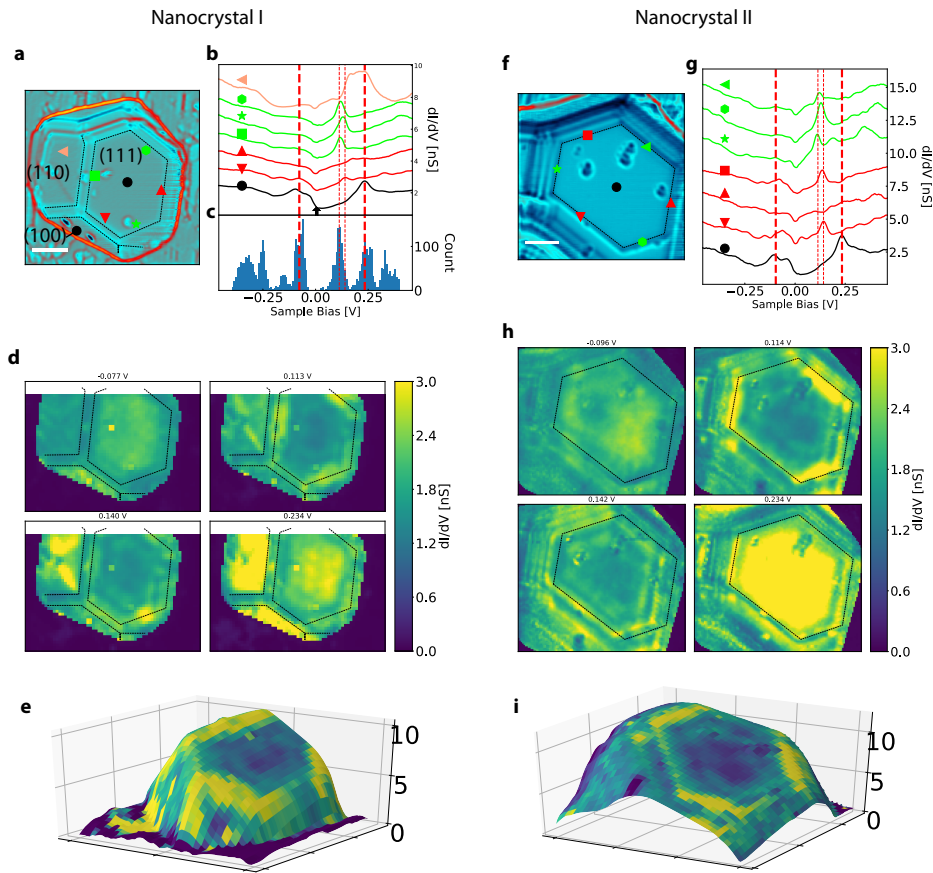


Fig. III.10 a) $40 \text{ nm} \times 40 \text{ nm}$ STM topographic image ($1.1 \text{ V}, 30 \text{ pA}$) of Bismuth nanocrystal I. Scale bar 8 nm . The six edges of the (111) facet are highlighted by black dashed lines. The symbols on this topographic image indicate the positions for which differential conductance curves are shown on panel b. b) Differential conductance curves taken at the positions indicated on panel a. c) Histogram of voltage peak positions extracted from the differential conductance spectra measured on the (111) facet. d) Differential conductance maps taken at the different voltages corresponding to the red dash lines in panel b and c. e) Differential conductance map taken at $E = 110 \text{ meV}$ projected on the 2D topographic image of the nanocrystal. f) $30 \text{ nm} \times 30 \text{ nm}$ STM topographic image ($1.5 \text{ V}, 30 \text{ pA}$) of Bismuth nanocrystal II. Scale bar 6 nm . g) Differential conductance curves taken at the positions indicated on panel f. h) Differential conductance maps taken at the different voltages corresponding to the red dash lines in panel g. i) Differential conductance map taken at $E = 110 \text{ meV}$ projected on the 2D topographic image of nanocrystal II.

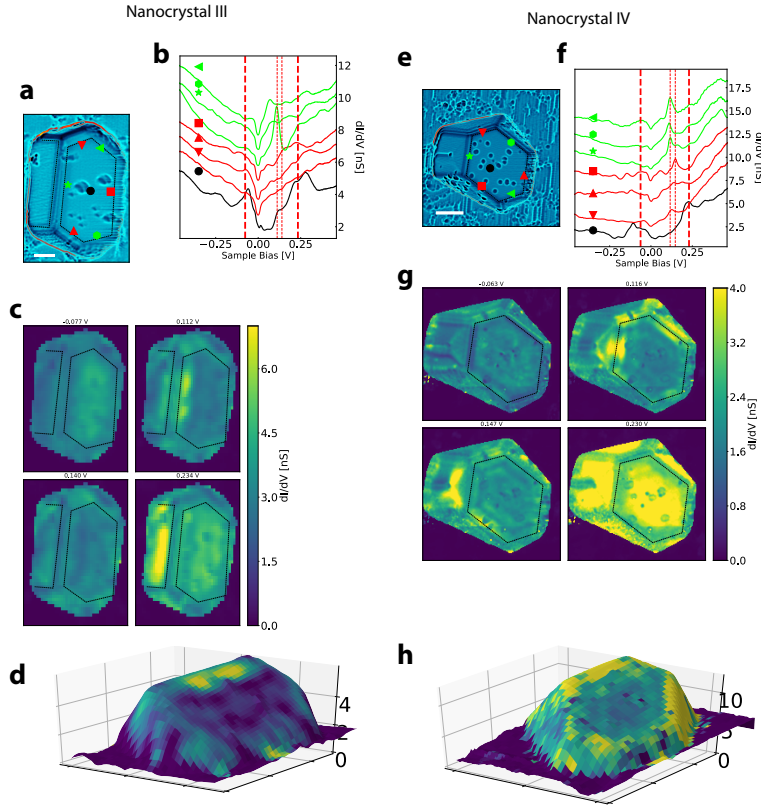


Fig. III.11 a) 25 nm × 35 nm STM topographic image (1.5 V, 30 pA) of Bismuth nanocrystal III. Scale bar 5 nm. The six edges of the (111) facet are clearly outlined by black dashed line. The symbols on this topographic image indicate the positions for which differential conductance curves are shown on panel b. b) Differential conductance curves taken at the positions indicated on panel a. c) Differential conductance maps taken at the different voltages corresponding to the red dash lines in panel b and c. d) Differential conductance map taken at $E = 110$ meV projected on the 2D topographic image of the nanocrystal. e) 50 nm × 50 nm STM topographic image (1.5 V, 30 pA) of Bismuth nanocrystal V. Scale bar 10 nm. f) Differential conductance curves taken at the positions indicated on panel e. g) Differential conductance maps taken at the different voltages corresponding to the red dash lines in panel f. h) Differential conductance map taken at $E = 110$ meV projected on the 2D topographic image of nanocrystal V.

by a black arrow. The differential conductance spectra measured on the edges, green symbol for type B, red symbols for type A, are significantly different from the spectra measured in the middle of the facet. For type B edges, a well defined single peak of large amplitude is observed at $E_B=110$ meV for all three edges. For type A edge, no prominent features are observed. Only a peak of weak amplitude at $E_A = 140$ meV is sometimes observed.

To check that the peaks observed in the spectrum shown are representative of the electronic properties of the nanocrystals and that we are not missing other peaks, we run an algorithm to find all conductance peaks in the differential conductance curves (about 2000 differential conductance curves) measured on the (111) facet of the nanocrystal. Then, we plot a histogram of the voltage positions of these conductance peaks. We show the histogram only for nanocrystal I, Fig. III.10c. This histogram displays maxima at the energy $E_{1..v}$ corresponding to extrema in the relation dispersion of the two surface states SSI and SSII. In addition, the histogram displays an additional peak located an energy about $E_B=110$ meV, corresponding to the edge-state on the edge of type B. No other peaks is observed in this voltage range, demonstrating that the edge-state is a significant characteristic of the tunneling spectrum. To check for the spatial location of the edge states, we plot four differential conductance maps taken at the different voltages corresponding to the four majors peaks observed in the spectrum. For $E=-75$ meV and $E = 235$ meV, the maps show that the electronic density of states arise from the surface states in the middle of the facets. For $E=110$ meV, the map shows clearly that the electronic density of states arise from the edge-states located on the type B edge of the (111) facet. The 3D figures where the differential conductance at $E=110$ meV are projected on the 2D topographic image of the nanocrystal shows clearly that at this energy, the electronic states are mostly localized on the type B edge of the nanocrystal. For $E = 140$ meV, the spatial location of the corresponding states does no appear so clearly.

In a recent previous work on Bismuth nanocrystals deposited on Nb[193], conductance peaks in the DC spectra were also found on both edges, at voltage positions similar to what found here. They suggested that both conductance peaks were signatures of topological edge states. While the conductance peak at $E_B=110$ meV for type B edge is found on all nanocrystals, the conductance peak at $E_A=140$ meV is not always present and seems to depend on details of the nanocrystals that we do not clearly understand. As shown by the differential conductance maps, only for type B edges, states extending along the edge can be clearly observed.

III.5 Conclusion

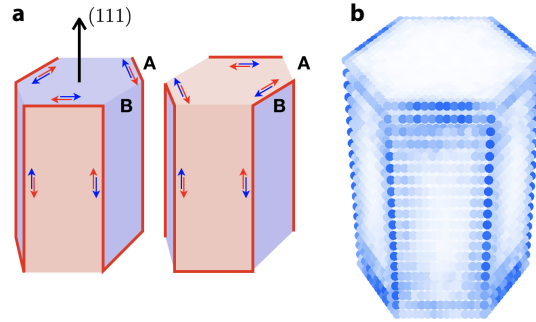


Fig. III.12 a) Schematic of the hinge states of a hexagonally-shaped Bismuth crystal. Red lines represent a single one-dimensional Kramers pair of gapless protected modes. b) Localized hinge modes of the minimal tight-binding model for Bismuth solved on a hexagon geometry. Plotted is the sum of the absolute squares of the eigenstates that lie in the bulk and surface gap.

To summarize, in our study of the tunneling spectrum of Bismuth nanocrystals, we identified edge states at the energy $E=110$ meV running along the edge of type B of the nanocrystal. Edge states were also identified previously in small cavity on the (111) surface of bulk Bi by Drozdov et al.[135]. In this last work, the edge states were also found only on one edge over two, at an energy slightly higher than us of $E=180$ meV. These authors suggested that the edge states were the signature of topological edge states as predicted by Murakami for a single bilayer of Bismuth. Because type B edges (last atom down) are more strongly coupled to the bulk Bismuth than the type A edges (last atom up), they suggested that the disappearance of one edge-state over two was the consequence of the strong coupling of the type-B edge with the bulk, inducing the disappearance of the topological state on this edge. In contrast to this last work, the major interest of our work on nanocrystals is that we can identify the type of the edge from looking at the shape of the nanocrystal. Thus, while we also found the edge-states only on one edge over two, we find that the edge-states appear only on the type B edge, a conclusion opposite to the last work. Thus, our observation cannot be reconciled with the Murakami's prediction of edge states on one bilayer of bismuth. In other words, the topmost Bismuth bilayer cannot be approximated by a single bilayer with topological edge states as predicted by Murakami. Following this conclusion, the recent theoretical work indicating that bulk Bismuth is a second order

topological insulator becomes particularly relevant. Unlike the Murakami's model that applies only to a single Bismuth bilayer, the Schindler's model applies to bulk Bismuth. This model predicts the existence of hinge-states at interface between the different crystallographic planes of Bismuth. Most remarkably, this model predicts that for (111) facets, a given hinge state should circulate only on edge over two, as sketched in Fig. III.12 extracted from Ref. [139]. Thus, this model provides a natural explanation for the spectrum observed on the Bismuth nanocrystals.

An obvious direction for future research is to study the evolution of the spectrum for the Bismuth crystal as its thickness increases, going from a two-dimensional crystal where the Murakami's model applies to the three-dimensional crystal where the Schindler's model applies.

IV – Hybrid semiconductor-superconductor Josephson junctions

In this chapter, I will present my work on Josephson junctions fabricated on bulk InAs and on InAs/GaSb heterostructures. This project has been motivated by the recent works demonstrating that the quantum well InAs/GaSb is a 2D topological insulator which becomes a topological superconductor in proximity of superconducting electrodes[8]. For this project, the system InAs/GaSb has been provided by A. Lemaître from C2N. While standard Josephson junctions have been already fabricated on this system[8], several phenomena of interest remain to be explored. In particular, it is expected theoretically that the edge-states should have a characteristic non-sinusoidal current-phase relationship. Furthermore, as shown recently in our group on Bi₂Se₃, the combination of strong spin-orbit coupling and in-plane magnetic field leads to an *anomalous* phase that can be detected through a measurement of the current-phase relationship[213]. Because this anomalous phase is strongly dependent on the Rashba coupling, measurements of the anomalous phase as function of gates voltages may provide a remarkable signature of the topological edge-states in this system InAs/GaSb, which can be gate-tuned from the trivial state to the topological state. To measure current-phase relationship requires the fabrication of asymmetric Superconducting Quantum Interference Devices (SQUIDs). In this work, we decided to develop SQUIDs based on the parallel combination of a SNS junction and a SIS junction. The "Normal" part of the SNS junction is made from InAs based semiconductor while the SIS junction is made from a standard Al/Al₂O₃/Al junction. For this project, I started in the group the development of the micro-fabrication of Josephson junctions on InAs. In the first section, I will provide a quick description of the state of art on this system. In the second section, I will describe the microfabrication method

that I developed for this project. In the third section, I will describe the preliminary results that I obtained.

IV.1 Introduction to hybrid Josephson junctions on InAs-based semiconductors

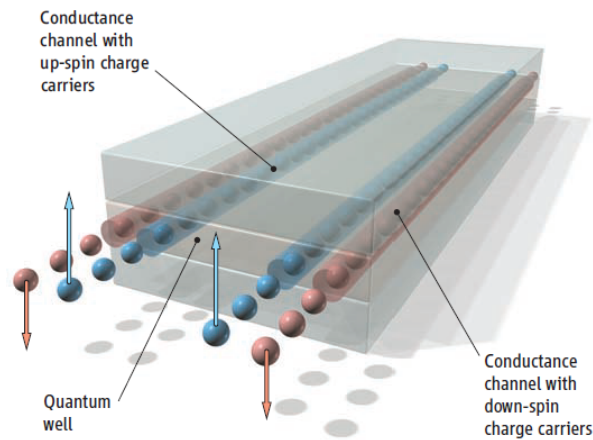


Fig. IV.1 Schematic of Quantum Spin Hall effect[214].

While field-effect transistors, where the drain-source current is modulated by a gate voltage, can be fabricated with a variety of semiconductors such as those from group IV (Si, Ge, Diamond), III-V (InAs, GaAs) or II-VI (CdSe, ZnSe), *superconducting* field-effect transistors, where the supercurrent is modulated by a gate voltage, can be fabricated only with a few semiconductors. One major difficulty in the fabrication of hybrid superconducting-semiconducting Josephson junctions is the need of a highly transparent interface between the superconducting electrodes and the semiconducting material. As discussed extensively in the first chapter, one remarkable characteristic of InAs is that the charge neutrality level is above the conduction band. This implies that the deposition of a metallic/superconducting electrode on the surface leads to the formation of an electron accumulation layer at the surface of InAs. For this reason, no Schottky barrier exists at the interface between InAs and the metallic electrode

and explains why InAs is one among few semiconductors from which the fabrication of Josephson junctions is possible. The fabrication of *superconducting transistors* started already in 1980 with the paper by T. Clarck[215]. Later, Josephson junctions have been fabricated on InAs/AlSb quantum wells[216], and in 2005, the first Josephson junction on a InAs nanowire has been fabricated[217].

Following the development of topological band theory as described in the previous chapter on Bismuth, the system InAs/GaSb attracted intense interest after the prediction of topological insulating behavior in InAs/GaSb quantum wells by Liu et al.[218]. As illustrated Fig. IV.1, the major characteristic of quantum spin Hall insulator is the existence of topological edge-states where the \uparrow and spin \downarrow propagate in opposite directions.

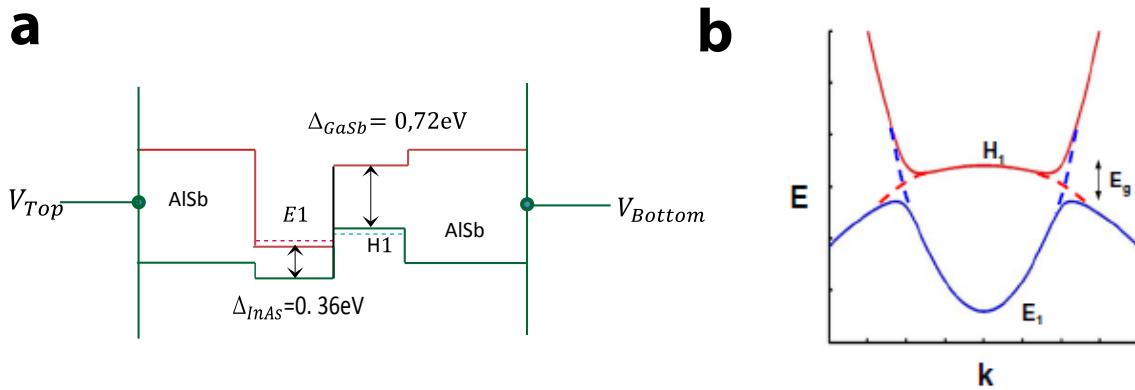


Fig. IV.2 a) *Inverted Quantum well formed by InAs/GaSb heterostructure which is sandwiched by two AlSb layers. One can see that the valence band of the AlSb layer is higher than the conduction band of the InAs layer.* b) *Band dispersion of InAs/GaSb[218].*

It is interesting to note the difference with the HgTe/CdTe topological insulator predicted by Bernevig et al.[219]. The topological nature of HgTe/CdTe arises from the band inversion between the s-like band Γ_6 and the p-like band Γ_8 within the HgTe layer. Actually, this band inversion also occurs in bulk HgTe, however, because of the doubly degenerate valence band Γ_8 , no gap exists within the bulk of HgTe and for this reason, bulk HgTe cannot qualify as a topological insulator. However, bulk HgTe can be made a bulk 3D topological insulator by applying strain to lift the degeneracy between the two valence bands[220]. In the case of HgTe/CdTe quantum wells[219], this is the quantum confinement that opens a gap and leads to the 2D topological insulator. In contrast, in InAs/GaSb quantum wells, neither InAs or GaSb have inverted band

structures. The band inversion arises from the fact that the valence band of GaSb is above the conduction band of InAs, as sketched Fig. IV.2a. Thus, in the heterostructure InAs/GaSb, this is the hybridization between the bands of InAs and GaSb that lead to band inversion and two-dimensional topological insulating behavior.

Despite this fundamental difference, the effective tight-binding Hamiltonian used to describe the band structure of InAs/GaSb[218] is very similar to the Bernevig-Hughes-Zhang Hamiltonian introduced in the previous chapter and used to describe the band structure of HgTe/CdTe quantum wells. In this previous chapter, we have also seen that this Hamiltonian is similar to the one used by Murakami to describe the topological properties of one Bismuth bi-layer.

One major advantage of InAs/GaSb heterostructures with respect to HgTe/CdTe is that the hybridization gap can be tuned with the gate voltage. In HgTe/CdTe, the band structure is set only by the thickness of the layers. In addition, InAs, GaSb and AlSb have similar lattice constant around 6.1Å [221, 222], thus, high quality heterostructures can be grown more easily than for HgTe/CdTe.

Following the theoretical prediction of topological quantum Hall insulating properties in InAs/GaSb[218], signatures of edge-states in transport properties have been reported[223, 224, 225]. Then, following the prediction that superconducting electrodes deposited on topological insulators could lead to topological superconductivity with Majorana edge-states[226, 227, 165, 228, 167, 229, 168, 230], the Delft group reported the fabrication of Josephson junctions on InAs/GaSb[8]. As shown on Fig. IV.3 extracted from this last paper, they found that the Fraunhofer pattern in the topological regime had a SQUID-like pattern, suggesting the possibility of edge-transport.

Despite these results, recent works have shown that even in the topologically-trivial regime, transport properties can be dominated by the edges[231] of the sample. It is a well established fact that etching of InAs heterostructures leads to electron accumulation on the edges as shown by numerous works aimed at the fabrication of infra-red detectors[232, 233]. For this major reason, robust way of identifying the topological properties of edges transport are searched for.

IV.2 Josephson effect

The transmission of Cooper pairs between two weakly coupled superconductors produces a superfluid current, the celebrated Josephson effect[234].

The weak link can be an insulating tunnel barrier such as in so-called Superconductor-

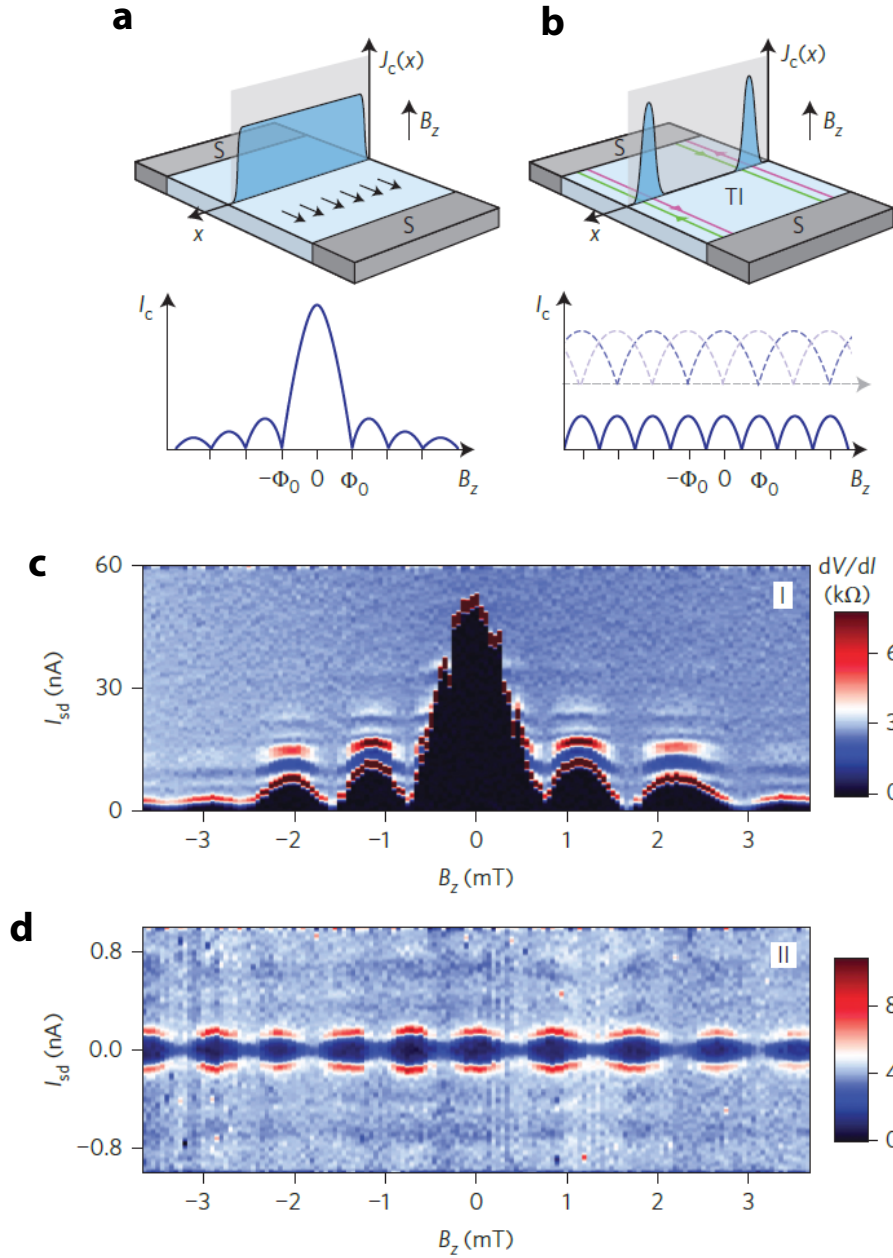


Fig. IV.3 Expected Fraunhofer interference pattern on a) non-topological and b) QSH topological insulator, respectively. $\phi_0 = \frac{h}{2e}$ is the magnetic flux quantum. c) Fraunhofer pattern measured in c) the trivial regime and d) the topological regime of an InAs/GaSb heterostructure. They are extracted from the paper by the Delft group[8].

Insulator-Superconductor (SIS) Josephson junctions or a non-superconducting layer of metal or semiconductor, which leads to so-called Superconductor-Normal-Superconductor (SNS) Josephson junctions.

As we have seen in the chapter 2, the order parameter of a superconductor is given by a complex wave-function that describes most thermodynamic and dynamic properties of the superconductor. Given two superconducting electrodes 1 & 2 described by the order parameters $\psi_1 = \sqrt{n_1}e^{i\phi_1}$ and $\psi_2 = \sqrt{n_2}e^{i\phi_2}$ with, respectively, superfluid density n_1, n_2 and phase ϕ_1, ϕ_2 , one can demonstrate the Josephson equations[81] :

$$\begin{aligned}\frac{d\phi}{dt} &= \frac{2e}{\hbar}V \\ I_c &= I_{c0} \sin(\phi)\end{aligned}$$

where $\phi = \phi_2 - \phi_1$ is the phase difference between the two electrodes.

In SIS Josephson junctions, the tunneling probability of Cooper pairs across the insulating barrier decays exponentially. For this reason, in SIS junctions, the insulating barrier is only of the order of a few nanometer thick. In contrast, in SNS junctions, the Josephson coupling results from the proximity effect from the superconductor into the normal region. Because this proximity effect extend on the distance $\xi_N = \sqrt{\frac{\hbar D}{k_B T}}$, which can be very long in high mobility gas such as InAs, SNS Josephson junctions can be made with a normal layer up to few hundreds of nanometers separating the superconducting electrodes.

To properly describe SNS Josephson junctions, one should introduce the concept of Andreev reflections and Andreev Bound States. So far, we only used the thermodynamic concept of order parameter to describe the superconducting proximity effect. The Andreev reflections provide the microscopic description for the superconducting proximity effect.

The BCS theory of superconductivity has shown that Cooper pairs result from the coupling of electron of momentum \vec{k} and spin up \uparrow with an electron of momentum $-\vec{k}$ and spin down \downarrow . In a quasi-particle description where one considers electron and hole excitations, Cooper pairing corresponds to the coupling between a quasi-electron $\psi_{k\uparrow}$ and a quasi-hole $\psi_{k\downarrow}$. On this basis, the effective BCS Hamiltonian, also called Bogolioubov-deGennes Hamiltonian, is given by :

$$H_{BdG} = \begin{pmatrix} \varepsilon_k & \Delta \\ \Delta^* & -\varepsilon_k \end{pmatrix}$$

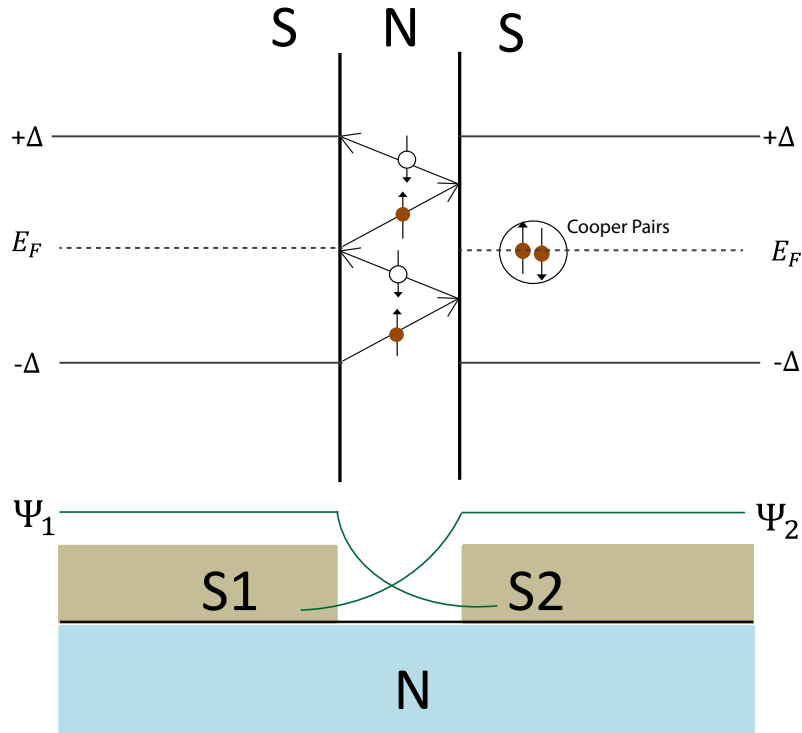


Fig. IV.4 A Josephson junction made from two superconducting electrodes $S1$ & $S2$ deposited on a normal conducting layer. Andreev Bound States in the normal region transport the superfluid current.

In a bulk superconductor, the diagonalization of this Hamiltonian provides the elementary excitation of the superconductor, the so-called Bogoliubons.

In an SN junction as sketched, Fig. IV.4, the off-diagonal pairing Δ between electrons and holes leads to Andreev reflections where an electron incoming from the normal region is retro-reflected into a hole.

Finally, in a SNS junction, Andreev Bound States are from the Bogoliubon excitations confined within the normal region between the superconducting electrodes. We can draw an analogy between normal QDots and SNS junctions. In normal QDots, the quantum confinement applied on the electron wave-function leads to the formation of discrete electronic levels. In SNS junctions, the confinement of Bogoliubon excitations within the normal region leads to the formation of Andreev Bound states.

From the knowledge of the energy spectrum $E_i(\phi)$ of the Andreev Bound States, which also depends on the phase difference between the two superconducting electrodes, the Josephson supercurrent can be calculated from the relation :

$$I = \sum_i \frac{\partial E_i(\phi)}{\partial \phi}$$

IV.3 Microfabrication of Josephson junctions with III-V semiconductors

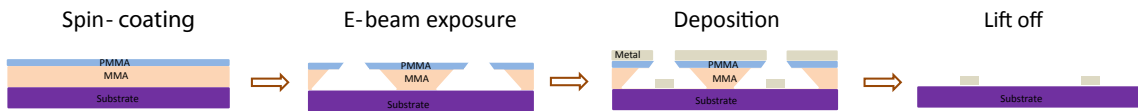


Fig. IV.5 The different steps of a lift-off with a MMA/PMMA bilayer. After spin-coating, the MMA/PMMA layer is exposed to an e-beam. Following exposure, the resist is developed, leading to a large undercut. After metal evaporation, the sample is lifted-off into acetone.

A significant time of my PhD was employed at developing the microfabrication procedure of Josephson junctions on InAs-based semiconductors.

All lithographic steps are based on e-beam exposure of MMA(8.5 EL10) and PMMA(A6) resists. To make a mask for etching purpose, a single layer of PMMA, 120 nm thick, is used and developed in MIBK/IPA 1 :3 for 75 s followed by rinsing in IPA for 30 s.

To make a mask for lift-off, a bilayer MMA/PMMA resist is employed, as sketched Fig. IV.5. Because of the large undercut in the MMA layer, the double layer resist makes the lift-off procedure much easier. The evaporation of superconducting Aluminum electrodes and gold contact and gate electrodes are done in a e-beam evaporator from Plassys. For patterning the Aluminum electrodes used for the fabrication of Josephson equations, we used a bilayer MMA(210 nm)/PMMA(70 nm), where the e-beam insulation dose is optimized by taking into account proximity effect to have the sharpest features. With this method, Josephson junctions with high aspect ratio, 5500 nm \times 400 nm, can be obtained as shown Fig. IV.6c.

The semiconducting layers have been etched with wet-etching. It has been shown in past works that wet-etching produces less damage than Reactive-Ion Etching (RIE).

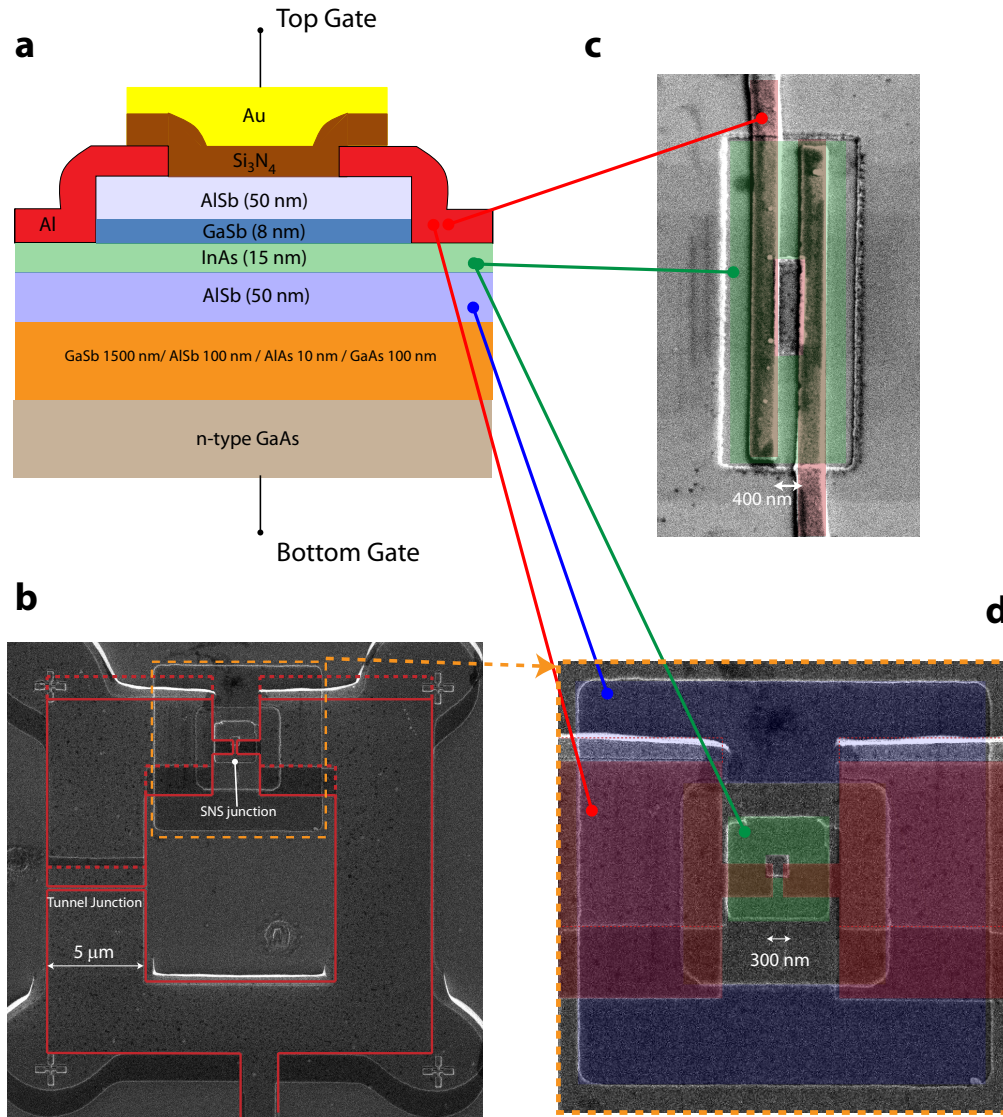


Fig. IV.6 a) Sketch of an InAs/GaSb heterostructure grown on a GaAs substrate. b) SEM image of an asymmetric SQUID made from a tunnel Josephson junction and a SNS Josephson. c) SEM image of a single Josephson junction. d) Zoom on the SNS junction of the SQUID shown panel b. On the images, the semiconducting layers and aluminum electrodes are identified by the corresponding colors used in the sketch shown panel a.

Furthermore, wet etching can be highly selective between the different layers InAs and AlSb. The wet etching is based on the following principles. Basic solutions, $\text{pH} < 7$, such as diluted TMAOH (2%) are used to etch the AlSb and GaSb layers selectively against the InAs layer. To etch the InAs layer, a solution containing hydrogen peroxide H_2O_2 and citric acid ($\text{C}_6\text{H}_8\text{O}_7$) is employed. H_2O_2 oxidize InAs, substituting As with O, and the citric acid removes the oxide. Because the AlSb layer oxidizes easily into Al_2O_3 , when this oxide needs to be removed, a diluted solution of phosphoric acid (H_3PO_4) is employed.

For gating III-V structures, a well-known procedure is to deposit a dielectric layer of Si_3N_4 by PVD. In areas where the dielectric needs to be removed, fluorine based Reactive-Ion Etching (RIE) is employed as such etchants are not etching the III-V semiconductor but only the Si_3N_4 dielectric layer.

The semiconducting layers constituting an InAs/GaSb quantum well are sketched Fig. IV.6a. For this quantum well grown by A. Lemaître of C2N, a n-doped GaAs substrate is used, which will be employed as a backgate. On this substrate, a buffer layer is grown finishing with a 50 nm thick AlSb layer. On this AlSb layer, a 15 nm thick InAs layer is grown, followed by the growth of a 8 nm thick GaSb layer that will lead to band inversion. This InAs/GaSb is protected by another 50 nm thick AlSb layer.

One of the major difficulty with the fabrication of back-gated InAs/GaSb heterostructures is to reduce the current leakage between the active InAs/GaSb layer and the doped substrate. Indeed, the AlSb layer below InAs and the buffer layer is not a good insulator. At room temperature, this buffer layer is actually highly conducting and do not allow the application of a gate voltage. Only at low temperature, below 50 K, does the AlSb layer and the buffer layer become insulating, and a gate voltage can be applied. However, this is not a really good insulating dielectric and only a few volts can be applied on the backgate. To reduce the current leakage between this backgate and the active layer, one needs to etch the top layers of AlSb/GaSb/InAs on the blue area indicated in Fig. IV.6b to isolate small mesa structures.

Step 1 : Isolation of the Mesa structure

- Spin coating of a PMMA(120 nm) layer + lithography + development
- Etching of top oxide layer with diluted phosphoric acid
- Etching of top AlSb layer with 2% TMAOH(30s) until a white mirror finish is obtained when the etching stops on the InAs layer

- Etching of the InAs layer with a solution of $C_6H_8O_7/H_2O_2/H_2O(1 :2 :4)$ until a light green finish is observed, indicating the appearance of the AlSb layer.

After the fabrication of the mesa structure, one needs to open a window in the top AlSb layer of the mesa structure, indicated by the green area in Fig. IV.6b.

Step 2 : Window opening

- Spin coating of a PMMA(120 nm) layer + lithography + development
- Etching of top oxide layer with diluted phosphoric acid
- Etching of top AlSb layer with 2% TMAOH(30s) until a white mirror finish is obtained when the etching stops on the InAs layer

After the opening of this window, a new lithographic step is employed to deposit the superconducting aluminum electrodes. After patterning and development of the resist, the sample must be pumped in a high vacuum chamber overnight to remove the residual solvent into the MMA/PMMA bi-layer. We noticed that the solvent in the resist can co-deposit during evaporation of the Aluminum electrodes and reduce the quality of the contacts. The quality of the interface is of the utmost importance to obtain good and reliable Josephson junctions. To that end, before inserting the sample into the evaporator, we dip the sample into a Na_2S solution, which removes the oxide layer at the surface of InAs and passivates the InAs with Sulphur. The passivation of the surface of III-V semiconductors with ammonium or sodium sulfide solutions is a common procedure. After this passivation step, the sample is inserted into the e-beam evaporator. Before evaporation, the sample is slightly etched with the argon ion-beam installed in the Plassys evaporator, immediately followed by the evaporation of the electrodes. The aluminum is finally protected by a 5 nm thick gold layer to protect the electrodes from the following RIE steps. For the fabrication of the SQUID which includes a SNS and a SIS junction, we use angle evaporation to fabricate the SIS junction, which involves two evaporation steps of Aluminum separated by a step of oxidation to fabricate the tunnel barrier.

Step 3 : Superconducting Aluminum electrodes

- For single junctions such as shown Fig. IV.6c, spin coating of MMA(210 nm)/PMMA(70 nm) layer + lithography + development
- For SQUIDS such as shown Fig. IV.6b, Spin coating of a MMA(380 nm)/MMA(380

- nm)/PMMA(300 nm) layer + lithography + development
- Pumping overnight on the e-beam resist to remove the solvent
- Na₂S passivation
- Mild Ion beam etching with argon in the ebeam evaporator
- For normal junctions, evaporation of the Ti(5 nm)/Al(45 nm)/Au(5 nm) electrodes
- For SQUIDS, evaporation of the first layer of Ti(5 nm)/Al(35 nm)
- For SQUIDS, oxidation, O₂ pressure 19 mbar for 240 s.
- For SQUIDS, evaporation of the second layer of Al(55 nm)+ Au(5 nm) with angle 57 °

After deposition of the aluminum electrodes, a dielectric layer of Si₃N₄, 100 nm thick, is deposited by PVD. Then opening in the dielectric layer are etched with fluorine-based RIE, so that electrical contact on the previously deposited aluminum electrodes is possible. After fluorine RIE of the Si₃N₄, an oxygen RIE has to be used to remove the polymerized resist layer on the top.

Step 4 : Dielectric deposition and RIE etching

- Spin coating of a PMMA(120 nm) layer + lithography + development
- RIE etching : SF₆ 25 sccm, power 50 watt, pressure 70 mTorr
- Oxygen RIE to remove polymerized top layer of PMMA

Finally, after etching, a final lithographic step is used to deposit the gold electrodes required to get the contacts on the superconducting aluminum electrodes and to deposit the gate electrode.

Step 5 : Contacts and gate electrodes

- Spin coating of a MMA(450 nm)/PMMA(550 nm) layer + lithography + development
- Mild Ion beam etching with argon in the e-beam evaporator
- Evaporation of the Ti(5 nm)/Au(170 nm) electrodes

IV.4 Measurements

All measurements presented are performed at a temperature about 300 mK in Helium 3 dilution refrigerator equipped with magnetic field. Four-terminals measurement is employed. To measure the IV curves, a standard method is used ; employing a Yokogawa voltage source, polarization resistance and low noise instrumentation amplifier.

To measure directly the differential conductance, a lock-in method is employed, similar to the one used in STS spectroscopy. A small AC current (10 nA) is supplied by a lock-in amplifier in addition to the direct DC current. The voltage measured across the junction is fed into the lock-in, giving the differential conductance dI/dV .

To test the quality of our evaporator and the preparation methods of the InAs, we first fabricated Josephson junctions on bulk InAs wafer where the number of microfabrication steps is reduced and so the fabrication faster.

Figure IV.7 shows a sketch and an image of the finished device. A single Josephson junction is fabricated on a bulk InAs substrate covered by dielectric layer of Si_3N_4 and a gate electrode. The dimensions of the junctions are for the length $L = 1000$ nm and for the width $W = 200$ nm.

Fig. IV.7c shows the resistance of the junction, in the normal state, its value is about $R_N = 60 \Omega$. As we cool the cryostat down to 300 mK, a sharp resistance drop is observed at the critical superconducting transition temperature $T_c = 0.8$ K. The critical temperature is smaller than the bulk $T_c = 1.2$ K of Aluminum. This is due to the inverse proximity effect from the sticking layer of Ti.

In Fig. IV.8 (left), current-voltage characteristics measured at $T = 300$ mK is displayed as function of in-plane magnetic field. The curve displays a clear Josephson current at zero bias, with a critical current about $1 \mu\text{A}$ at zero magnetic field. The IV curve has the characteristic shape observed in SNS junctions. In Fig. IV.8 (right), the critical current I_c is extracted and plot as function of magnetic field. In a short junction model[81], where the junction is smaller than ξ_N , the Ambegaokar-Baratoff relation[235] provides a relation between the amplitude of the critical current, the normal state resistance and the superconducting gap energy :

$$I_c R_N = \frac{\pi \Delta}{2e} \tanh(\Delta/2k_B T)$$

From the measured critical current, normal resistance and sample temperature, we can extract the effective superconducting gap energy $\Delta = 51 \mu\text{eV}$. From the BCS formula, Eq. II.3, one can also calculate the superconducting gap energy from the mea-

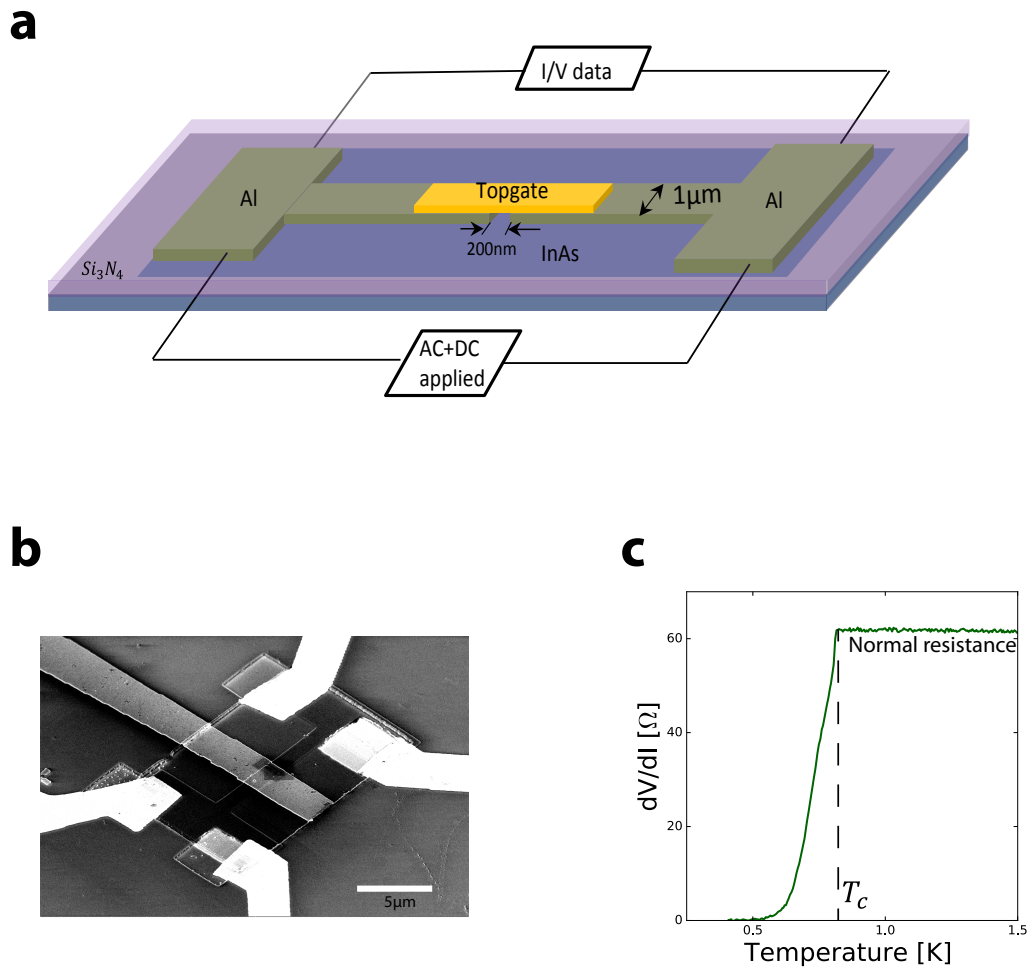


Fig. IV.7 a) Sketch of a junction fabricated on bulk InAs. b) SEM image of device. c) Resistance dependence on temperature.

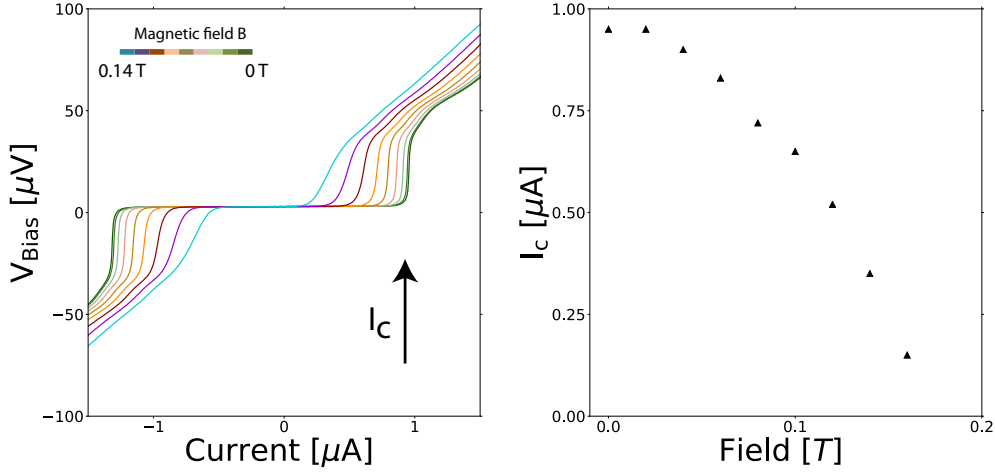


Fig. IV.8 Left : $I - V$ characteristics of a single Josephson junction on InAs as function of in-plane magnetic field. Right : The critical current extracted from IV characteristics is plotted as function of the amplitude of in-plane magnetic field.

sured critical temperature $T_c = 0.8$ K. From bulk aluminum, we know the BCS ratio $2\Delta/k_B T_c = (340\mu\text{eV})/(1.2\text{ K}) = 3.3$. Using this BCS ratio, and using the measured $T_c = 0.8$ K, we get the superconducting gap $\Delta = 110\ \mu\text{eV}$. This is about two times larger than extracted from the value of the critical current. This implies that the critical current is two times smaller than expected theoretically. This kind of discrepancy is not unusual with SNS junctions. We are satisfied through that the measured critical current has the correct order of magnitude.

We see now that the critical current I_c can be tuned by the gate voltage as shown in Fig. IV.9. Gate voltages from 0 to -26 V are applied to the junction. At 0 gate voltage, the critical current $I_c \approx 1\ \mu\text{A}$. At the maximum negative voltage -26 V, limited by the breakdown of the dielectric layer Si_3N_4 , I_c decreases down to $0.3\ \mu\text{A}$. This is due to the depletion of electron density in the n doped InAs.

To test the quality of the junction, we applied microwave radiations. As shown in Fig. IV.10, current steps appear in the $I - V$ characteristic as an expected consequence of the AC Josephson effect. Indeed, when irradiating a Josephson junction with a microwave signal, its phase oscillates with the frequency f of the applied signal. Standard junctions with a conventional 2π periodic current-phase relationship, $I_J = I_c \sin(\varphi)$, will display superfluid current steps, i.e. the Shapiro steps, at the voltage values[236]. :

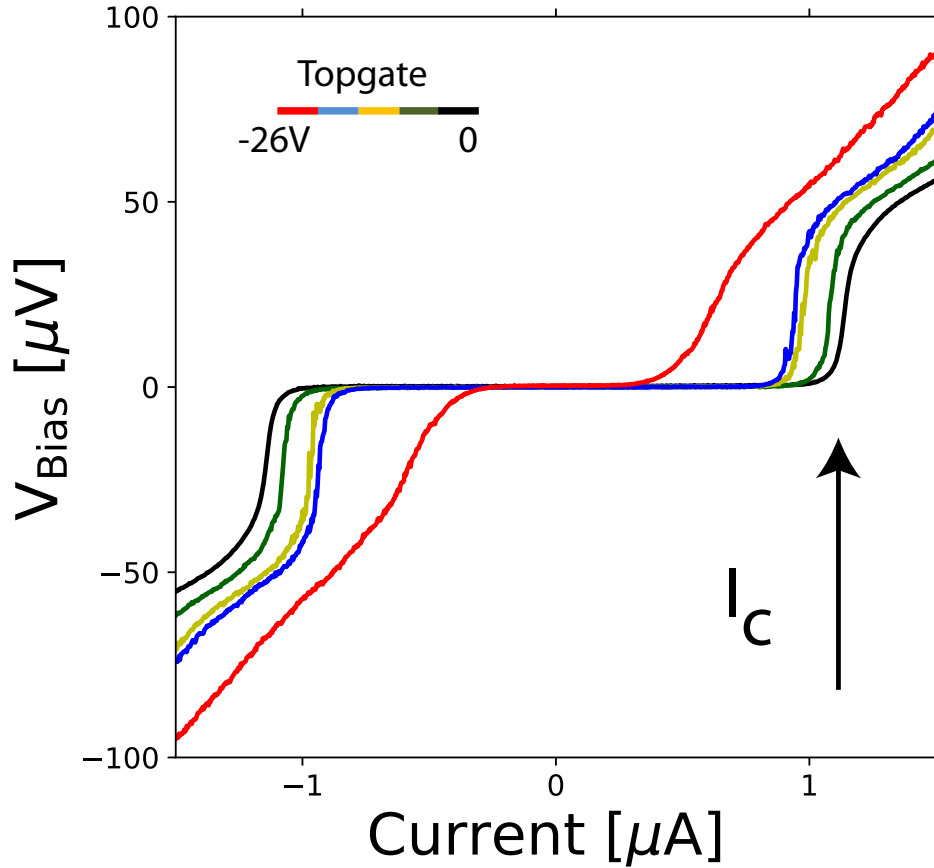


Fig. IV.9 $I - V$ characteristics as function of top-gate voltage.

$$V = nf \frac{\hbar\pi}{e}$$

where $n = 0, 1, 2, \dots$

From this last formula, the expected voltage difference between two Shapiro steps is about $11 \mu\text{V}$ for an irradiation frequency $f = 5 \text{ GHz}$, as observed experimentally in Fig. IV.10. The observation of the Shapiro steps testify the quality of the junction.

Finally, we measured the difference resistance dI/dV of this junction. We find local maxima that certainly result from multiple Andreev reflections in the junction.

When a voltage bias exists between the two superconducting electrodes, quasi-particle transfer from one electrode is generally not possible because no quasi-particle states exists within the superconducting gap. Only for a voltage bias of $V > 2\Delta/e$,

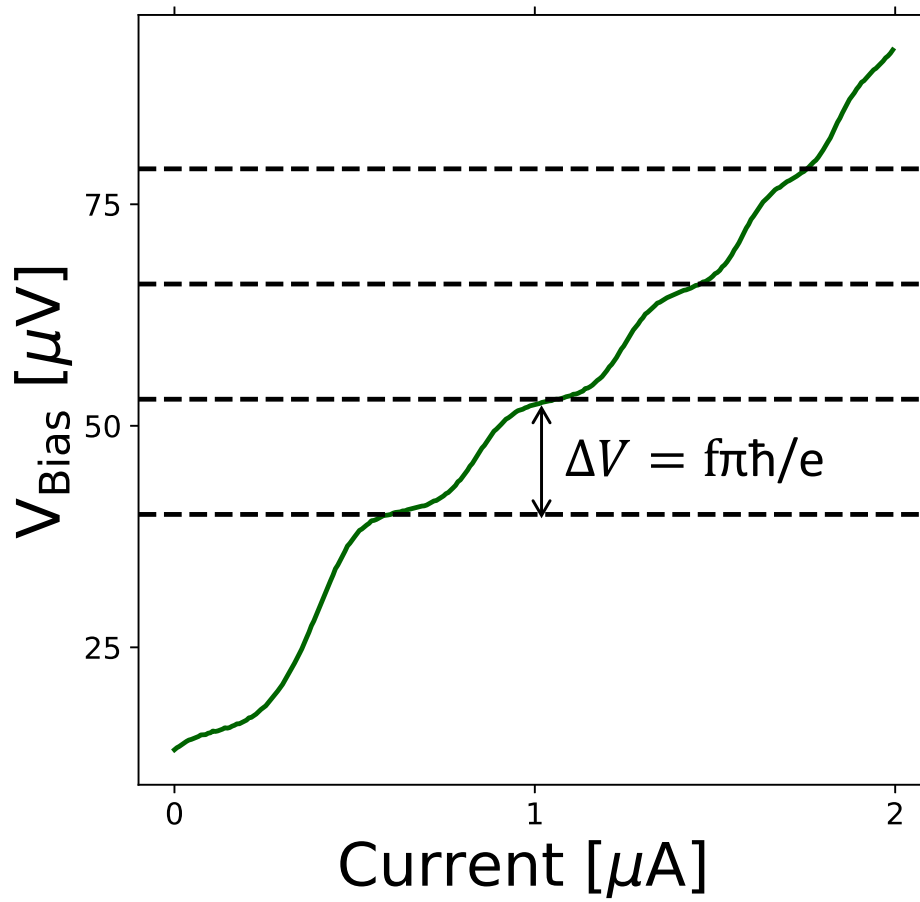


Fig. IV.10 $I - V$ characteristic of a junction submitted to a microwave signal of $f = 5 \text{ GHz}$. Shapiro steps can be observed.

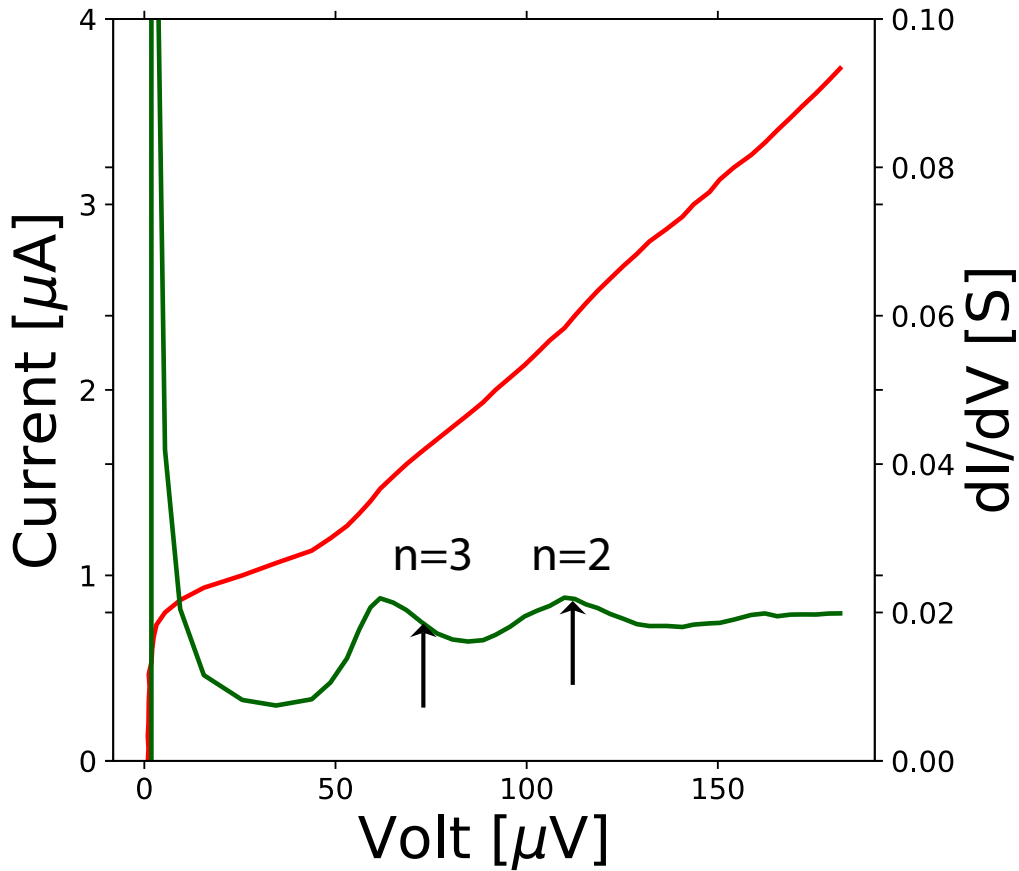


Fig. IV.11 IV (green line) and dI/dV (red line) characteristic as function of bias voltage for a single SNS junction. The vertical arrows indicate the position of the peaks expected for the Andreev reflections of order $n = 2$ and $n = 3$.

direct transfer of quasi-particles from one electrode to the other is possible. However, quasi-particle transfer for lower voltage $V < 2\Delta/e$ is possible thanks to multiple Andreev reflections. Indeed, let's consider a quasi-electron injected from one superconducting electrode into the normal region, if the voltage bias $V < 2\Delta/e$, this quasi-electron will be reflected back into quasi-hole with an addition energy given by eV . If the quasi-hole has an energy higher than the gap energy, it will get into the electrode. However, if its energy is lower than the gap energy, it will be reflected back into a quasi-electron, acquiring again an energy eV . Multiple Andreev reflections occur until the energy of the quasi-particle is high enough above the superconducting gap to get into the electrode. Thus, because of the peak in density of states at the gap edge, maxima in the conductance are observed when :

$$V = \frac{2\Delta}{ne}$$

where n is the order of the reflection. An Andreev reflection of order n corresponds to n traversals of the normal region in the SNS junction. From the superconducting gap energy $\Delta = 110 \mu\text{eV}$ in our junction, we expect maxima in the conductance at the values $[220, 110, 73, 55] \mu\text{eV}$ for $n=[1,2,3,4]$ respectively. On the differential conductance curve shown Fig. IV.11, we can identify the two peaks resulting from multiple Andreev reflection of order $n = 2$ and $n = 3$. Note that the the position of the peak $n = 3$ does not match exactly the position of the peak observed experimentally.

IV.5 Conclusion

The ultimate goal of this project that I have started in the group is the fabrication of asymmetric SQUIDs composed of one standard SIS, Aluminum/Aluminum oxide/Aluminum junction, and one SNS junction fabricated on the edge of an InAs/GaSb mesa. This asymmetric SQUID will first be employed to measure the current-phase relationship of the edge states. Furthermore, with an in-plane magnetic field, we will test for the generation of an anomalous phase shift. I completed the development of the microfabrication methods and I have been able to finish chip-circuits with standard Josephson junctions and asymmetric SQUIDs.

The observation of good Josephson characteristics, including the Shapiro steps and multiple Andreev reflections, on the single Josephson junctions testified that our preparation method of the InAs surface is reliable and enable the fabrication of Josephson junctions.

First measurements of the asymmetric SQUIDs in a dilution fridge are planed in a near future.

V – Conclusion and Perspectives

In the first experiment, we have seen that it is possible to grow high quality Pb nanocrystals on the (110) surface of InAs. We found that, because of the large Fermi wavelength, larger than the lateral width of the nanocrystal, the nanocrystal is only weakly coupled to the substrate, which leads to the emergence of Coulomb blockade in this nanocrystal. Thanks to this phenomena, we have been able to study, for the first time by STM, the superconducting parity effect, which we employed to test the validity of the Anderson limit. Furthermore, on this same system, we have been able to observe discrete electronic levels and attempted the mapping of the corresponding wavefunctions.

In the second experiment, we have seen that Bi nanocrystals can also be grown on the top of InAs. However, because of the presence of wetting layer of Bi at the interface between InAs and the nanocrystal, the electronic coupling between the Bi nanocrystals and the substrate is strong, which suppress Coulomb blockade. In this experiment, we obtained spectroscopic maps on the (111) face of the nanocrystals on which we identify edge-states. These edge-states can be naturally interpreted as the hinge-states expected for second-order 3D topological insulators where the edge-states are uni-dimensional.

Finally, during this PhD, I developed, in the group, the microfabrication methods for fabricating Josephson junctions and asymmetric SQUIDs with InAs substrates and InAs/GaSb heterostructures. Preliminary results indicate that our method for surface preparation of InAs is reliable and leads to good Josephson characteristics.

In the introduction of this manuscript, I started with a discussion of the recent development on the design of topological materials with trivial III-V semiconductors and superconductors. We have seen that a topological insulator can be fabricated from the heterostructure InAs/GaSb and that topological superconductors can be fabricated from the superconducting proximity effect induced in a nanowire[6] with an in-axial magnetic field or from the proximity effect into the topological insulator InAs/GaSb[8].

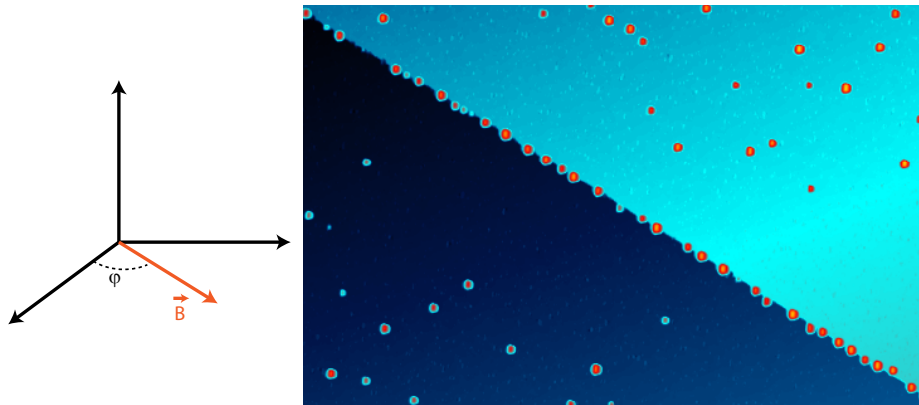


Fig. V.1 A row of Pb nanocrystals aligned against an atomic step edge of the substrate. In a STM equipped with a vectorial magnetic field, it could be possible to test the emergence of Majorana states for a magnetic field aligned along the row of Pb nanocrystals.

While my STM results on superconducting Pb nanocrystals do not seem to have a direct relationship with those results, further work under magnetic field may be of interest for topological superconductivity. Indeed, as shown in Fig. V.1, Pb nanocrystals tend to accumulate on the step edges of the InAs nanowire. By improving the growth procedure, it seems quite possible to grow a nanowire along this step edge through the fusion of the Pb nanocrystals. Using an STM equipped with a vectorial magnetic field, it should be possible to apply the magnetic along the axial direction of the nanowire, or equivalently step-edge, and study the tunneling spectrum near the end of the nanowire. This system seems to provide a possible realization of a topological superconductor through the superconducting proximity effect induced in a semiconducting nanowire, as suggested theoretically by Lutchyn et al.[6] and observed experimentally in InAs[237, 238, 239, 240] and InSb nanowires[6, 241, 242].

On the Bi nanocrystals, we identified topological edge-states. It would be interesting to observe extended step-edges. To do so, it could also be interesting to attempt the growth of Bi nanowires along step edges of III-V semiconductors.

Finally, for the InAs/GaSb heterostructure, one of the motivations for developing the microfabrication methods on this system in the group is to study the topological edge-states on the side of this heterostructure through STM spectroscopy. Indeed, several works, in particular by our collaborators of C2N, have shown that it was possible to perform tunneling spectroscopy on the edges of cleaved heterostructures[13, 10].

VI – Publications

1. **Tianzhen Zhang**, Sergio Vlaic, Stéphane Pons, Alexandre Assouline, Alexandre Zimmers, Dimitri Roditchev, Hervé Aubin, et al. “Quantum Confinement Effects in Pb Nanocrystals Grown on InAs.” [Physical Review B 97\(21\) : 214514\(2018\)](#) (Editor’s suggestion)
2. **Tianzhen Zhang**, et al. “STM spectroscopy study of topological hinge states on Bismuth nanocrystal.” [in preparation](#)
3. Sergio Vlaic, Stéphane Pons, **Tianzhen Zhang**, Alexandre Assouline, Alexandre Zimmers, Christophe David, Guillemin Rodary, Jean-Christophe Girard, Dimitri Roditchev, and Hervé Aubin. “Superconducting Parity Effect across the Anderson Limit.” [Nature Communications 8 \(2\) : 14549\(2017\)](#)
4. Alexandre Assouline, Cheryl Feuillet-Palma, Nicolas Bergeal, **Tianzhen Zhang**, Alireza Mottaghizadeh, Alexandre Zimmers, Emmanuel Lhuillier, et al. “Spin-Orbit Induced Phase-Shift in Bi_2Se_3 Josephson Junctions.” [arXiv Preprint arXiv :1806. 01406. https ://arxiv.org/abs/1806.01406\(2018\)](#).

Bibliographie

- [1] C. LIU, T. HUGHES, X.-L. QI, K. WANG & S.-C. ZHANG ; «Quantum Spin Hall Effect in Inverted Type-II Semiconductors» ; Phys. Rev. Lett. **100**, p. 236 601 (2008). [v](#), [66](#)
- [2] I. KNEZ, R.-R. DU & G. SULLIVAN ; «Evidence for Helical Edge Modes in Inverted InAs/GaSb Quantum Wells» ; Phys. Rev. Lett. **107**, p. 136 603 (2011). [v](#), [67](#)
- [3] L. DU, I. KNEZ, G. SULLIVAN & R. R. DU ; «Robust helical edge transport in gated InAs/GaSb bilayers» ; Phys. Rev. Lett. **114**, p. 1–5 (2015). [v](#), [67](#)
- [4] F. QU, A. J. A. BEUKMAN, S. NADJ-PERGE, M. WIMMER, B.-M. NGUYEN, W. YI, J. THORP, M. SOKOLICH, A. A. KISELEV, M. J. MANFRA, C. M. MARCUS & L. P. KOUWENHOVEN ; «Electric and Magnetic Tuning Between the Trivial and Topological Phases in InAs/GaSb Double Quantum Wells» ; Phys. Rev. Lett. **115**, p. 036 803 (2015). [v](#), [67](#)
- [5] F. COUËDO, H. IRIE, K. SUZUKI, K. ONOMITSU & K. MURAKI ; «Single-edge transport in an InAs/GaSb quantum spin Hall insulator» ; Phys. Rev. B Condens. Matter **94**, p. 035 301 (2016). [v](#), [67](#)
- [6] J. D. SAU, R. M. LUTCHYN, S. TEWARI & S. DAS SARMA ; «Generic New Platform for Topological Quantum Computation Using Semiconductor Heterostructures» ; Phys. Rev. Lett. **104**, p. 040 502 (2010). [v](#), [105](#), [106](#)
- [7] V. MOURIK, K. ZUO, S. M. FROLOV, S. R. PLISSARD, E. P. a. M. BAKKERS & L. P. KOUWENHOVEN ; «Signatures of Majorana Fermions in Hybrid Superconductor-Semiconductor Nanowire Devices» ; Science **336**, p. 1003–1007 (2012). [v](#)
- [8] V. S. PRIBIAG, A. J. BEUKMAN, F. QU, M. C. CASSIDY, C. CHARPENTIER, W. WEGSCHEIDER & L. P. KOUWENHOVEN ; «Edge-mode superconductivity

- in a two-dimensional topological insulator» ; Nature nanotechnology **10**, p. 593 (2015). [v](#), [85](#), [88](#), [89](#), [105](#)
- [9] P. N. FIRST, J. a. STROSCIO, R. a. DRAGOSET, D. T. PIERCE & R. J. CELOTTA ; «Metallicity and gap states in tunneling to Fe clusters in GaAs(110)» ; Phys. Rev. Lett. **63**, p. 1416–1419 (1989). [v](#)
- [10] J. C. GIRARD, A. LEMAÎTRE, A. MIARD, C. DAVID & Z. Z. WANG ; «Low temperature scanning tunneling microscopy wave-function imaging of InAsGaAs cleaved quantum dots with similar height» ; J. Vac. Sci. Technol. B Microelectron. Nanometer Struct. Process. Meas. Phenom. **27**, p. 891–894 (2009). [v](#), [106](#)
- [11] A. URBIETA, B. GRANDIDIER, J. P. NYS, D. DERESMES, D. STIÉVENARD, A. LEMAÎTRE, G. PATRIARCHE & Y. M. NIQUET ; «Scanning tunneling spectroscopy of cleaved InAs/GaAs quantum dots at low temperatures» ; Phys. Rev. B Condens. Matter **77**, p. 155 313 (2008). [v](#)
- [12] B. GRANDIDIER, Y. M. NIQUET, B. LEGRAND, J. P. NYS, C. PRIESTER, D. STIEVENARD, J. M. GERARD & V. THIERRY-MIEG, V ; «Imaging the wave-function amplitudes in cleaved semiconductor quantum boxes» ; Phys. Rev. Lett. **85**, p. 1068–1071 (2000). [v](#)
- [13] B. FAIN, I. ROBERT-PHILIP, A. BEVERATOS, C. DAVID, Z. Z. WANG, I. SAGNES & J. C. GIRARD ; «Discretization of Electronic States in Large InAsP / InP Multilevel Quantum Dots Probed by Scanning Tunneling Spectroscopy» ; Phys. Rev. Lett. **108**, p. 126 808 (2012). [v](#), [106](#)
- [14] J. BARDEEN ; «Tunnelling from a many-particle point of view» ; Physical Review Letters **6**, p. 57 (1961). [3](#)
- [15] J. G. SIMMONS ; «Generalized formula for the electric tunnel effect between similar electrodes separated by a thin insulating film» ; Journal of applied physics **34**, p. 1793–1803 (1963). [3](#)
- [16] R. LANDAUER ; «Electrical resistance of disordered one-dimensional lattices» ; Philosophical magazine **21**, p. 863–867 (1970). [3](#)
- [17] M. BÜTTIKER, Y. IMRY, R. LANDAUER & S. PINHAS ; «Generalized many-channel conductance formula with application to small rings» ; Physical Review B **31**, p. 6207 (1985). [3](#)
- [18] G. BINNIG, H. ROHRER, C. GERBER & E. WEIBEL ; «Tunneling through a controllable vacuum gap» ; Applied Physics Letters **40**, p. 178–180 (1982). [5](#)

- [19] G. BINNIG, H. ROHRER, C. GERBER & E. WEIBEL ; «Surface studies by scanning tunneling microscopy» ; Physical review letters **49**, p. 57 (1982). 5
- [20] G. BINNIG & H. ROHRER ; «Scanning tunneling microscope» ; (1982) ; uS Patent 4,343,993. 5
- [21] G. KLIMECK, R. C. BOWEN, T. B. BOYKIN & T. A. CWIK ; «sp^{3s}* Tight-binding parameters for transport simulations in compound semiconductors» ; Superlattices and Microstructures **27**, p. 519–524 (2000). 7
- [22] W. MÖNCH ; *Electronic properties of semiconductor interfaces* ; tome 123 (Springer Science & Business Media) (2003). 8, 9
- [23] T. ZHANG, S. VLAIC, S. PONS, A. ASSOULINE, A. ZIMMERS, D. RODITCHEV, H. AUBIN, G. ALLAN, C. DELERUE, C. DAVID *et al.* ; «Quantum confinement effects in Pb nanocrystals grown on InAs» ; Physical Review B **97**, p. 214514 (2018). 8
- [24] W. MÖNCH ; *Semiconductor surfaces And Interfaces* (Springer Berlin Heidelberg) (2001). 9, 11
- [25] W. MONCH ; «On the physics of metal-semiconductor interfaces» ; Rep. Prog. Phys. **53**, p. 221–278 (1990). 9, 10
- [26] S. G. LOUIE & M. L. COHEN ; «Electronic structure of a metal-semiconductor interface» ; Phys. Rev. B Condens. Matter **13**, p. 2461–2469 (1976). 9
- [27] J. P. LAFEMINA ; «Total-energy calculations of semiconductor surface reconstructions» ; Surf. Sci. Rep. **16**, p. 137–260 (1992). 9
- [28] W. G. SCHMIDT ; «Adsorption of group-V elements on III–V (1 1 0) surfaces» ; Surf. Sci. Rep. **25**, p. 141–223 (1996). 9
- [29] J. TERSOFF ; «Schottky Barrier Heights and the Continuum of Gap States» ; Phys. Rev. Lett. **52**, p. 465–468 (1984). 9
- [30] J. TERSOFF ; «Theory of semiconductor heterojunctions : The role of quantum dipoles» ; Phys. Rev. B : Condens. Matter Mater. Phys. **30**, p. 4874–4877 (1984). 9
- [31] M. MORGENSTERN, A. GEORGI, C. STRASSER, C. R. AST, S. BECKER & M. LIEBMANN ; «Scanning tunneling microscopy of two-dimensional semiconductors : Spin properties and disorder» ; Physica E **44**, p. 1795–1814 (2012). 9, 15

- [32] H.-U. BAIER, L. KOENDERS & W. MÖNCH; «Oxidation of InAs (110) and correlated changes of electronic surface properties»; *J. Vac. Sci. Technol. B Microelectron. Nanometer Struct. Process. Meas. Phenom.* **4**, p. 1095–1099 (1986). 10
- [33] Y. CHEN, J. C. HERMANSON & G. J. LAPEYRE; «Coupled plasmon and phonon in the accumulation layer of InAs(110) cleaved surfaces»; *Phys. Rev. B Condens. Matter* **39**, p. 12 682–12 687 (1989). 10
- [34] K. SMIT, L. KOENDERS & W. MÖNCH; «Adsorption of chlorine and oxygen on cleaved InAs (110) surfaces : Raman spectroscopy, photoemission spectroscopy, and Kelvin probe measurements»; *J. Vac. Sci. Technol. B Microelectron. Nanometer Struct. Process. Meas. Phenom.* **7**, p. 888–893 (1989). 10
- [35] V. Y. ARISTOV, I. L. BOLOTIN & S. G. GELAKHOVA; «Anomalous pinning of the Fermi level at the InAs (110)-Cu interface obtained at 10 K»; *Surf. Sci.* **251**, p. 453–456 (1991). 10
- [36] T. VAN GEMMEREN, S. R. SALMAGNE & W. MÖNCH; «Atomic nitrogen on InAs (110) surfaces at room temperature»; *Appl. Surf. Sci.* **65**, p. 625–631 (1993). 10
- [37] V. Y. ARISTOV, G. LE LAY, L. T. VINH, K. HRICOVINI & J. E. BONNET; «Giant band bending induced by Ag on InAs(110) surfaces at low temperature»; *Phys. Rev. B : Condens. Matter Mater. Phys.* **47**, p. 2138–2145 (1993). 10
- [38] V. Y. ARISTOV, G. L. LAY, P. SOUKIASSIAN, K. HRICOVINI, J. E. BONNET, J. OSVALD & O. OLSSON; «Alkali-Metal-Induced Highest Fermi-Level Pinning Position above Semiconductor Conduction Band Minimum»; *Europhys. Lett.* **26**, p. 359–364 (1994). 10
- [39] V. Y. ARISTOV, G. LE LAY, P. SOUKIASSIAN, K. HRICOVINI, J. E. BONNET, J. OSVALD & O. OLSSON; «Cs-induced highest EF jump above InAs (110) conduction-band minimum»; *J. Vac. Sci. Technol. B Microelectron. Nanometer Struct. Process. Meas. Phenom.* **12**, p. 2709–2712 (1994). 10
- [40] V. Y. ARISTOV, P. S. MANGAT, P. SOUKIASSIAN & G. LE LAY; «NaInAs (110) interface formation at RT»; *Surf. Sci.* **331**, p. 641–645 (1995). 10
- [41] C. NOWAK, J. KRUIJATZ, A. MÄRKL, C. MEYNE, A. CHASSÉ, W. BRAUN, W. RICHTER & D. ZAHN; «The adsorption of Sb on InAs (110) studied by photoemission and photoelectron diffraction»; *Surf. Sci.* **331**, p. 619–624 (1995). 10

- [42] M. MORGENSTERN, M. GETZLAFF, D. HAUDE, R. WIESENDANGER & R. L. JOHNSON; «Coverage dependence of the Fe-induced Fermi-level shift and the two-dimensional electron gas on InAs(110)»; Phys. Rev. B Condens. Matter **61**, p. 13 805–13 812 (2000). [10](#)
- [43] M. GETZLAFF, M. MORGENSTERN, C. MEYER, R. BROCHIER, R. JOHNSON & R. WIESENDANGER; «Nb-induced two-dimensional electron gas on n-InAs(110) : Anomalous coverage dependence»; Phys. Rev. B : Condens. Matter Mater. Phys. **63**, p. 205 305 (2001). [10](#), [11](#)
- [44] M. MORGENSTERN, J. WIEBE, A. WACHOWIAK, M. GETZLAFF, J. KLIJN, L. PLUCINSKI, R. L. JOHNSON & R. WIESENDANGER; «Co on p -InAs(110) : An island-induced two-dimensional electron system consisting of electron droplets»; Phys. Rev. B : Condens. Matter Mater. Phys. **65**, p. 155 325 (2002). [10](#)
- [45] J. M. LAYET, M. CARRÈRE, H. J. KIM, R. L. JOHNSON, R. BELKHOUB, V. ZHILIN, V. Y. ARISTOV & G. LE LAY; «Two-dimensional electron gas at InAs(100)1×2/1×4 Pb»; Surf. Sci. **402-404**, p. 724–728 (1998). [10](#)
- [46] L. Ö. OLSSON, C. B. M. ANDERSSON, M. C. HÅKANSSON, J. KANSKI, L. ILVER & U. O. KARLSSON; «Charge Accumulation at InAs Surfaces»; Phys. Rev. Lett. **76**, p. 3626–3629 (1996). [10](#)
- [47] L. PIPER, T. VEAL, M. LOWE & C. MCCONVILLE; «Electron depletion at InAs free surfaces : Doping-induced acceptorlike gap states»; Phys. Rev. B : Condens. Matter Mater. Phys. **73**, p. 195 321 (2006). [10](#)
- [48] G. BINNIG, N. GARCIA, H. ROHRER, J. SOLER & F. FLORES; «Electron-metal-surface interaction potential with vacuum tunneling : Observation of the image force»; Physical Review B **30**, p. 4816 (1984). [12](#)
- [49] R. M. FEENSTRA, Y. DONG, M. SEMTSIV & W. MASSELINK; «Influence of tip-induced band bending on tunnelling spectra of semiconductor surfaces»; Nanotechnology **18**, p. 044 015 (2006). [12](#)
- [50] G. DE RAAD, D. BRULS, P. KOENRAAD & J. WOLTER; «Interplay between tip-induced band bending and voltage-dependent surface corrugation on GaAs (110) surfaces»; Physical Review B **66**, p. 195 306 (2002). [12](#)
- [51] S. LOTH; *Atomic scale images of acceptors in III-V semiconductors : band bending, tunneling paths and wave functions* (Universitätsverlag Göttingen) (2008). [12](#)

- [52] R. DOMBROWSKI, C. STEINEBACH, C. WITTNEVEN, M. MORGENSTERN & R. WIESENDANGER ; «Tip-induced band bending by scanning tunneling spectroscopy of the states of the tip-induced quantum dot on InAs(110)» ; Phys. Rev. B : Condens. Matter Mater. Phys. **59**, p. 8043–8048 (1999). 15
- [53] P. W. ANDERSON ; «Theory of dirty superconductors» ; Journal of Physics and Chemistry of Solids **11**, p. 26–30 (1959). 17
- [54] H. BRUNE ; «Microscopic view of epitaxial metal growth : nucleation and aggregation» ; (1998). 18, 27
- [55] C. GORTER ; «A possible explanation of the increase of the electrical resistance of thin metal films at low temperatures and small field strengths» ; Physica **17**, p. 777–780 (1951). 19
- [56] W. HALPERIN ; «Quantum size effects in metal particles» ; Reviews of Modern Physics **58**, p. 533 (1986). 20
- [57] K. PEDERSEN ; «Quantum size effects in nanostructures» ; Organic and Inorganic Nanostructures (2006). 20
- [58] D. L. KLEIN, R. ROTH, A. K. L. LIM, A. PAUL ALIVISATOS & P. L. MC EUEN ; «A single-electron transistor made from a cadmium selenide nanocrystal» ; Nature **323**, p. 699 (1997). 20, 21
- [59] U. BANIN, Y. CAO, D. KATZ & O. MILLO ; «Identification of atomic-like electronic states in indium arsenide nanocrystal quantum dots» ; Nature **400**, p. 542–544 (1999). 20, 21
- [60] O. MILLO, D. KATZ, Y. CAO & U. BANIN ; «Scanning tunneling spectroscopy of InAs nanocrystal quantum dots» ; Phys. Rev. B : Condens. Matter Mater. Phys. **61**, p. 16 773–16 777 (2000). 20, 21
- [61] O. MILLO, D. KATZ, Y. CAO & U. BANIN ; «Imaging and Spectroscopy of Artificial-Atom States in Core/Shell Nanocrystal Quantum Dots» ; Phys. Rev. Lett. **86**, p. 5751–5754 (2001). 20, 21, 57
- [62] P. LILJEROTH, P. A. Z. VAN EMMICHOVEN, S. G. HICKEY, H. WELLER, B. GRANDIDIER, G. ALLAN & D. VANMAEKELBERGH ; «Density of states measured by scanning-tunneling spectroscopy sheds new light on the optical transitions in PbSe nanocrystals» ; Phys. Rev. Lett. **95**, p. 086 801 (2005). 20, 21
- [63] P. LILJEROTH, K. OVERGAAG, A. URBIETA, B. GRANDIDIER, S. HICKEY & D. VANMAEKELBERGH ; «Variable Orbital Coupling in a Two-Dimensional

- Quantum-Dot Solid Probed on a Local Scale»; *Phys. Rev. Lett.* **97**, p. 1–4 (2006). [20](#), [21](#)
- [64] P. LILJEROTH, L. JDIRA, K. OVERGAAG, B. GRANDIDIER, S. SPELLER & D. VANMAEKELBERGH; «Can scanning tunnelling spectroscopy measure the density of states of semiconductor quantum dots?»; *Phys. Chem. Chem. Phys.* **8**, p. 3845 (2006). [20](#), [21](#)
- [65] L. JDIRA, P. LILJEROTH, E. STOFFELS, D. VANMAEKELBERGH & S. SPELLER; «Size-dependent single-particle energy levels and interparticle Coulomb interactions in CdSe quantum dots measured by scanning tunneling spectroscopy»; *Phys. Rev. B : Condens. Matter Mater. Phys.* **73**, p. 1–6 (2006). [20](#), [21](#)
- [66] Z. SUN, I. SWART, C. DELERUE, D. VANMAEKELBERGH & P. LILJEROTH; «Orbital and Charge Resolved Polaron States in CdSe Dots and Rods Probed by Scanning Tunneling Spectroscopy»; *Phys. Rev. Lett.* **102**, p. 196 401 (2009). [20](#), [21](#)
- [67] H. WANG, E. LHUILLIER, Q. YU, A. MOTTAGHIZADEH, C. ULYSSE, A. ZIMMERS, A. DESCAMPS-MANDINE, B. DUBERTRET & H. AUBIN; «Effects of electron-phonon interactions on the electron tunneling spectrum of PbS quantum dots»; *Phys. Rev. B : Condens. Matter Mater. Phys.* **92**, p. 041 403 (2015). [20](#), [21](#)
- [68] H. WANG, E. LHUILLIER, Q. YU, A. ZIMMERS, B. DUBERTRET, C. ULYSSE & H. AUBIN; «Transport in a Single Self-Doped Nanocrystal»; *ACS Nano* **11**, p. 1222–1229 (2017). [20](#), [21](#)
- [69] A. M. CHANG, H. U. BARANGER, L. N. PFEIFFER, K. W. WEST & T. Y. CHANG; «Non-Gaussian distribution of Coulomb blockade peak heights in quantum dots»; *Phys. Rev. Lett.* **76**, p. 1695–1698 (1996). [20](#), [21](#)
- [70] J. A. FOLK, S. R. PATEL, S. F. GODIJN, A. G. HUIBERS, S. M. CRONENWETT, C. M. MARCUS, K. CAMPMAN & A. C. GOSSARD; «Statistics and parametric correlations of Coulomb blockade peak fluctuations in quantum dots»; *Phys. Rev. Lett.* **76**, p. 1699–1702 (1996). [20](#), [21](#)
- [71] S. M. CRONENWETT, S. R. PATEL, C. M. MARCUS, K. CAMPMAN & A. C. GOSSARD; «Mesoscopic Fluctuations of Elastic Cotunneling in Coulomb Blockaded Quantum Dots»; *Phys. Rev. Lett.* **79**, p. 2312–2315 (1997). [20](#), [21](#)
- [72] S. R. PATEL, S. M. CRONENWETT, D. R. STEWART, A. G. HUIBERS, C. M. MARCUS, C. I. DURUÖZ, J. S. HARRIS, K. CAMPMAN & A. C. GOSSARD;

- «Statistics of Coulomb Blockade Peak Spacings»; Phys. Rev. Lett. **80**, p. 4522–4525 (1998). [20](#), [21](#)
- [73] A. G. HUIBERS, S. R. PATEL, C. M. MARCUS, P. W. BROUWER, C. I. DURUÖZ & J. S. HARRIS; «Distributions of the Conductance and its Parametric Derivatives in Quantum Dots»; Phys. Rev. Lett. **81**, p. 1917–1920 (1998). [20](#), [21](#)
- [74] S. R. PATEL, D. R. STEWART, C. M. MARCUS, M. GÖKÇEDAĞ, Y. ALHASSID, A. D. STONE, C. I. DURUÖZ & J. S. HARRIS; «Changing the Electronic Spectrum of a Quantum Dot by Adding Electrons»; Phys. Rev. Lett. **81**, p. 5900–5903 (1998). [20](#), [21](#)
- [75] O. BOHIGAS, M. J. GIANNONI & C. SCHMIT; «Characterization of Chaotic Quantum Spectra and Universality of Level Fluctuation Laws»; (1984). [21](#)
- [76] F. HAAKE; *Quantum Signatures of Chaos* (Springer Science & Business Media) (2001). [21](#)
- [77] Y. ALHASSID; «The statistical theory of quantum dots»; Rev. Mod. Phys. **72**, p. 895–968 (2000). [21](#), [57](#)
- [78] A. MIRLIN; «Statistics of energy levels and eigenfunctions in disordered systems»; Phys. Rep. **326**, p. 259–382 (2000). [21](#), [57](#)
- [79] R. A. JALABERT, A. D. STONE & Y. ALHASSID; «Statistical theory of Coulomb blockade oscillations : Quantum chaos in quantum dots»; Physical review letters **68**, p. 3468 (1992). [21](#)
- [80] A. ASSOULINE, C. FEUILLET-PALMA, A. ZIMMERS, H. AUBIN, M. APRILI & J.-C. HARMAND; «Shiba Bound States across the Mobility Edge in Doped InAs Nanowires»; Phys. Rev. Lett. **119**, p. 097 701 (2017). [21](#)
- [81] M. TINKHAM; *Introduction to superconductivity - 2nd ed* (New York : McGraw Hill) (1996). [23](#), [90](#), [97](#)
- [82] D. DEAN & M. HJORTH-JENSEN; «Pairing in nuclear systems : from neutron stars to finite nuclei»; Reviews of Modern Physics **75**, p. 607 (2003). [24](#)
- [83] G. ZÜRN, A. WENZ, S. MURMANN, A. BERGSCHNEIDER, T. LOMPE & S. JOCHIM; «Pairing in few-fermion systems with attractive interactions»; Physical review letters **111**, p. 175 302 (2013). [24](#)
- [84] J. DUKELSKY, S. PITTEL & G. SIERRA; «Colloquium : Exactly solvable Richardson-Gaudin models for many-body quantum systems»; Reviews of modern physics **76**, p. 643 (2004). [24](#)

- [85] D. AVERIN & Y. V. NAZAROV ; «Single-electron charging of a superconducting island» ; Physical review letters **69**, p. 1993 (1992). [24](#), [43](#), [46](#)
- [86] P. LAFARGE, P. JOYEZ, D. ESTEVE, C. URBINA & M. DEVORET ; «Two-electron quantization of the charge on a superconductor» ; Nature **365**, p. 422 (1993). [24](#)
- [87] M. TUOMINEN, J. HERGENROTHER, T. TIGHE & M. TINKHAM ; «Experimental evidence for parity-based 2e periodicity in a superconducting single-electron tunneling transistor» ; Physical review letters **69**, p. 1997 (1992). [24](#)
- [88] M. TUOMINEN, J. HERGENROTHER, T. TIGHE & M. TINKHAM ; «Even-odd electron number effects in a small superconducting island : Magnetic-field dependence» ; Physical Review B **47**, p. 11 599 (1993). [24](#)
- [89] T. M. EILES, J. M. MARTINIS & M. H. DEVORET ; «Even-odd asymmetry of a superconductor revealed by the Coulomb blockade of Andreev reflection» ; Physical review letters **70**, p. 1862 (1993). [24](#)
- [90] P. LAFARGE, P. JOYEZ, D. ESTEVE, C. URBINA & M. DEVORET ; «Measurement of the even-odd free-energy difference of an isolated superconductor» ; Physical review letters **70**, p. 994 (1993). [24](#)
- [91] A. P. HIGGINBOTHAM, S. M. ALBRECHT, G. KIRŠANSKAS, W. CHANG, F. KUEMMETH, P. KROGSTRUP, T. S. JESPERSEN, J. NYGÅRD, K. FLENSBERG & C. M. MARCUS ; «Parity lifetime of bound states in a proximitized semiconductor nanowire» ; Nature Physics **11**, p. 1017 (2015). [24](#)
- [92] P. JOYEZ, P. LAFARGE, A. FILIPE, D. ESTEVE & M. DEVORET ; «Observation of parity-induced suppression of Josephson tunneling in the superconducting single electron transistor» ; Physical review letters **72**, p. 2458 (1994). [24](#)
- [93] J. AUMENTADO, M. W. KELLER, J. M. MARTINIS & M. H. DEVORET ; «Nonequilibrium quasiparticles and 2 e periodicity in single-cooper-pair transistors» ; Physical review letters **92**, p. 066 802 (2004). [24](#)
- [94] D. J. VAN WOERKOM, A. GERESDI & L. P. KOUWENHOVEN ; «One minute parity lifetime of a NbTiN Cooper-pair transistor» ; Nature Physics **11**, p. 547 (2015). [24](#), [25](#)
- [95] A. SAVIN, M. MESCHKE, J. P. PEKOLA, Y. A. PASHKIN, T. LI, H. IM & J.-S. TSAI ; «Parity effect in Al and Nb single electron transistors in a tunable environment» ; Applied Physics Letters **91**, p. 063 512 (2007). [25](#)

- [96] C. BLACK, D. RALPH & M. TINKHAM; «Spectroscopy of the superconducting gap in individual nanometer-scale aluminum particles»; Physical review letters **76**, p. 688 (1996). 25
- [97] J. VON DELFT & D. C. RALPH; «Spectroscopy of discrete energy levels in ultrasmall metallic grains»; Physics Reports **345**, p. 61–173 (2001). 25
- [98] D. RALPH, C. BLACK & M. TINKHAM; «Spectroscopic measurements of discrete electronic states in single metal particles»; Physical review letters **74**, p. 3241 (1995). 25
- [99] D. RALPH, C. BLACK & M. TINKHAM; «Gate-voltage studies of discrete electronic states in aluminum nanoparticles»; Physical review letters **78**, p. 4087 (1997). 25
- [100] F. BRAUN & J. VON DELFT; «Fixed-n superconductivity : The crossover from the bulk to the few-electron limit»; Physical review letters **81**, p. 4712 (1998). 25
- [101] J. DUKELSKY & G. SIERRA; «Crossover from bulk to few-electron limit in ultrasmall metallic grains»; Physical Review B **61**, p. 12 302 (2000). 25
- [102] A. MASTELLONE, G. FALCI & R. FAZIO; «Small superconducting grain in the canonical ensemble»; Physical review letters **80**, p. 4542 (1998). 25
- [103] S. BOSE, A. M. GARCÍA-GARCÍA, M. M. UGEDA, J. D. URBINA, C. H. MICHAELIS, I. BRIHUEGA & K. KERN; «Observation of shell effects in superconducting nanoparticles of Sn»; Nature materials **9**, p. 550 (2010). 26, 27
- [104] C. BRUN, K. H. MÜLLER, I.-P. HONG, F. PATTHEY, C. FLINDT & W.-D. SCHNEIDER; «Dynamical coulomb blockade observed in nanosized electrical contacts»; Physical review letters **108**, p. 126 802 (2012). 27
- [105] D. BOLMONT, P. CHEN, F. PROIX & C. A. SEBENNE; «Room-temperature formation of the Ag/GaAs (110) interface»; J. Phys. C : Solid State Phys. **15**, p. 3639 (1982). 27
- [106] R. LUDEKE, T.-C. CHIANG & T. MILLER; «Schottky barrier formation of Ag on GaAs (110)»; J. Vac. Sci. Technol. B Microelectron. Nanometer Struct. Process. Meas. Phenom. **1**, p. 581–587 (1983). 27
- [107] B. M. TRAFAS, Y. N. YANG, R. L. SIEFERT & J. H. WEAVER; «Scanning tunneling microscopy of Ag growth on GaAs(110) at 300 K : From clusters to crystallites»; Phys. Rev. B : Condens. Matter Mater. Phys. **43**, p. 14 107–14 114 (1991). 27

- [108] G. NEUHOLD, L. BARTELS, J. J. PAGGEL & K. HORN; «Thickness-dependent morphologies of thin Ag films on GaAs(110) as revealed by LEED and STM»; (1997). 27
- [109] R. M. FEENSTRA; «Electronic states of metal atoms on the GaAs(110) surface studied by scanning tunneling microscopy»; Phys. Rev. Lett. **63**, p. 1412–1415 (1989). 27
- [110] P. N. FIRST, J. a. STROSCIO, R. a. DRAGOSSET, D. T. PIERCE & R. J. CELOTTA; «Metallicity and gap states in tunneling to Fe clusters in GaAs(110)»; Phys. Rev. Lett. **63**, p. 1416–1419 (1989). 29
- [111] J. WIEBE, C. MEYER, J. KLIJN, M. MORGENSTERN & R. WIESENDANGER; «From quantized states to percolation : Scanning tunneling spectroscopy of a strongly disordered two-dimensional electron system»; Phys. Rev. B : Condens. Matter Mater. Phys. **68**, p. 041 402 (2003). 29, 41
- [112] D. a. MUZYCHENKO, K. SCHOUTEDEN, S. V. SAVINOV, N. S. MASLOVA, V. I. PANOV & C. VAN HAESENDONCK; «Low-Temperature Scanning Tunneling Microscopy of Ring-Like Surface Electronic Structures Around Co Islands on InAs(110) Surfaces»; J. Nanosci. Nanotechnol. **9**, p. 4700–4708 (2009). 29, 41
- [113] K. MCGREER, J.-C. WAN, N. ANAND & A. GOLDMAN; «Superconducting energy gap in Coulomb staircase tunneling structures»; Physical Review B **39**, p. 12 260 (1989). 35
- [114] A. HANNA & M. TINKHAM; «Variation of the Coulomb staircase in a two-junction system by fractional electron charge»; Physical review B **44**, p. 5919 (1991). 35, 36, 37
- [115] A. HANNA, M. TUOMINEN & M. TINKHAM; «Observation of elastic macroscopic quantum tunneling of the charge variable»; Physical review letters **68**, p. 3228 (1992). 35
- [116] E. BAR-SADEH & O. MILLO; «Observation of an interplay between single-electron charging effects and superconductivity in YNi₂B₂C»; Physical Review B **53**, p. 3482 (1996). 35
- [117] I.-P. HONG, C. BRUN, M. PIVETTA, F. PATTHEY & W.-D. SCHNEIDER; «Coulomb blockade phenomena observed in supported metallic nanoislands»; Frontiers in Physics **1**, p. 1–8 (2013). 35

- [118] A. E. HANNA & M. TINKHAM; «Variation of the Coulomb staircase in a two-junction system by fractional electron charge»; Phys. Rev. B : Condens. Matter Mater. Phys. **44**, p. 5919–5922 (1991). 36
- [119] W. MÖNCH; *Semiconductor surfaces and interfaces*; tome 26 (Springer Science & Business Media) (2013). 39, 41
- [120] M. MORGENSTERN, A. GEORGI, C. STRASSER, C. AST, S. BECKER & M. LIEB-MANN; «Scanning tunneling microscopy of two-dimensional semiconductors : Spin properties and disorder»; Physica E : Low-dimensional Systems and Nanostructures **44**, p. 1795–1814 (2012). 39, 41
- [121] J. W. G. WILDÖER, A. J. A. VAN ROIJ, C. J. P. M. HARMANS & H. VAN KEMPEN; «Semiconductor band switching by charging a small grain with a single electron»; Phys. Rev. B : Condens. Matter Mater. Phys. **53**, p. 10 695–10 698 (1996). 41
- [122] B. J. VAN WEES, H. VAN HOUTEN, C. W. J. BEENAKKER, J. G. WILLIAMSON, L. P. KOUWENHOVEN, D. VAN DER MAREL & C. T. FOXON; «Quantized conductance of point contacts in a two-dimensional electron gas»; Phys. Rev. Lett. **60**, p. 848–850 (1988). 41
- [123] C. PASQUIER, U. MEIRAV, F. I. B. WILLIAMS, D. C. GLATTLI, Y. JIN & B. ETIENNE; «Quantum limitation on Coulomb blockade observed in a 2D electron system»; Phys. Rev. Lett. **70**, p. 69–72 (1993). 41
- [124] L. P. KOUWENHOVEN, D. AUSTING & S. TARUCHA; «Few-electron quantum dots»; Reports on Progress in Physics **64**, p. 701 (2001). 43
- [125] A. FLORIS, A. SANNA, S. MASSIDDA & E. GROSS; «Two-band superconductivity in Pb from ab initio calculations»; Physical Review B **75**, p. 054 508 (2007). 51
- [126] M. RUBY, B. W. HEINRICH, J. I. PASCUAL & K. J. FRANKE; «Experimental demonstration of a two-band superconducting state for lead using scanning tunneling spectroscopy»; Physical review letters **114**, p. 157 001 (2015). 51
- [127] Y.-F. ZHANG, J.-F. JIA, T.-Z. HAN, Z. TANG, Q.-T. SHEN, Y. GUO, Z. Q. QIU & Q.-K. XUE; «Band Structure and Oscillatory Electron-Phonon Coupling of Pb Thin Films Determined by Atomic-Layer-Resolved Quantum-Well States»; Phys. Rev. Lett. **95**, p. 096 802 (2005). 52
- [128] I. B. ALTFEDER, K. A. MATVEEV & D. M. CHEN; «Electron Fringes on a Quantum Wedge»; Phys. Rev. Lett. **78**, p. 2815–2818 (1997). 52

- [129] W. B. SU, S. H. CHANG, W. B. JIAN, C. S. CHANG, L. J. CHEN & T. T. TSONG ; «Correlation between Quantized Electronic States and Oscillatory Thickness Relaxations of 2D Pb Islands on Si(111)-(7×7) Surfaces» ; Phys. Rev. Lett. **86**, p. 5116–5119 (2001). 52
- [130] P. M. ECHENIQUE & J. B. PENDRY ; «The existence and detection of Rydberg states at surfaces» ; J. Phys. C : Solid State Phys. **11**, p. 2065–2075 (1978). 52
- [131] B. PANNETIER & H. COURTOIS ; «Andreev reflection and proximity effect» ; Journal of low temperature physics **118**, p. 599–615 (2000). 58, 61
- [132] K. D. USADEL ; «Generalized diffusion equation for superconducting alloys» ; Physical Review Letters **25**, p. 507 (1970). 61
- [133] S. GUÉRON, H. POTHIER, N. O. BIRGE, D. ESTEVE & M. DEVORET ; «Superconducting proximity effect probed on a mesoscopic length scale» ; Physical review letters **77**, p. 3025 (1996). 61
- [134] W. BELZIG, C. BRUDER & G. SCHÖN ; «Local density of states in a dirty normal metal connected to a superconductor» ; Physical Review B **54**, p. 9443 (1996). 61
- [135] I. K. DROZDOV, A. ALEXANDRADINATA, S. JEON, S. NADJ-PERGE, H. JI, R. J. CAVA, B. BERNEVIG & A. YAZDANI ; «One-dimensional topological edge states of bismuth bilayers» ; Nat. Phys. (2014). 65, 66, 73, 74, 83
- [136] S. MURAKAMI ; «Quantum spin Hall effect and enhanced magnetic response by spin-orbit coupling» ; Phys. Rev. Lett. **97**, p. 236 805 (2006). 65, 66, 73
- [137] M. WADA, S. MURAKAMI, F. FREIMUTH & G. BIHLMAYER ; «Localized edge states in two-dimensional topological insulators : Ultrathin Bi films» ; Phys. Rev. B : Condens. Matter Mater. Phys. **83**, p. 121 310 (2011). 65, 73
- [138] F. SCHINDLER, A. M. COOK, M. G. VERGNIORY, Z. WANG, S. S. P. PARKIN, B. ANDREI BERNEVIG & T. NEUPERT ; «Higher-order topological insulators» ; Science Advances **4**, p. eaat0346 (2018). 66, 74, 75
- [139] F. SCHINDLER, Z. WANG, M. G. VERGNIORY, A. M. COOK, A. MURANI, S. SENGUPTA, A. Y. KASUMOV, R. DEBLOCK, S. JEON, I. DROZDOV *et al.* ; «Higher-Order Topology in Bismuth» ; arXiv preprint arXiv :1802.02585 (2018). 66, 75, 84
- [140] D. J. THOULESS, M. KOHMOTO, M. P. NIGHTINGALE & M. DEN NIJS ; «Quantized Hall Conductance in a Two-Dimensional Periodic Potential» ; Phys. Rev. Lett. **49**, p. 405–408 (1982). 66

- [141] F. D. HALDANE; «Model for a quantum Hall effect without Landau levels : Condensed-matter realization of the “parity anomaly”»; Phys. Rev. Lett. **61**, p. 2015–2018 (1988). 66
- [142] C. L. KANE & E. J. MELE; «Z2 topological order and the quantum spin hall effect»; Phys. Rev. Lett. **95**, p. 3–6 (2005). 66
- [143] J. E. MOORE & L. BALENTS; «Topological invariants of time-reversal-invariant band structures»; Phys. Rev. B Condens. Matter **75**, p. 121 306 (2007). 66
- [144] B. A. BERNEVIG, T. L. HUGHES & S.-C. ZHANG; «Quantum spin Hall effect and topological phase transition in HgTe quantum wells»; Science **314**, p. 1757–1761 (2006). 66
- [145] M. KÖNIG, S. WIEDMANN, C. BRÜNE, A. ROTH, H. BUHMANN, L. W. MOLENKAMP, X.-L. QI & S.-C. ZHANG; «Quantum spin hall insulator state in HgTe quantum wells»; Science **318**, p. 766–770 (2007). 66
- [146] A. ROTH, C. BRÜNE, H. BUHMANN, L. W. MOLENKAMP, J. MACIEJKO, X.-L. QI & S.-C. ZHANG; «Nonlocal transport in the quantum spin Hall state»; Science **325**, p. 294–297 (2009). 67
- [147] C. BRÜNE, A. ROTH, H. BUHMANN, E. M. HANKIEWICZ, L. W. MOLENKAMP, J. MACIEJKO, X.-L. QI & S.-C. ZHANG; «Spin polarization of the quantum spin Hall edge states»; Nat. Phys. **8**, p. 486–491 (2012). 67
- [148] X.-L. QI & S.-C. ZHANG; «Topological insulators and superconductors»; Rev. Mod. Phys. **83**, p. 1057–1110 (2011). 67, 70
- [149] X. LI, H. LIU, H. JIANG, F. WANG & J. FENG; «Edge engineering of a topological Bi(111) bilayer»; Phys. Rev. B Condens. Matter **90**, p. 165 412 (2014). 67
- [150] C. W. GROTH, M. WIMMER, A. R. AKHMEROV & X. WAIN TAL; «Kwant : a software package for quantum transport»; New Journal of Physics **16**, p. 063 065 (2014). 69
- [151] Y. ZHANG, K. HE, C.-Z. CHANG, C.-L. SONG, L.-L. WANG, X. CHEN, J.-F. JIA, Z. FANG, X. DAI, W.-Y. SHAN, S.-Q. SHEN, Q. NIU, X.-L. QI, S.-C. ZHANG, X.-C. MA & Q.-K. XUE; «Crossover of the three-dimensional topological insulator Bi₂Se₃ to the two-dimensional limit»; Nat. Phys. **6**, p. 584–588 (2010). 70
- [152] L. FU, C. L. KANE & E. J. MELE; «Topological Insulators in Three Dimensions»; Phys. Rev. Lett. **98**, p. 106 803 (2007). 69, 73

- [153] L. FU & C. L. KANE; «Topological insulators with inversion symmetry»; *Phys. Rev. B Condens. Matter* **76**, p. 1–17 (2007). 70
- [154] H. ZHANG, C.-X. LIU, X.-L. QI, X. DAI, Z. FANG & S.-C. ZHANG; «Topological insulators in Bi₂Se₃, Bi₂Te₃ and Sb₂Te₃ with a single Dirac cone on the surface»; *Nat. Phys.* **5**, p. 438–442 (2009). 70
- [155] S. CHADOV, X. QI, J. KÜBLER, G. H. FECHER, C. FELSER & S. C. ZHANG; «Tunable multifunctional topological insulators in ternary Heusler compounds»; *Nat. Mater.* **9**, p. 541–545 (2010). 70
- [156] H. LIN, L. A. WRAY, Y. XIA, S. XU, S. JIA, R. J. CAVA, A. BANSIL & M. Z. HASAN; «Half-Heusler ternary compounds as new multifunctional experimental platforms for topological quantum phenomena»; *Nat. Mater.* **9**, p. 546–549 (2010). 70
- [157] Y. L. CHEN, Z. K. LIU, J. G. ANALYTIS, J.-H. CHU, H. J. ZHANG, B. H. YAN, S.-K. MO, R. G. MOORE, D. H. LU, I. R. FISHER, S. C. ZHANG, Z. HUSSAIN & Z.-X. SHEN; «Single Dirac Cone Topological Surface State and Unusual Thermoelectric Property of Compounds from a New Topological Insulator Family»; *Phys. Rev. Lett.* **105**, p. 266 401 (2010). 70
- [158] B. YAN, H.-J. ZHANG, C.-X. LIU, X.-L. QI, T. FRAUENHEIM & S.-C. ZHANG; «Theoretical prediction of topological insulator in ternary rare earth chalcogenides»; *Phys. Rev. B : Condens. Matter Mater. Phys.* **82**, p. 161 108 (2010). 70
- [159] H. LIN, R. S. MARKIEWICZ, L. A. WRAY, L. FU, M. Z. HASAN & A. BANSIL; «Single-Dirac-cone topological surface states in the TlBiSe(2) class of topological semiconductors»; *Phys. Rev. Lett.* **105**, p. 036 404 (2010). 70
- [160] Y. ANDO; «Topological Insulator Materials»; *J. Phys. Soc. Jpn.* **82**, p. 102 001 (2013). 70
- [161] B. YAN & S.-C. ZHANG; «Topological materials»; *Rep. Prog. Phys.* **75**, p. 096 501 (2012). 70
- [162] M. HASAN & C. KANE; «Colloquium : Topological insulators»; *Rev. Mod. Phys.* **82**, p. 3045–3067 (2010). 70
- [163] J. C. Y. TEO & C. L. KANE; «Topological defects and gapless modes in insulators and superconductors»; *Phys. Rev. B : Condens. Matter Mater. Phys.* **82**, p. 115 120 (2010). 70

- [164] Y. ANDO & L. FU; «Topological Crystalline Insulators and Topological Superconductors : From Concepts to Materials»; Annual Review of Condensed Matter Physics **6**, p. 361–381 (2015). 70
- [165] C. BEENAKKER; «Search for Majorana fermions in superconductors»; Annu. Rev. Condens. Matter Phys. **4**, p. 113–136 (2013). 70, 88
- [166] J. ALICEA; «New directions in the pursuit of Majorana fermions in solid state systems»; Rep. Prog. Phys. **75**, p. 076 501 (2012). 70
- [167] S. YIP; «Noncentrosymmetric Superconductors»; Annu. Rev. Condens. Matter Phys. **5**, p. 15–33 (2014). 70, 88
- [168] Y. NAKAJIMA, R. HU, K. KIRSHENBAUM, A. HUGHES, P. SYERS, X. WANG, K. WANG, R. WANG, S. R. SAHA, D. PRATT, J. W. LYNN & J. PAGLIONE; «Topological RPdBi half-Heusler semimetals : A new family of noncentrosymmetric magnetic superconductors»; Sci Adv **1**, p. e1500 242 (2015). 70, 88
- [169] C. BEENAKKER & L. KOUWENHOVEN; «A road to reality with topological superconductors»; Nat. Phys. **12**, p. 618–621 (2016). 70
- [170] K. MANNA, Y. SUN, L. MÜCHLER, J. KÜBLER & C. FELSER; «Heusler, Weyl, and Berry»; arXiv preprint arXiv :1802.03771 (2018). 70
- [171] N. P. ARMITAGE, E. J. MELE & A. VISHWANATH; «Weyl and Dirac semimetals in three-dimensional solids»; Rev. Mod. Phys. **90**, p. 015 001 (2018). 70
- [172] B. YAN & C. FELSER; «Topological Materials : Weyl Semimetals»; Annu. Rev. Condens. Matter Phys. **8**, p. 337–354 (2017). 70
- [173] S.-Q. SHEN; *Topological Insulators; Springer Series in Solid-State Sciences*, tome 187 (Springer Singapore, Singapore) (2017). 70
- [174] G. TKACHOV; *Topological Insulators : The Physics of Spin Helicity in Quantum Transport* (CRC Press) (2015). 70
- [175] P. HOFMANN; «The surfaces of bismuth : Structural and electronic properties»; Prog. Surf. Sci. **81**, p. 191–245 (2006). 71, 73
- [176] H. DU, X. SUN, X. LIU, X. WU, J. WANG, M. TIAN, A. ZHAO, Y. LUO, J. YANG, B. WANG & J. G. HOU; «Surface Landau levels and spin states in bismuth (111) ultrathin films»; Nat. Commun. **7**, p. 10 814 (2016). 72, 79
- [177] C. R. AST & H. HÖCHST; «Fermi surface of Bi(111) measured by photoemission spectroscopy»; Phys. Rev. Lett. **87**, p. 177 602 (2001). 72, 73

- [178] S. GOLIN; «Band Structure of Bismuth : Pseudopotential Approach»; Phys. Rev. **166**, p. 643–651 (1968). 73
- [179] Y. LIU & R. E. ALLEN; «Electronic structure of the semimetals Bi and Sb»; Phys. Rev. B : Condens. Matter Mater. Phys. **52**, p. 1566 (1995). 73
- [180] Y. M. KOROTEEV, G. BIHLMAYER, J. E. GAYONE, E. V. CHULKOV, S. BLÜGEL, P. M. ECHENIQUE & P. HOFMANN; «Strong Spin-Orbit Splitting on Bi Surfaces»; Phys. Rev. Lett. **93**, p. 046 403 (2004). 73
- [181] Y. M. KOROTEEV, G. BIHLMAYER, E. V. CHULKOV & S. BLÜGEL; «First-principles investigation of structural and electronic properties of ultrathin Bi films»; Phys. Rev. B Condens. Matter **77**, p. 045 428 (2008). 73
- [182] J. C. Y. TEO, L. FU & C. L. KANE; «Surface states and topological invariants in three-dimensional topological insulators : Application to Bi_xSb_x »; Phys. Rev. B Condens. Matter **78**, p. 045 426 (2008). 73
- [183] T. HIRAHARA, N. FUKUI, T. SHIRASAWA, M. YAMADA, M. AITANI, H. MIYAZAKI, M. MATSUNAMI, S. KIMURA, T. TAKAHASHI, S. HASEGAWA & K. KOBAYASHI; «Atomic and electronic structure of ultrathin Bi(111) films grown on Bi_2Te_3 (111) substrates : evidence for a strain-induced topological phase transition»; Phys. Rev. Lett. **109**, p. 227 401 (2012). 73
- [184] I. AGUILERA, C. FRIEDRICH & S. BLÜGEL; «Electronic phase transitions of bismuth under strain from relativistic self-consistent *GW* calculations»; Phys. Rev. B Condens. Matter **91**, p. 125 129 (2015). 73
- [185] C. R. AST & H. HÖCHST; «Electronic structure of a bismuth bilayer»; Phys. Rev. B Condens. Matter **67**, p. 113 102 (2003). 73
- [186] B. ZHOU, H.-Z. LU, R.-L. CHU, S.-Q. SHEN & Q. NIU; «Finite size effects on helical edge states in a quantum spin-Hall system»; Phys. Rev. Lett. **101**, p. 246 807 (2008). 73
- [187] T. HIRAHARA, G. BIHLMAYER, Y. SAKAMOTO, M. YAMADA, H. MIYAZAKI, S. I. KIMURA, S. BLÜGEL & S. HASEGAWA; «Interfacing 2D and 3D topological insulators : Bi(111) bilayer on Bi_2Te_3 »; Phys. Rev. Lett. **107**, p. 1–5 (2011). 73
- [188] F. YANG, L. MIAO, Z. F. WANG, M.-Y. YAO, F. ZHU, Y. R. SONG, M.-X. WANG, J.-P. XU, A. V. FEDOROV, Z. SUN, G. B. ZHANG, C. LIU, F. LIU, D. QIAN, C. L. GAO & J.-F. JIA; «Spatial and energy distribution of topological edge states in single Bi(111) bilayer»; Phys. Rev. Lett. **109**, p. 016 801 (2012). 73

- [189] S. H. KIM, K.-H. JIN, J. PARK, J. S. KIM, S.-H. JHI, T.-H. KIM & H. W. YEOM; «Edge and interfacial states in a two-dimensional topological insulator : Bi(111) bilayer on $\{\{Bi\}\}_2\{\{Te\}\}_2\{Se\}$ »; Phys. Rev. B Condens. Matter **89**, p. 155 436 (2014). [73](#)
- [190] Z. LIU, C.-X. LIU, Y.-S. WU, W.-H. DUAN, F. LIU & J. WU; «Stable nontrivial Z2 topology in ultrathin Bi (111) films : a first-principles study»; Phys. Rev. Lett. **107**, p. 136 805 (2011). [73](#)
- [191] S. XIAO, D. WEI & X. JIN; «Bi(111) thin film with insulating interior but metallic surfaces»; Phys. Rev. Lett. **109**, p. 166 805 (2012). [73](#)
- [192] H. W. YEOM, K.-H. JIN & S.-H. JHI; «Topological fate of edge states of single Bi bilayer on Bi(111)»; Phys. Rev. B Condens. Matter **93**, p. 075 435 (2016). [73](#)
- [193] F. YANG, J. JANDKE, T. STORBECK, T. BALASHOV, A. AISHWARYA & W. WULFHEKEL; «Edge states in mesoscopic Bi islands on superconducting Nb(110)»; Phys. Rev. B Condens. Matter **96**, p. 235 413 (2017). [74](#), [82](#)
- [194] Y. OHTSUBO, L. PERFETTI, M. O. GOERBIG, P. LE FÈVRE, F. BERTRAN & A. TALEB-IBRAHIMI; «Non-trivial surface-band dispersion on Bi(111)»; New J. Phys. **15**, p. 033 041 (2013). [74](#)
- [195] L. PERFETTI, J. FAURE, E. PAPALAZAROU, J. MAUCHAIN, M. MARSÌ, M. O. GOERBIG, A. TALEB-IBRAHIMI & Y. OHTSUBO; «New aspects of electronic excitations at the bismuth surface : Topology, thermalization and coupling to coherent phonons»; J. Electron Spectrosc. Relat. Phenom. **201**, p. 60–65 (2015). [74](#)
- [196] S. ITO, B. FENG, M. ARITA, A. TAKAYAMA, R.-Y. LIU, T. SOMEYA, W.-C. CHEN, T. IIMORI, H. NAMATAME, M. TANIGUCHI, C.-M. CHENG, S.-J. TANG, F. KOMORI, K. KOBAYASHI, T.-C. CHIANG & I. MATSUDA; «Proving Nontrivial Topology of Pure Bismuth by Quantum Confinement»; Phys. Rev. Lett. **117**, p. 236 402 (2016). [74](#)
- [197] W. NING, F. KONG, C. XI, D. GRAF, H. DU, Y. HAN, J. YANG, K. YANG, M. TIAN & Y. ZHANG; «Evidence of topological two-dimensional metallic surface states in thin bismuth nanoribbons»; ACS Nano **8**, p. 7506–7512 (2014). [74](#)
- [198] W. NING, F. KONG, Y. HAN, H. DU, J. YANG, M. TIAN & Y. ZHANG; «Robust surface state transport in thin bismuth nanoribbons»; Sci. Rep. **4**, p. 7086 (2014). [74](#)

- [199] C. LI, A. KASUMOV, A. MURANI, S. SENGUPTA, F. FORTUNA, K. NAPOLSKII, D. KOSHKODAEV, G. TSIRLINA, Y. KASUMOV, I. KHODOS, R. DEBLOCK, M. FERRIER, S. GUÉRON & H. BOUCHIAT ; «Magnetic field resistant quantum interferences in Josephson junctions based on bismuth nanowires» ; Phys. Rev. B Condens. Matter **90**, p. 245 427 (2014). 74
- [200] A. MURANI, A. KASUMOV, S. SENGUPTA, Y. A. KASUMOV, V. T. VOLKOV, I. I. KHODOS, F. BRISSET, R. DELAGRANGE, A. CHEPELIANSKII, R. DEBLOCK, H. BOUCHIAT & S. GUÉRON ; «Ballistic edge states in Bismuth nanowires revealed by SQUID interferometry» ; Nat. Commun. **8**, p. 15 941 (2017). 74
- [201] Z. SONG, Z. FANG & C. FANG ; «(d-2)-Dimensional Edge States of Rotation Symmetry Protected Topological States» ; Phys. Rev. Lett. **119**, p. 246 402 (2017). 74
- [202] W. A. BENALCAZAR, B. A. BERNEVIG & T. L. HUGHES ; «Electric multipole moments, topological multipole moment pumping, and chiral hinge states in crystalline insulators» ; Phys. Rev. B Condens. Matter **96**, p. 245 115 (2017). 74
- [203] W. A. BENALCAZAR, B. A. BERNEVIG & T. L. HUGHES ; «Quantized electric multipole insulators» ; Science **357**, p. 61–66 (2017). 74
- [204] J. LANGBEHN, Y. PENG, L. TRIFUNOVIC, F. VON OPPEN & P. W. BROUWER ; «Reflection-Symmetric Second-Order Topological Insulators and Superconductors» ; Phys. Rev. Lett. **119**, p. 246 401 (2017). 74
- [205] S. A. PARAMESWARAN & Y. WAN ; «Viewpoint : Topological Insulators Turn a Corner» ; Physics **10** (2017). 75
- [206] C. B. DUKE, A. PATON, W. K. FORD, A. KAHN & J. CARELLI ; «Dynamical analysis of low-energy electron diffraction intensities from GaAs (110)-p (1× 1)-Sb (1 ML)» ; Phys. Rev. B : Condens. Matter Mater. Phys. **26**, p. 803 (1982). 75
- [207] R. M. FEENSTRA & P. MÅRTENSSON ; «Fermi-level pinning at the Sb/GaAs(110) surface studied by scanning tunneling spectroscopy» ; Phys. Rev. Lett. **61**, p. 447–450 (1988). 75
- [208] W. K. FORD, T. GUO, D. L. LESSOR & C. B. DUKE ; «Dynamical low-energy electron-diffraction analysis of bismuth and antimony epitaxy on GaAs(110)» ; Phys. Rev. B Condens. Matter **42**, p. 8952–8965 (1990). 75
- [209] M. G. BETTI, C. MARIANI, N. JEDRECY, R. PINCHAUX, A. RUOCCO & M. SAUVAGE-SIMKIN ; «Epitaxial continued-layer structure of Sb on GaAs(110)

- as observed by grazing-incidence x-ray diffraction»; *Phys. Rev. B : Condens. Matter Mater. Phys.* **50**, p. 14 336–14 339 (1994). 75
- [210] A. B. MCLEAN, R. M. FEENSTRA, A. TALEB-IBRAHIMI & R. LUDEKE; «Electronic and structural properties of a discommensurate monolayer system : GaAs(110)-(1{1}Bi)»; *Phys. Rev. B Condens. Matter* **39**, p. 12 925–12 928 (1989). 76
- [211] W. K. FORD, T. GUO, S. L. LANTZ, K. WAN, S.-L. CHANG, C. B. DUKE & D. L. LESSOR; «Bismuth and antimony adsorption on III-V (110) substrates : Growth, order, and structure»; *Journal of Vacuum Science & Technology B : Microelectronics Processing and Phenomena* **8**, p. 940–947 (1990). 76
- [212] M. G. BETTI, D. BERSELLI, C. MARIANI, N. JEDRECY, M. SAUVAGE-SIMKIN, Y. GARREAU & R. PINCHAUX; «(1 × 2) Bi chain reconstruction on the InAs(110) surface»; *Phys. Rev. B : Condens. Matter Mater. Phys.* **59**, p. 15 760–15 765 (1999). 76
- [213] A. ASSOULINE, C. FEUILLET-PALMA, N. BERGEAL, T. ZHANG, A. MOTTAGHI-ZADEH, A. ZIMMERS, E. LHUILLIER, M. MARANGOLO, M. EDDRIEF, P. ATKINSON *et al.*; «Spin-Orbit induced phase-shift in Bi \times 2 Se \times 3 Josephson junctions»; arXiv preprint arXiv :1806.01406 (2018). 85
- [214] M. KÖNIG, S. WIEDMANN, C. BRÜNE, A. ROTH, H. BUHMANN, L. W. MOLENKAMP, X.-L. QI & S.-C. ZHANG; «Quantum spin Hall insulator state in HgTe quantum wells»; *Science* **318**, p. 766–770 (2007). 86
- [215] T. CLARK, R. PRANCE & A. GRASSIE; «Feasibility of hybrid Josephson field effect transistors»; *Journal of Applied Physics* **51**, p. 2736–2743 (1980). 87
- [216] C. NGUYEN, H. KROEMER & E. L. HU; «Anomalous Andreev conductance in InAs-AlSb quantum well structures with Nb electrodes»; *Physical review letters* **69**, p. 2847 (1992). 87
- [217] Y.-J. DOH, J. A. VAN DAM, A. L. ROEST, E. P. BAKKERS, L. P. KOUWENHOVEN & S. DE FRANCESCHI; «Tunable supercurrent through semiconductor nanowires»; *science* **309**, p. 272–275 (2005). 87
- [218] C. LIU, T. L. HUGHES, X.-L. QI, K. WANG & S.-C. ZHANG; «Quantum spin Hall effect in inverted type-II semiconductors»; *Physical review letters* **100**, p. 236 601 (2008). 87, 88

- [219] B. A. BERNEVIG, T. L. HUGHES & S.-C. ZHANG ; «Quantum spin Hall effect and topological phase transition in HgTe quantum wells» ; Science **314**, p. 1757–1761 (2006). 87
- [220] C. BRÜNE, C. LIU, E. NOVIK, E. HANKIEWICZ, H. BUHMANN, Y. CHEN, X. QI, Z. SHEN, S. ZHANG & L. MOLENKAMP ; «Quantum Hall effect from the topological surface states of strained bulk HgTe» ; Physical review letters **106**, p. 126 803 (2011). 87
- [221] M. L. COHEN & T. BERGSTRESSER ; «Band structures and pseudopotential form factors for fourteen semiconductors of the diamond and zinc-blende structures» ; Physical Review **141**, p. 789 (1966). 88
- [222] I. KNEZ & R.-R. DU ; «Quantum spin Hall effect in inverted InAs/GaSb quantum wells» ; Frontiers of Physics **7**, p. 200–207 (2012). 88
- [223] L. DU, I. KNEZ, G. SULLIVAN & R.-R. DU ; «Robust helical edge transport in gated InAs/GaSb bilayers» ; Physical review letters **114**, p. 096 802 (2015). 88
- [224] T. LI, P. WANG, H. FU, L. DU, K. A. SCHREIBER, X. MU, X. LIU, G. SULLIVAN, G. A. CSÁTHY, X. LIN *et al.* ; «Observation of a helical Luttinger liquid in InAs/GaSb quantum spin Hall edges» ; Physical review letters **115**, p. 136 804 (2015). 88
- [225] F. NICHELE, A. N. PAL, P. PIETSCH, T. IHN, K. ENSSLIN, C. CHARPENTIER & W. WEGSCHEIDER ; «Insulating State and Giant Nonlocal Response in an In As/Ga Sb Quantum Well in the Quantum Hall Regime» ; Physical review letters **112**, p. 036 802 (2014). 88
- [226] J. C. TEO & C. L. KANE ; «Majorana fermions and non-Abelian statistics in three dimensions» ; Physical review letters **104**, p. 046 401 (2010). 88
- [227] X.-L. QI & S.-C. ZHANG ; «Topological insulators and superconductors» ; Reviews of Modern Physics **83**, p. 1057 (2011). 88
- [228] J. ALICEA ; «New directions in the pursuit of Majorana fermions in solid state systems» ; Reports on progress in physics **75**, p. 076 501 (2012). 88
- [229] Y. ANDO & L. FU ; «Topological crystalline insulators and topological superconductors : from concepts to materials» ; Annu. Rev. Condens. Matter Phys. **6**, p. 361–381 (2015). 88
- [230] C. BEENAKKER & L. KOUWENHOVEN ; «A road to reality with topological superconductors» ; Nature Physics **12**, p. 618 (2016). 88

- [231] F. NICHELE, H. J. SUOMINEN, M. KJAERGAARD, C. M. MARCUS, E. SAJADI, J. A. FOLK, F. QU, A. J. BEUKMAN, F. K. DE VRIES, J. VAN VEEN *et al.*; «Edge transport in the trivial phase of InAs/GaSb»; *New Journal of Physics* **18**, p. 083 005 (2016). 88
- [232] P.-Y. DELAUNAY, A. HOOD, B. M. NGUYEN, D. HOFFMAN, Y. WEI & M. RAZEGHI; «Passivation of type-II In As/ Ga Sb double heterostructure»; *Applied Physics Letters* **91**, p. 091 112 (2007). 88
- [233] B.-M. NGUYEN, D. HOFFMAN, E. K.-w. HUANG, P.-Y. DELAUNAY & M. RAZEGHI; «Background limited long wavelength infrared type-II InAs/GaSb superlattice photodiodes operating at 110 K»; *Applied Physics Letters* **93**, p. 123 502 (2008). 88
- [234] B. D. JOSEPHSON; «Possible new effects in superconductive tunnelling»; *Physics letters* **1**, p. 251–253 (1962). 88
- [235] V. AMBEGAOKAR & A. BARATOFF; «Tunneling between superconductors»; *Physical Review Letters* **10**, p. 486 (1963). 97
- [236] A. BARONE & G. PATERNO; *Physics and applications of the Josephson effect*; tome 1 (Wiley Online Library) (1982). 99
- [237] J. E. SESTOFT, T. KANNE, A. N. GEJL, M. VON SOOSTEN, J. S. YODH, D. SHERMAN, B. TARASINSKI, M. WIMMER, E. JOHNSON, M. DENG, J. NYGÅRD, T. S. JESPERSEN, C. M. MARCUS & P. KROGSTRUP; «Engineering hybrid epitaxial InAsSb/Al nanowires for stronger topological protection»; *Phys. Rev. Materials* **2**, p. 044 202 (2018). 106
- [238] D. LAROCHE, D. BOUMAN, D. J. VAN WOERKOM, A. PROUTSKI, C. MURTHY, D. I. PIKULIN, C. NAYAK, R. J. VAN GULIK, J. NYGÅRD, P. KROGSTRUP *et al.*; «Observation of the 4π -periodic Josephson effect in InAs nanowires»; arXiv preprint arXiv :1712.08459 (2017). 106
- [239] S. M. ALBRECHT, A. P. HIGGINBOTHAM, M. MADSEN, F. KUEMMETH, T. S. JESPERSEN, J. NYGÅRD, P. KROGSTRUP & C. M. MARCUS; «Exponential protection of zero modes in Majorana islands»; *Nature* **531**, p. 206–209 (2016). 106
- [240] A. DAS, Y. RONEN, Y. MOST, Y. OREG, M. HEIBLUM & H. SHTRIKMAN; «Zero-bias peaks and splitting in an Al–InAs nanowire topological superconductor as a signature of Majorana fermions»; *Nat. Phys.* **8**, p. 887–895 (2012). 106

- [241] V. MOURIK, K. ZUO, S. M. FROLOV, S. R. PLISSARD, E. P. a. M. BAKKERS & L. P. KOUWENHOVEN ; «Signatures of Majorana Fermions in Hybrid Superconductor-Semiconductor Nanowire Devices» ; *Science* **336**, p. 1003–1007 (2012). [106](#)
- [242] H. ZHANG, O. GÜL, S. CONESA-BOJ, K. ZUO, V. MOURIK, F. K. DE VRIES, J. VAN VEEN, D. J. VAN WOERKOM, M. P. NOWAK, M. WIMMER *et al.* ; «Ballistic Majorana nanowire devices» ; arXiv preprint arXiv :1603.04069 **10** (2016). [106](#)

Limite d'Anderson et états de bords topologiques

Tianzhen Zhang

Ces dix dernières années ont vu l'émergence des théories des bandes topologiques. La recherche de structures de bandes topologiquement non triviales ont conduit à la prédiction théorique d'une pléthore de nouveaux matériaux: isolants topologiques, semi-métaux topologiques, supraconducteurs topologiques.

Dans ce contexte, la famille de semiconducteurs III-V est particulièrement intéressante. Il a été montré théoriquement et expérimentalement que l'hétérostructure InAs /GaSb constitue un isolant topologique bidimensionnel. En outre, il a également été montré, théoriquement et expérimentalement, que le dépôt d'une électrode supraconductrice sur un nanofil de InAs conduit à un supraconducteur topologique, lorsque soumis à un champ magnétique axial. De même, le dépôt d'une électrode supraconductrice sur un isolant topologique bidimensionnel InAs/GaSb devrait donner naissance à un supraconducteur topologique. Ce contexte a conduit à un regain d'intérêt pour l'étude fondamentale de l'interface entre les métaux et les semi-conducteurs III-V.

Pour cette thèse, j'ai travaillé sur la croissance de nanocristaux supraconducteurs (Pb) et semi-métalliques (Bi) sur la surface (110) des InAs et la spectroscopie STM de ces systèmes. En outre, j'ai également travaillé sur la microfabrication de jonctions Josephson et de dispositifs SQUID avec des hétérostructures InAs/GaSb, qui pourraient, à l'avenir, être utilisées dans la spectroscopie STM en coupe transversale.

Dans ce manuscrit, je présenterai, dans le premier chapitre, les bases théoriques de l'effet tunnel quantique et passerai en revue notre compréhension actuelle de l'interface entre les semi-conducteurs III-V et les couches métalliques.

Dans le deuxième chapitre, je vais décrire une première expérience dans laquelle je montre que des nanocristaux de plomb (Pb) supraconducteurs de haute qualité peuvent être réalisés sur la surface (110) d'InAs. Nous avons découvert que lorsque la dimension latérale des nanocristaux de Pb est inférieure à la longueur d'onde de Fermi du gaz d'électrons bidimensionnel accumulé à la surface de InAs, les nanocristaux sont faiblement couplés à ce gaz électronique et, par conséquent, se trouvent dans le régime du blocage de Coulomb. Ce phénomène a permis la première étude de l'effet de parité supraconducteur par spectroscopie STM, que nous avons utilisée pour vérifier la validité de la limite d'Anderson. De plus, nous avons identifié, dans ces nanocristaux de Pb, la signature

de niveaux électroniques discrets et tenté une cartographie des fonctions d'onde électroniques correspondantes.

Dans le troisième chapitre, je vais décrire une deuxième expérience STM où je montre que des nanocristaux de Bismuth (Bi) de haute qualité peuvent également être réalisés sur la surface (110) d'InAs. Contrairement aux nanocristaux de Pb, une couche de mouillage de Bi sépare les nanocristaux de la surface InAs, conduisant à un fort couplage entre les nanocristaux de Bi et le substrat. A partir de la spectroscopie STM, nous avons identifié des états de bord sur le plan (111) des nanocristaux de bismuth. Ces états de bord ont une symétrie C_3 , qui est inférieure à la symétrie C_6 de la face (111). En supposant que le bismuth est un isolant topologique de second ordre comme suggéré théoriquement, les états de bords observés peuvent être interprétés naturellement comme les états de charnière prédits dans cette dernière théorie de la bande topologique.

Enfin, dans le dernier chapitre, je présenterai les méthodes que j'ai développées pour la fabrication de jonctions Josephson hybrides sur des hétérostructures InAs et InAs/GaSb, ainsi que des mesures préliminaires des caractéristiques Josephson.

Dans la première expérience, nous avons vu qu'il est possible de cultiver du Pb de haute qualité nanocristaux à la surface (110) des InAs. En raison de la grande longueur d'onde de Fermi, plus

grande que la dimension latérale du nanocristal, le nanocristal n'est que faiblement couplé au substrat, ce qui conduit à l'apparition d'un blocage de Coulomb. Grâce à ce phénomène, nous avons pu étudier, pour la première fois par STM, l'effet de parité supraconducteur que nous avons utilisé pour tester la validité de la limite d'Anderson. Observez les niveaux électroniques discrets et tentez la cartographie des fonctions d'onde correspondantes.

Dans la deuxième expérience, nous avons vu que les nanocristaux de Bi peuvent également être développés Sur le dessus des InAs. Cependant, en raison de la présence de couche de mouillage de Bi à l'interface entre InAs et le nanocristal, le couplage électronique entre les nanocristaux de Bi et le substrat est fort, ce qui supprime le blocage de Coulomb. Cartes spectroscopiques sur la face (111) des nanocristaux sur lesquels on identifie les états de bord Ces états de bord peuvent être naturellement interprétés comme les états de charnière attendus pour les isolants topologiques 3D de second ordre où les états de bord sont unidimensionnels

Enfin, au cours de cette thèse, j'ai développé, dans le groupe, les méthodes de microfabrication pour la fabrication de jonctions Josephson et de SQUID asymétriques avec des substrats InAs et des hétérostructures InAs/GaSb. Les résultats préliminaires indiquent que notre méthode de préparation de

surface des InAs est fiable et conduit à de bonnes caractéristiques de Josephson.

Alors que mes résultats de STM sur nanocristaux supraconducteurs Pb ne semblent pas avoir un relation directe avec ces résultats, d'autres travaux sous champ magnétique peut être intéressant pour la supraconductivité topologique. En effet, Pb nanocristaux ont tendance à accumuler sur les bords de l'étape du nanofil InAs. En améliorant la croissance procédure, il semble tout à fait possible de cultiver un nanofil le long de ce bord par étape la fusion des nanocrytals Pb. Utilisation d'un STM équipé d'un champ magnétique vectoriel domaine, il devrait être possible d'appliquer le champ magnétique le long de la direction axiale du nanofil, ou l'étape de pointe de manière équivalente, et l'étude du spectre à effet tunnel vers la fin de la nanofil. Ce système semble offrir une réalisation possible d'un supraconducteur topologique grâce à l'effet de proximité supraconducteur induit dans un semi-conducteur nanofil, comme suggéré par Lutchyn théoriquement et al. et observé expérimentalement en InAs et nanofils InSb Sur les Bi nanocristaux, nous avons identifié topologiques bord états. Il serait intéressant d'observer les beaux-bords étendus. Pour ce faire, il pourrait aussi être intéressant de tenter la croissance de nanofils le long de bords Bis étape de semi-conducteurs III-V.

Enfin, pour la hétérostructure InAs/GaSb, l'une des motivations pour le développement des méthodes de microfabrication sur ce système dans le groupe est d'étudier la topologie des états de bord sur le côté de cette hétérostructure par spectroscopie STM. En effet, plusieurs ouvrages, notamment par nos collaborateurs de C2N, ont montré qu'il était possible d'effectuer la spectroscopie à effet tunnel sur les bords des hétérostructures clivées.

Titre : Limite d'Anderson et états de bords topologiques

Mots clés : Supraconductivité, Topologie, STM, Jonction Josephson

Résumé : Cette thèse décrit la fabrication de systèmes hybrides basés sur le semi-conducteur InAs, leur étude par spectroscopie STM et la mesure de jonctions Josephson. Dans une première expérience, je montre que des nanocristaux (NC) de plomb (Pb) supraconducteurs de haute qualité peuvent être cristallisés sur la surface (110) de InAs. Lorsque la taille latérale des NCs est inférieure à la longueur d'onde de Fermi du gaz d'électrons bidimensionnel accumulé à la surface de InAs, les NCs ne sont que faiblement couplés à ce gaz électronique et se retrouvent donc dans le régime de blocage de Coulomb. Ce phénomène a permis la première étude de l'effet de parité supraconducteur par spectroscopie STM, que nous avons utilisée pour vérifier la validité de la limite d'Anderson.

Dans une seconde expérience, je montre que des NCs de Bismuth (Bi) de haute qualité peuvent

également être cristallisés sur la surface (110) de InAs. Contrairement aux NCs de Pb, une couche de mouillage de Bi sépare les NCs de la surface, conduisant à un fort couplage entre les NCs de Bi et le substrat. A partir de la spectroscopie STM, nous avons identifié des états de bord sur le plan (111) des NCs avec une symétrie C3. En supposant que le bismuth est un isolant topologique de second ordre comme suggéré théoriquement, les états de bords observés peuvent être interprétés naturellement comme les états de charnière prédits dans cette dernière théorie de bande topologique.

Enfin, je présenterai les méthodes que j'ai développées pour la fabrication de jonctions Josephson hybrides sur des hétérostructures InAs et InAs / GaSb, ainsi que des mesures préliminaires des caractéristiques Josephson.

Title : Anderson limit and topological edge states

Keywords : Superconductivity, Topological, STM, Josephson Junction

Abstract : This thesis describes the fabrication of hybrid systems based on the narrow-gap semiconductor InAs and their study through STM spectroscopy and measure of Josephson characteristics. In the first experiment, I show that high quality superconducting Lead (Pb) nanocrystals can be grown on the (110) surface of InAs. When the lateral size of the Pb nanocrystals is smaller than the Fermi wavelength of the two-dimensional electron gas accumulated at the surface of InAs, the nanocrystals are only weakly coupled to this electron gas and, consequently, are found in the regime of Coulomb blockade. This phenomenon enabled the first study of the superconducting parity effect through STM spectroscopy, which we employed to check the validity of the Anderson limit.

In the second experiment, I show that high quality Bis-

muth (Bi) nanocrystals can also be grown on the (110) surface of InAs. In contrast to Pb nanocrystals, a wetting layer of Bi separates the nanocrystals from the InAs surface, leading to a strong coupling between the Bi nanocrystals and the substrate. From STM spectroscopy, we have identified edge-states on the (111) plane of the nanocrystals with C3 symmetry. Assuming that Bismuth is a 2nd order topological insulator as suggested theoretically, the observed edge-states can be interpreted naturally as the hinge-states predicted in this last topological band theory.

Finally, I will present the methods that I developed for the fabrication of hybrid Josephson junctions on bulk InAs and InAs/GaSb heterostructures, together with preliminary measurements of Josephson characteristics.

